Chapter 4
Shock Wave Interaction with Bodies of Various Shapes

Shock wave interactions with cylinders and other bodies are one of the fundamental topics of shock-dynamics. In this chapter results of flow visualizations over these body are presented.
Counting fringe orders, the density distribution over the bodies can be determined. Then the density distributions can be converted to the pressure distributions. However, the quantitative density distributions demonstrate slip lines and hence useful to validate numerical schemes.

The procedure of estimating density distribution from interferograms are conducted as follows: Interferometric fringe number N is determined integrating the density along the *OB* path,

$$N\lambda/K = \int_0^L (\rho - \rho_0)dz \tag{4.1}$$

where L is the light path length, that is, the shock tube width and z is the distance of light path length. The λ is wave length of ruby laser 694.3 nm. The ρ and the ρ_0 are densities behind and in front of the shock wave. If the density profile in the boundary layer is known, the path integral is rewritten as following,

$$\begin{aligned} N\lambda/K = &\int_{\text{upper boundary layer}} (\rho - \rho_0)dz + \int_{\text{core flow}} (\rho - \rho_0)dz \\ &+ \int_{\text{lower boundary layer}} (\rho - \rho_0)dz \end{aligned} \tag{4.2}$$

Assume that the shock tube wall is at room temperature and, for the sake of simplicity, the Karmann-Pohlhausen velocity profile in the boundary layer, Eq. (4.2) can be rewritten as follows,

K. Takayama, *Visualization of Shock Wave Phenomena*,
https://doi.org/10.1007/978-3-030-19451-2_4

$$N\lambda/K = L(\rho_2 - \rho_W) + 2\delta\left(\rho_W \int_0^1 f(\eta)d\eta - \rho_2\right)dz \tag{4.3}$$

where ρ_w is the density on the wall and f(η) is the Karmann Pohlhausen velocity profile across the boundary layer, where $\eta = z/\delta$, $A = -(\gamma - 1/2)M^2\ \rho_w/\rho_2$, and $B = -\{(\gamma - 1/2)M^2 + 1 - (T_w/T_2))\rho_w/\rho_2$.

$$f(\eta) = 1/\left\{A\left(2\eta - 2\eta^3 + \eta^4\right)^2\square + B\left(2\eta - 2\eta^3 + \eta^4\right) + 1\right\}^{\square} \tag{4.4}$$

T_w is the wall temperature and T_2 is the uniform flow temperature behind the shock wave. M is the uniform flow Mach number behind the shock wave. For Ms = 1.7 and a wall temperature T_w = 300 K, M = 0.77, ρ_w/ρ_2 = 1.458, and Tw/T2 = ρ_w/ρ_2, respectively. A = 0.1729 and B = 0.4327 and eventually $\int_0^1 f(\eta)d\eta = 0.836$. Therefore, the fringe number N is given by

$$N = KL/\lambda(\rho_2 - \rho_0)(1 + 0.836\delta/L). \tag{4.5}$$

The density increment Δρ corresponding to one fringe shift is given by

$$\Delta\rho/\rho_0 = \lambda/(KL\rho_0)/(1 + 0.836\delta/L) \tag{4.6}$$

For L = 60 mm, λ = 694.3 nm and the Gladstone-Dale constant K of this wavelength, $\Delta\rho/\rho_0$ is equivalent to approximately 4.6% of the ambient density. The ratio of the density increment taking the boundary layer displacement thickness into consideration, that corresponding to one fringe shift is written as

$$\Delta\rho/\rho_0 = 1 + 0.88\delta/L. \tag{4.7}$$

This implies that the contribution of the boundary layer displacement thickness δ to the total fringe shift is 0.88δ/L. For laminar boundary layer, according to the boundary layer theory (Schlichting 1960), the boundary layer displacement thickness is given by

$$\delta/L = 7.812(x/Re)^{1/2} \tag{4.8}$$

where x is the distance measured from the incident shock wave.

δ/L for the present shock tube flow is approximately 0.025 at x = 1 m. The effect of the boundary layer on fringe number decreases by 2%. The correction of fringe number is so small that it may be neglected if the experiments are not conducted at extremely low pressures.

The density distribution over cylinders can be determined simply by counting the fringe numbers. The resulting density distribution is convertible to a pressure distribution in the neighborhood of the cylinder surface, if the isentropic relation is

applied at a given value of stagnation density. From known pressure distributions over the cylinders, the pressure coefficient is readily determined and then the drag and lift forces are obtained by counting fringes on interferograms.

4.1 Circular Cylinder

4.1.1 Cylinder in Air

A 40 mm diameter circular cylinder was put between two 15 mm thick acrylic plates which were glued in the frame of the test section of the 60 mm × 150 mm conventional shock tube. Visualizations were conducted for a wide range of Ms and initial pressure using double exposure holographic interferometry. Acrylic plates are slightly inhomogeneous but would not distorted fringe distributions but only affected the image contrast.

Figure 4.1 shows the installation of a 20 mm diameter cylinder in the test section windows.

Figure 4.2 show sequential observations of a shock wave for Ms = 1.50 over a 40 mm diameter cylinder. The reflected shock wave pattern is RR when the shock wave impinged at the frontal stagnation area of the cylinder. The reflection pattern became SMR, when the shock wave approached to the equator of the cylinder. The transmitting shock waves propagated along the upper and lower sides of the cylinder toward the rear stagnation point. At the same time, the triple points TP are formed emanating curved Mach stems MS and slip lines SL.

Figure 4.3 show sequential observation of a shock wave for Ms = 2.6 in air propagating along a 40 mm diameter cylinder installed in the 60 mm × 150 mm conventional shock tube. At frontal surface, the reflection pattern was initially a RR.

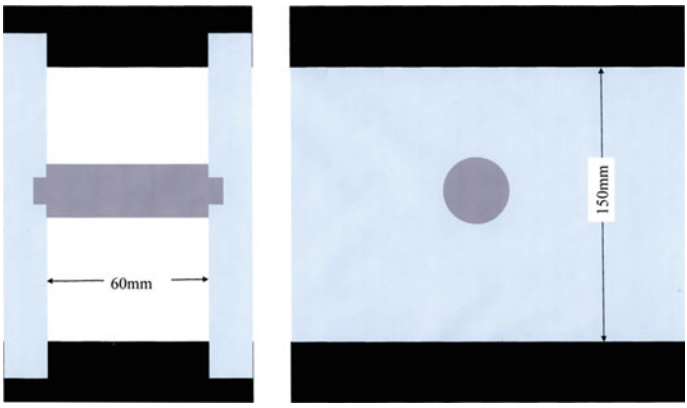

Fig. 4.1 Installation of a cylinder in the test section

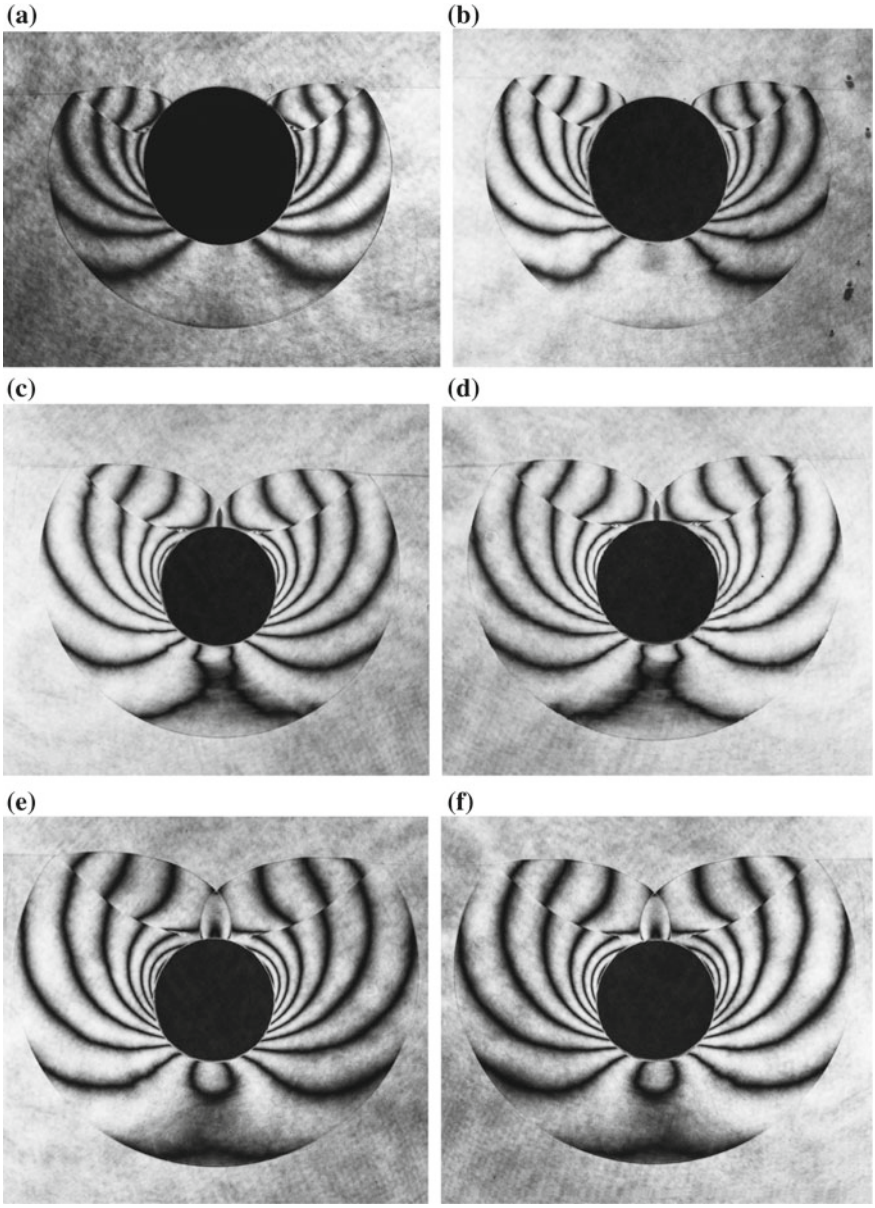

Fig. 4.2 Interaction of a shock wave with a 40 mm diameter circular cylinder for Ms = 1.50 in air at 275 hPa, 299.6 K: **a** #96053044, 180 μs Ms = 1.499; **b** #96053008, 190 μs Ms = 1.499; **c** #96053011, 200 μs Ms = 1.501; **d** #96053012, 220 μs, Ms = 1.497; **e** #96053013, 230 μs Ms = 1.503; **f** #96053014, 240 μs Ms = 1.500; **g** #96053015, 250 μs Ms = 1.499; **h** #96053016, 260 μs Ms = 1.501

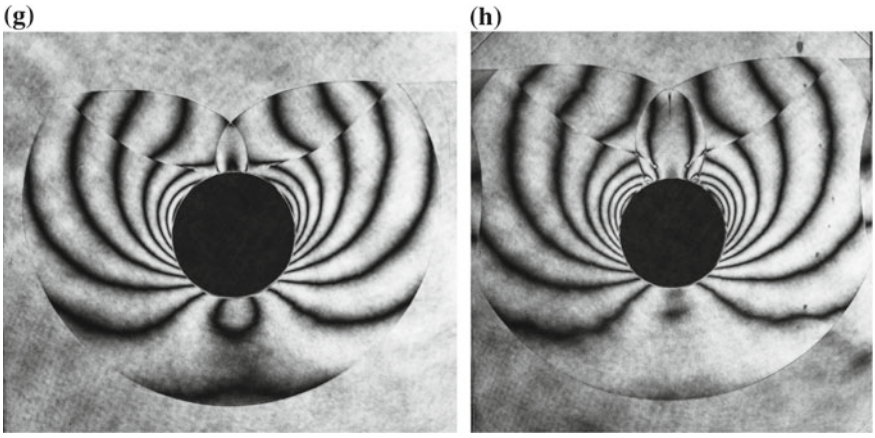

Fig. 4.2 (continued)

At the equator seen in Fig. 4.3a the SMR appear accompanying TP and curved MS seen in Fig. 4.3b. The Mach stems propagated along the upper and lower wall were reflected at the rear stagnation point and the reflected MS moved to the reverse direction. The reflected MS interacted with boundary layer developing along the cylinder surface. This process of the interaction is similar to the reflected shock interaction with the side wall boundary layer at the shock tube side wall (Mark 1956). Another reflected shock wave/boundary layer interaction was observed. In Fig. 4.3e an arrow indicates the bifurcation of RS interacting with the boundary layer developing along the shock tube sidewall. Figure 4.3g, h show the patterns of reflected MS interacting with boundary layer. The MS interacts with a SL emanating from the TP.

Figure 4.4 show sequential observations of interaction of shock wave of Ms = 1.70 with a 20 mm diameter cylinder in air at 900 hPa. The experiment was performed in the 60 mm × 150 mm conventional shock tube.

4.1.2 Cylinder in CO_2

Figure 4.5 show the evolution of shock wave interactions with a 20 mm diameter cylinder in CO_2 in a conventional 60 mm × 150 mm shock tube. A 20 mm cylinder was sandwiched between two acrylic plates, which were once used to measure pressures and then had holes accommodating the pressure transducers. In Fig. 4.5c, the black circular shadows were remnants of the smoothly plugged holes accommodating the pressure transducers.

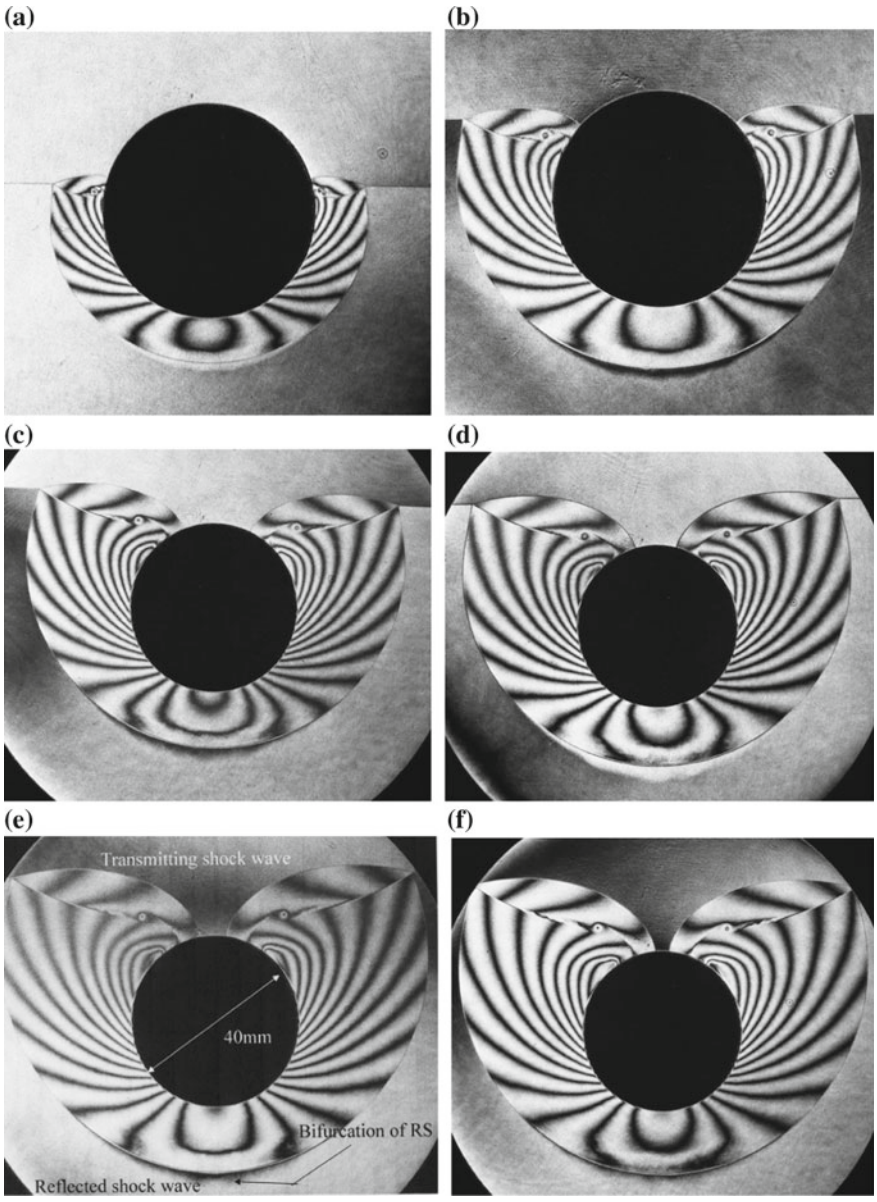

Fig. 4.3 Shock interaction with a 40 mm diameter cylinder for Ms = 2.60 in air at 100 hPa, 291.1 K: **a** #83110803, Ms = 2.591; **b** #83110901, Ms = 2.591; **c** #83110904, Ms = 2.617; **d** #83110802, Ms = 2.591; **e** #83050902, Ms = 2.620; **f** #83110906, Ms = 2.607; **g** #83050903, Ms = 2.589; **h** #83050901, Ms = 2.589; **i** enlargement of (**h**); **j** #83050904, Ms = 2.579

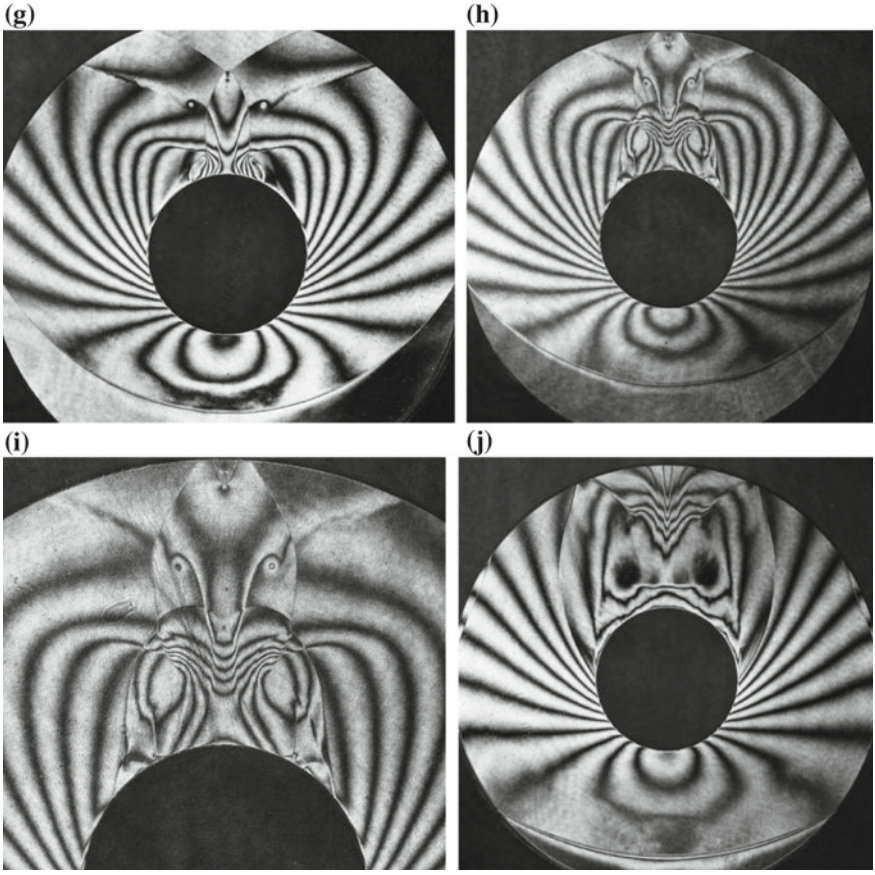

Fig. 4.3 (continued)

The polyatomic gases are favorable media from the point of view of interferometric visualization. The Gladstone-Dale constant in CO_2 and air are 0.00045 and 0.00027. respectively and the sensitivity of the fringes are proportional to the Gladstone-Dale constant. Therefore, the sensitivity of CO_2 is 1.7 times higher than that of air. This effect is much pronounced in SF_6.

The specific heats ratio, γ, in monoatomic gases is 1.667, that in air is 1.4, that in CO_2 is 1.29, and that in SF_6 is 1.08. The reflected shock wave will bifurcate due to the interacting with the sidewall boundary layer. With the value of γ approaching to unity, the range of Ms at which the bifurcation occurs becomes wider and the effect of such an interaction is more pronounced. The interaction between the reflected MS and the boundary layer along the cylinder surface is enhanced with the decrease in the value of γ (Mark 1956).

In monatomic gas, on the contrary, the effect of the reflected shock wave/boundary layer is minimized.

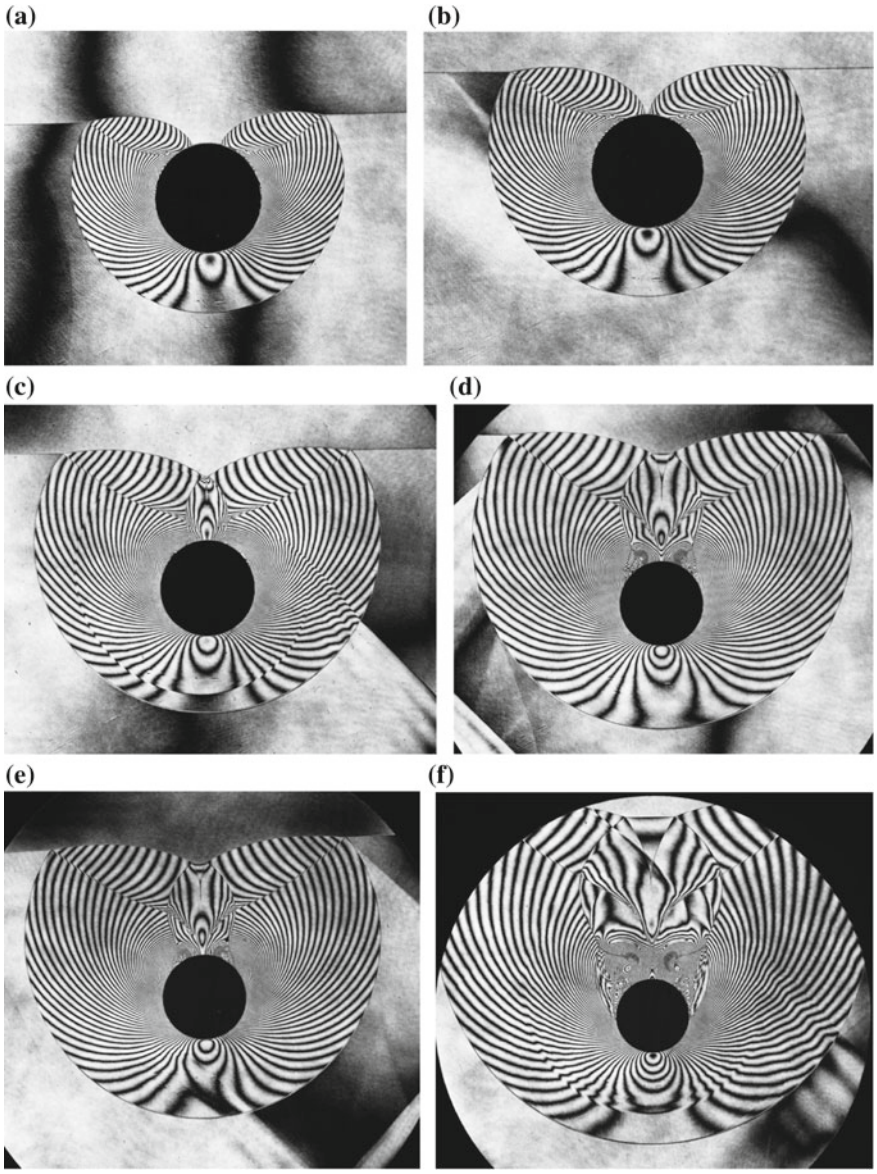

Fig. 4.4 Evolution of shock wave interaction with a 20 mm diameter cylinder for Ms—1.70, Re = 0.3×10^5 in air at 900 hPa, 2891.1 K: **a** #88012703, Ms = 1.673; **b** #88012705, Ms = 1.680; **c** #88012706, Ms = 1.678; **d** #88012707, Ms = 1.719; **e** #88012801, Ms = 1.723; **f** #88012708; Ms = 1.687, 900 hPa; **g** 88012802 623 μs Ms = 1.701; **h** enlargement of (**g**); **i** #88012715, Ms = 1.703; **j** #88012709, Ms = 1.713; **k** 88012803, Ms = 1.723; **l** #88012804; Ms = 1.681; **m** #88012710, Ms = 1.737; **n** #88012714, Ms = 1.675; **o** #88012809, Ms = 1.728; **p** #88012807. Ms = 1.672

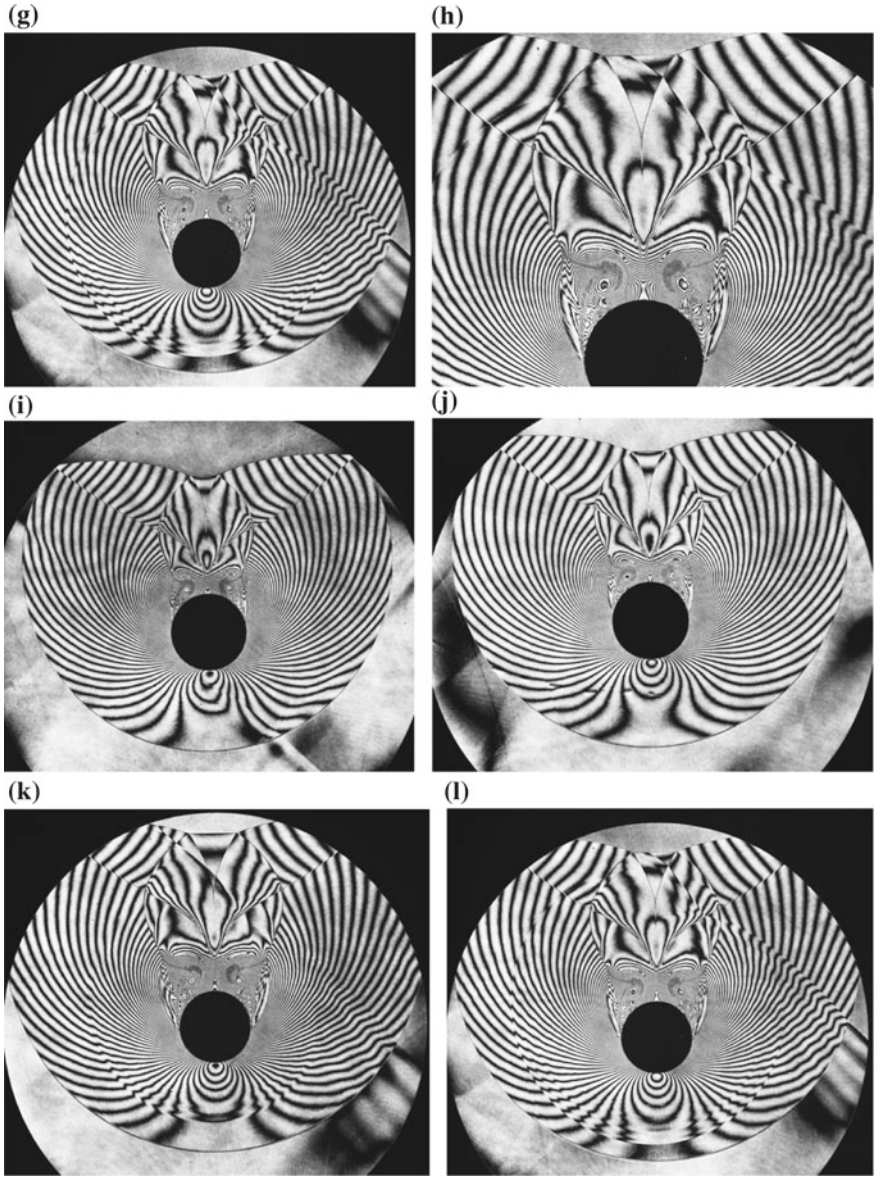

Fig. 4.4 (continued)

Figure 4.6 show the evolution of shock wave interaction with a 20 mm cylinder for Ms = 2.20 in CO_2 at 300 hPa, 289.1 K. Experiments were performed in a 60 mm $\times$ 150 mm conventional shock tube. Fringes in a densely populated area are hardly resolved but the density distribution precisely. In Fig. 4.6a–f, nearly

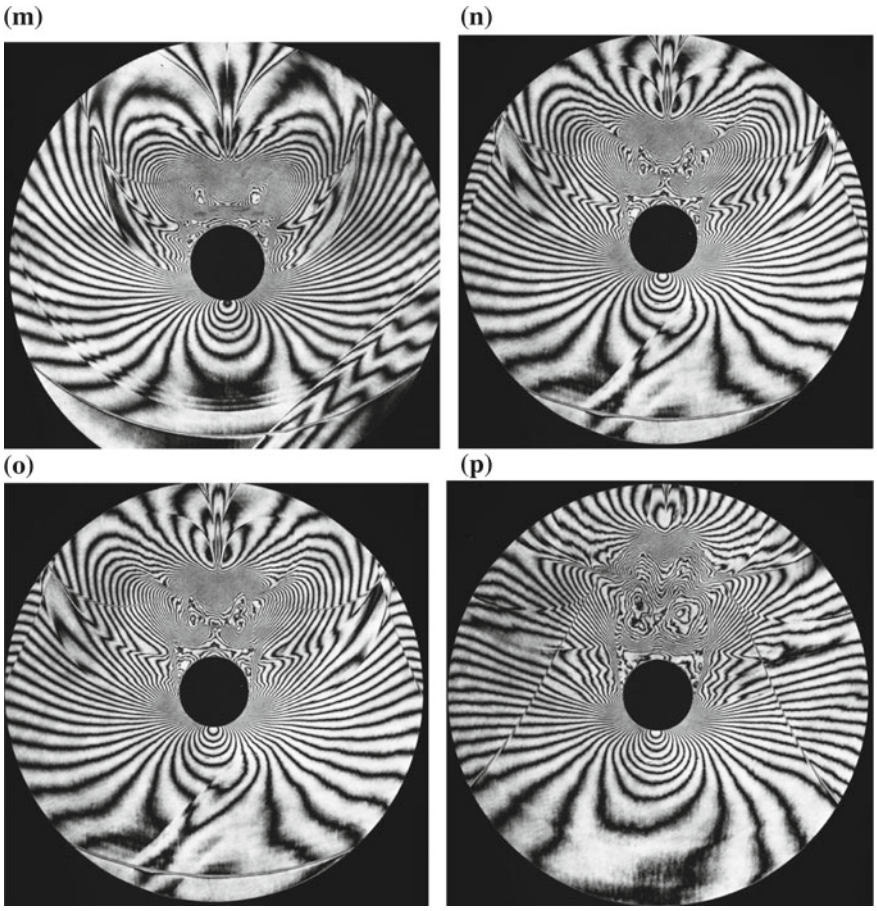

Fig. 4.4 (continued)

steady supersonic shock tube flows were built up so that the shock stand-off distance over the 20 mm diameter cylinder was maintained for a while.

4.1.3 Cylinder in SF_6

Figure 4.7 show sequential observations of shock wave/cylinder interaction in SF_6 at 100 hPa. The RS interacted with the sidewall boundary layer and caused a wide bifurcation region which were missing in Fig. 4.6.

Figure 4.8 show later stage of shock wave interaction with a 20 mm diameter cylinder for Ms = 4.20 in SF_6 at 20 hPa, 290.2 K. The RS along the frontal surface of the cylinder interacted with the boundary layer developing along the shock tube

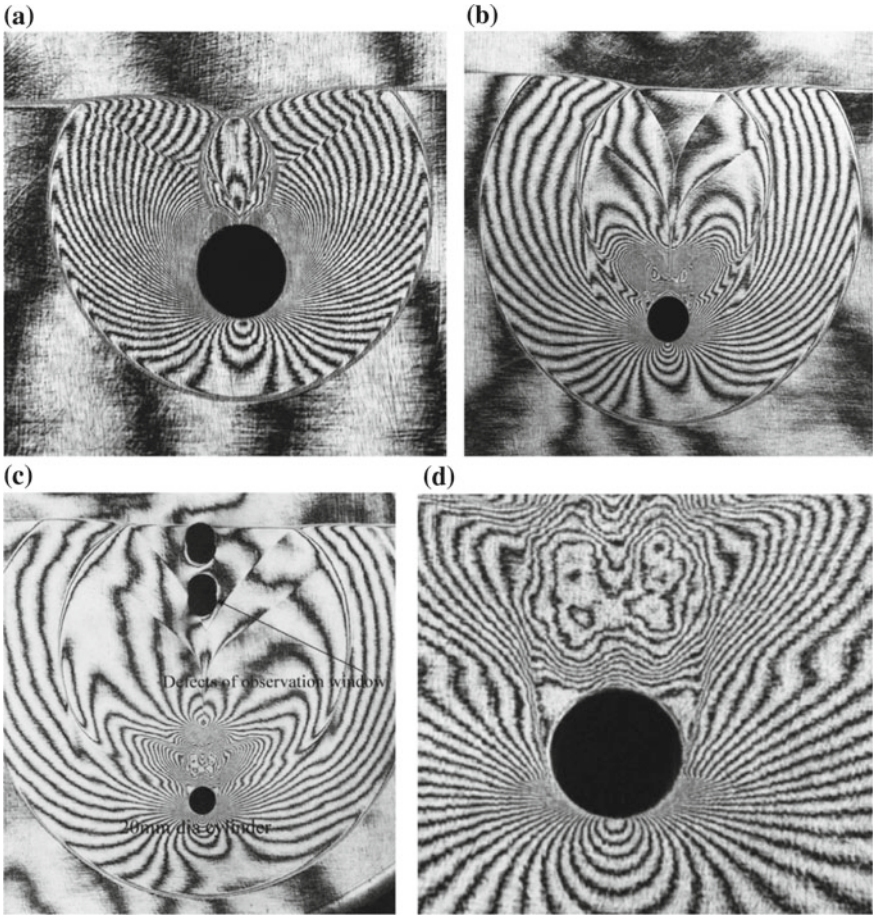

Fig. 4.5 Interaction of shock wave with a 20 mm diameter cylinder for Ms = 1.66 in CO_2 at 500 hPa, 290.2 K: **a** #89030204, Ms = 1.67; **b** #89030209, Ms = 1.66; **c** #89030211, Ms = 1.66 l; **d** enlargement of (**c**)

sidewall. The boundary layer was significantly bifurcated, which resulted in irregularly shaped fringes distributed at the frontal side of the cylinder.

4.1.4 Cylinder in Dusty Gas

In Fig. 2.14, the shock wave interaction with a 10 mm diameter cylinder installed in the test section of a dusty gas shock tube flow was investigated. The experiments were conducted in a 30 mm × 40 mm conventional shock tube which was already explained in Fig. 2.14. The dust particles under study were fly ashes of about 5 μm

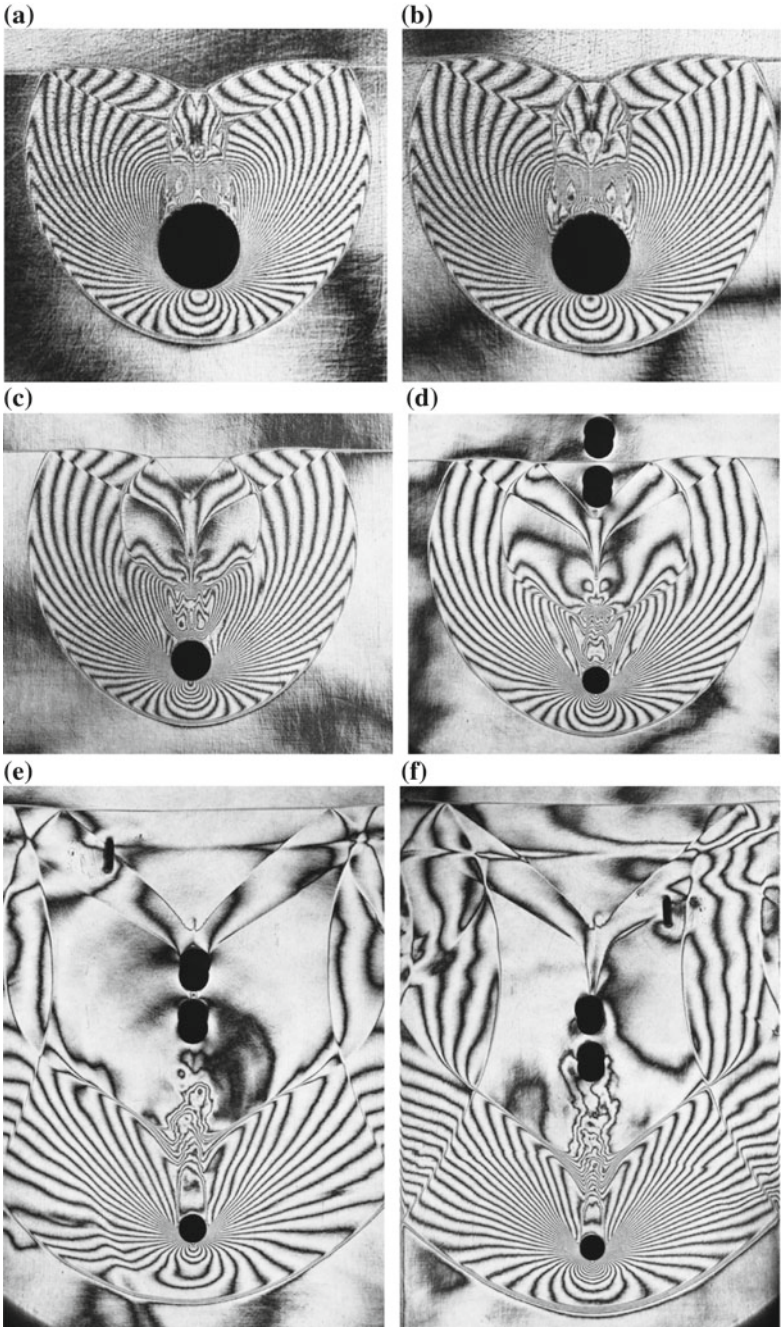

Fig. 4.6 Evolution of shock wave interaction with a 20 mm diameter cylinder for Ms = 2.20 in CO_2 at 300 hPa, 289.1 K: **a** #89030313, Ms = 2.21; **b** #89030312, Ms = 2.24; **c** #89030311, Ms = 2.24; **d** #89030403, Ms = 2.20; **e** #89030406, Ms = 2.28; **f** #89030404

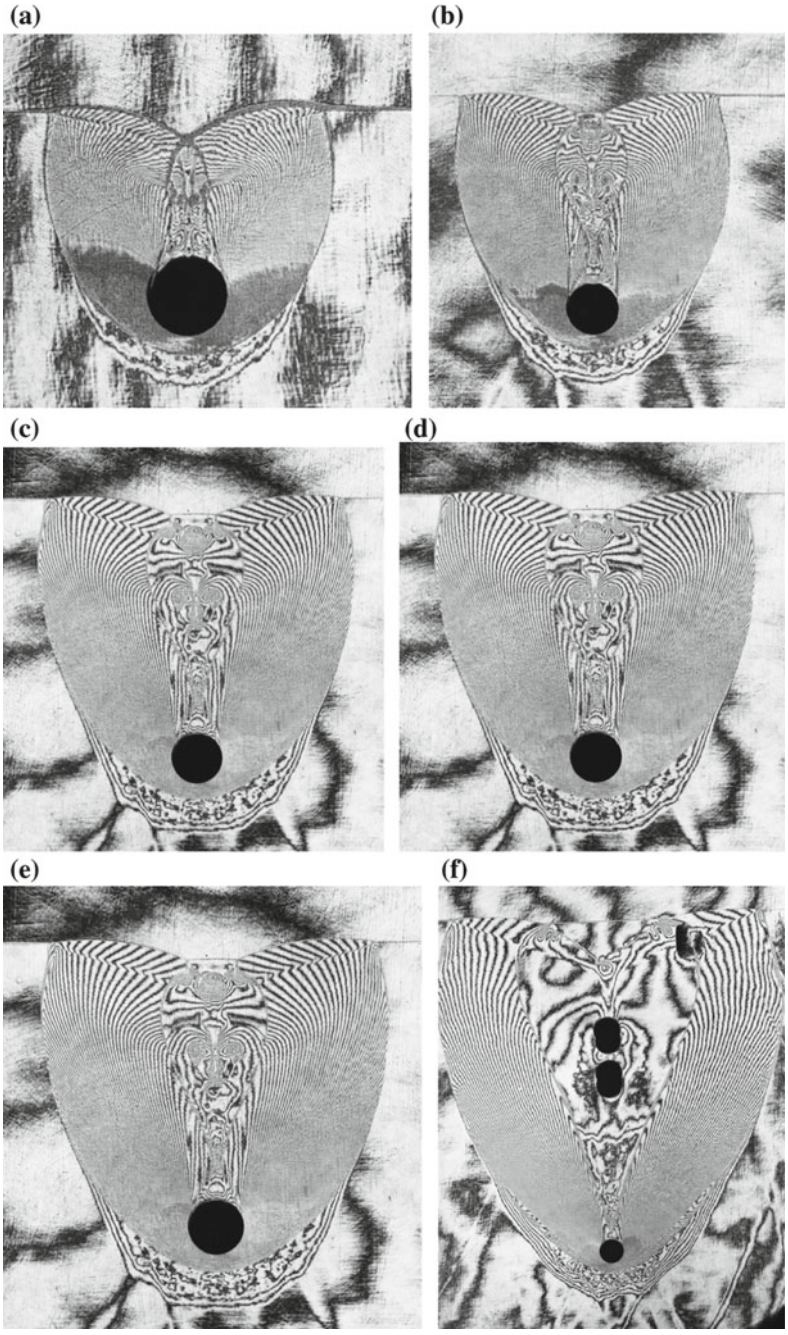

Fig. 4.7 Evolution of shock wave/cylinder interaction for Ms = 2.88 in SF_6 at 100 hPa, 290.2 K: **a** #89030606, 140 μs from trigger point, Ms = 2.86; **b** #89030604, 180 μs, Ms = 2.88; **c** #890306032301, 200 μs, Ms = 2.89; **d** #89030602, 220 μs, Ms = 2.24; **e** #89030705, 300 μs, Ms = 2.82; **f** #89030709, 300 μs, Ms = 2.88; **g** #89030711, 400 μs, Ms = 2.83; **h** #89030713, 450 μs, Ms = 2.81

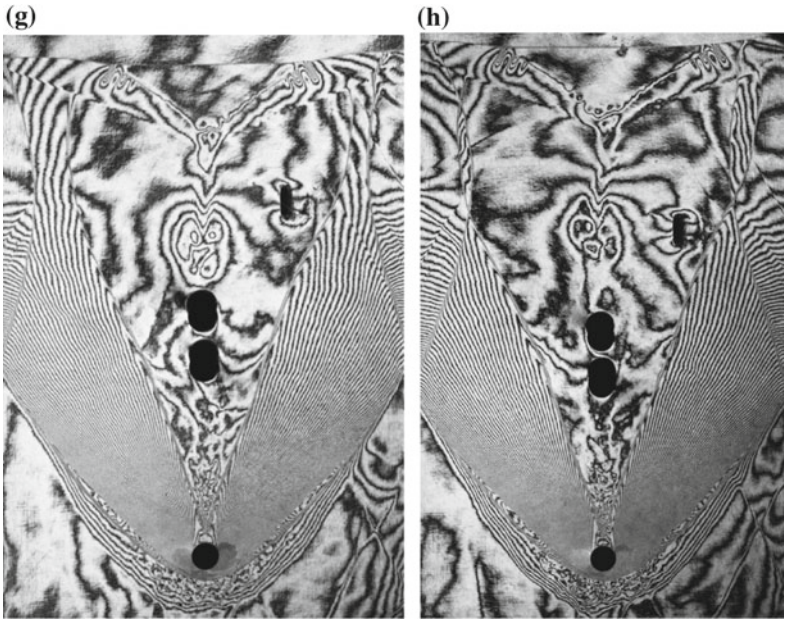

Fig. 4.7 (continued)

diameter. The dust loading ratio was defined as a ratio of mass of dust particle to the mass of air volume under study and was approximately 0.02 (Sugiyama et al. 1988). Figure 2.14 explained the dust circulation system: the dust particles were supplied from the dust hopper and recovered at the dump tank via a filter separating the dust particles from the air. The shock wave Mach number Ms ranges from 1.3 to 2.15 in air and the corresponding Reynolds number referred to the cylinder diameter ranges from 6.5×10^4 to 1.6×10^5, respectively.

Figure 4.9 show shock wave reflections over the cylinder for Ms = 1.3 in dusty air. The procedure of exposures were as follows: The room light was off and the holographic film was placed on the film holder. The first exposure was conducted before the dust circulation started. The film was covered with a thick cloth. The dust particles circulation was started and the room light was on. The dust concentration was continuously monitored. Several minutes later when the dust concentration reached to a given value, the dust circulation was stopped and the room light was off. Then second exposure was conducted. Meantime, the whole system was kept motionless except the dust circulation systems.

The present optical arrangement is similar to the shadowgraph and hence unreconstructed holograms in Fig. 4.9 are equivalent to direct shadow pictures. Figure 4.9a shows an interferogram of a dusty gas shock tube flow. But its fringe distribution never shows any deviations from that of dust free flows.

Grey regions around the cylinder surface on the unreconstructed holograms seen in Fig,4.9b show the dust free region in which the dust particles were removed due

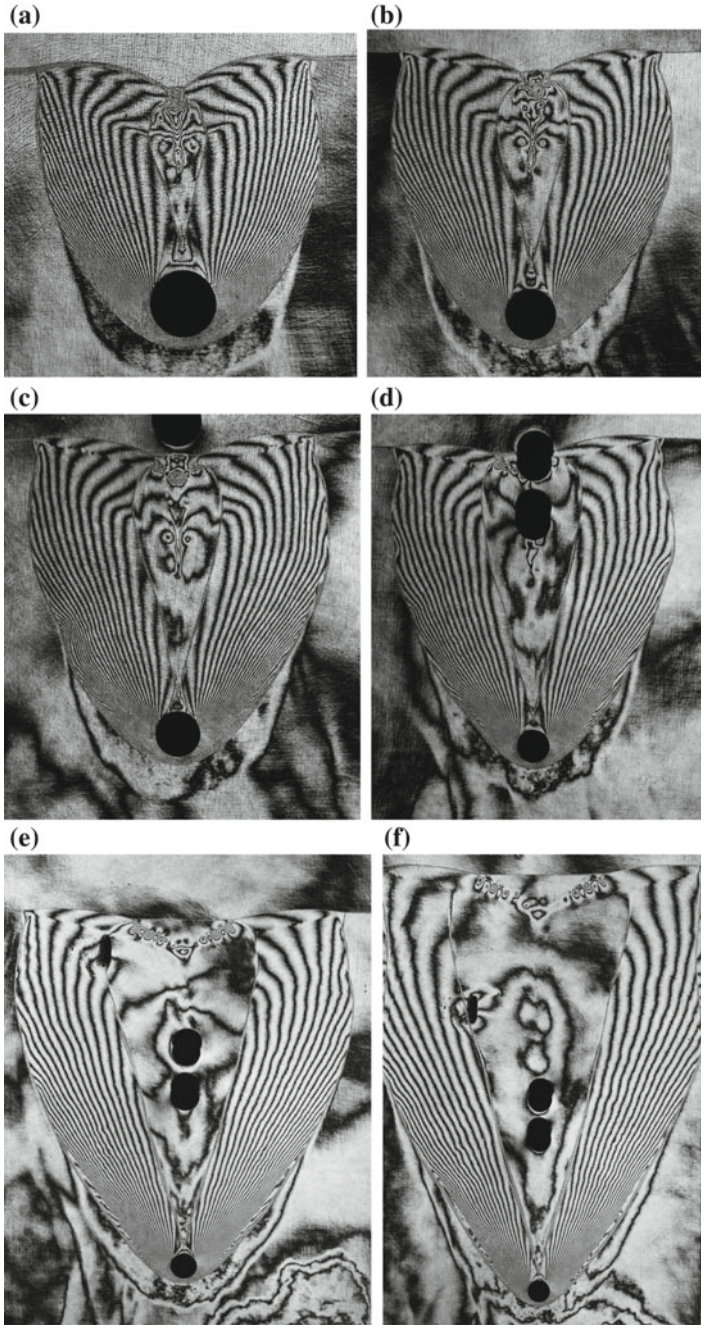

Fig. 4.8 Evolution of shock wave/cylinder interaction at later stage for Ms = 4.20 in SF_6 at 20 hPa, 290.2 K; **a** #89030718, 340 μs from trigger point, Ms = 4.18; **b** #89030717, 370 μs, Ms = 4.20; **c** #89030716, 400 μs, Ms = 4.22; **d** #89030715, 430 μs, Ms = 4.22; **e** #89030804, 580 μs, Ms = 4.05; **f** #89030805, 630 μs, Ms = 4.18

to centrifugal forces. At the second exposure, the *OB* carried all the holographic information which included the light absorption by the dust particles and the light scattering with the dust particles. Although the loading ratio was 0.02, the presence

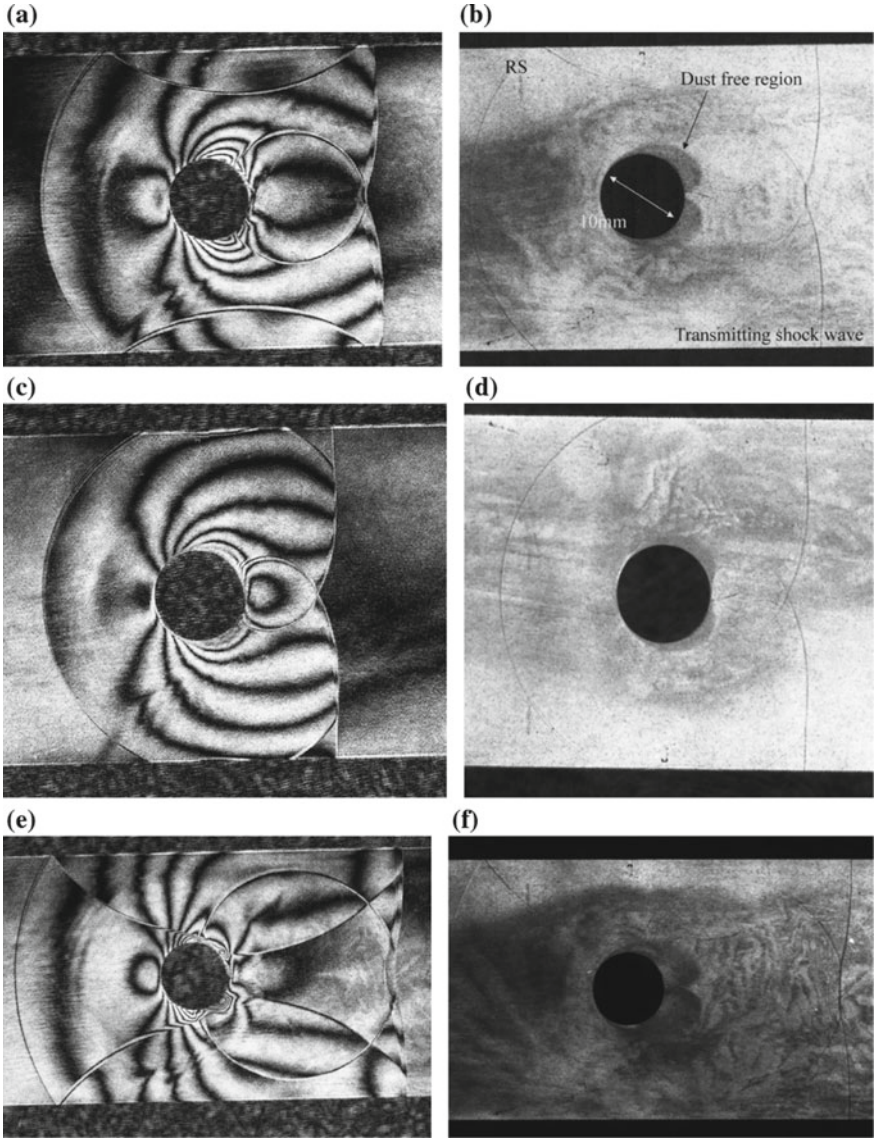

Fig. 4.9 Shock wave/cylinder interaction in a dusty gas at 1013 hPa, 186 K: **a** #86111207, 340 μs time from the trigger point, Ms = 1.320; **b** unreconstructed hologram of (**a**); **c** #86111202, Ms = 1.304; **d** unreconstructed hologram of (**c**); **e** #86111208, 350 μs, Ms = 1.320; **f** unreconstructed hologram of (**e**); **g** #86111504 400 μs Ms = 2.174; **h** unreconstructed and hologram of (**g**); **i** #86111507 360 μs Ms = 2.200; **j** unreconstructed hologram of (**i**)

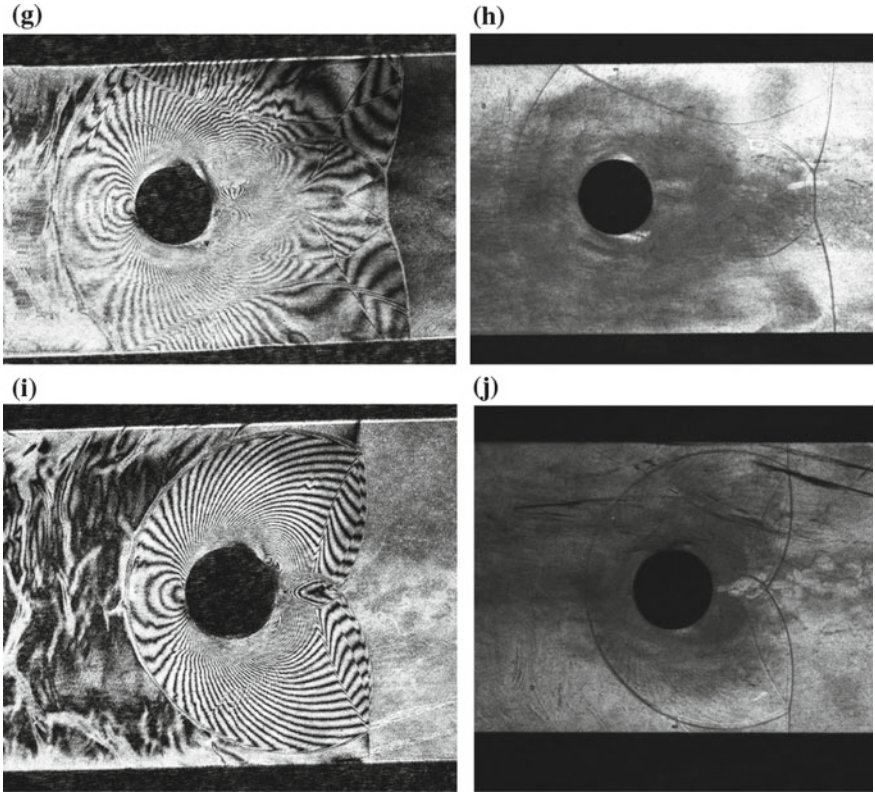

Fig. 4.9 (continued)

of the uniformly distributed dust particles scattered the laser beam. Due to the light scattering and diffraction from the particles, the background contrast looked brighter. This is the so-called the Mie scattering, which occurs when the particles having larger sizes than the light wave length scatter the source light. Then in the region where the dust particles were completely absent, the contrast of background was darker than the region in which the dust particles are uniformly distributed. Molecules in our sky scattered the sun light so that the sky is blue due to the so-called Rayleigh scattering. On the moon surface there are no air no dust particles in the sky and the sun light was not scattered. Then the sky looks dark.

The dust free region is created by vortex motion which was created due to the interaction of the reflected MS with the boundary layer developing along the cylinder surface. The flow in the vortex induced centrifugal forces strong enough to eject the dust particles. As the shock tube size is small, the proportion of vortex is large if compared with a large shock tube, for example, as shown in Fig. 4.2. Izumi (1988) numerically simulated the presence of the dust free region using the TVD scheme. The dust free region existed in nearly the same area as dark pattern appeared.

4.1.5 *Rotating Cylinder*

When a shock wave propagated along a rotating cylinder, the transition form a RR to SMR would be different along the cylinder surface depending on the direction of rotation. Just to observe this effect, a hollow cylinder of radius R made of aluminum alloy was rotated in the 60 mm × 150 mm diaphragm-less shock tube. Using an inverter the rotation speed ω was about 2000 rad/s to counter-clockwise rotation and the angular velocity Rω was about 50 m/s. Figure 4.10a shows the test section coated with the fluorescent paint on the shock tube wall and the cylinder surface. Diffuse holographic observation was conducted. In Fig. 4.10b, a result of double exposure diffuse holographic observation is shown. A shock wave of Ms = 1.19 propagated along the cylinder from left to right hand side. In Fig. 4.10b along the upper side, the flow direction was counter clockwise. The transition from RR to MR was retarded, whereas along the lower side the transition was promoted. The positions of triple points on the upper and lower sides were clearly observed and

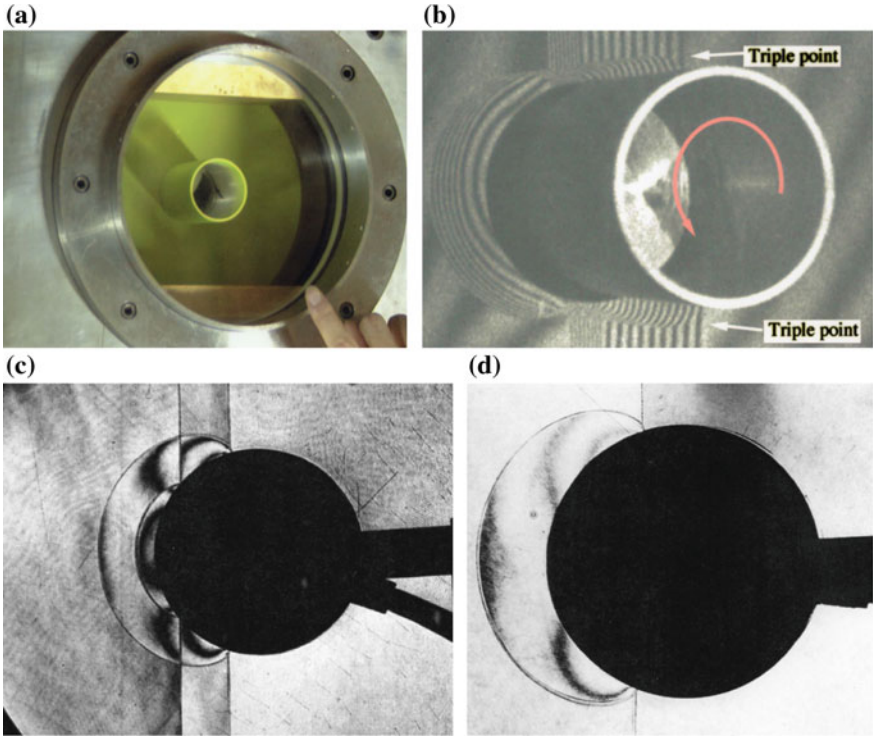

Fig. 4.10 Shock wave reflection from a counter-clockwise rotating cylinder 25,000 rpm of 50 mm diameter for Ms = 1.19 in air: **a** #99061502 l; **b** #99061503; **c**, **d** 70 mm cylinder (Yada 2001)

then the height of the MS was short on the upper side but was long on the lower side. The image of the reflected shock wave was projected on the sidewall (Sun et al 2001). Figure 4.10c, d show a double exposure interferogram conducted later stage (Yada 2001). The test piece was supported out side the test section. The visualization was conducted by the standard image hologram. The shapes of Mach stems on the upper and lower sides are slightly different indicating the difference of counter flows. This was a preparatory experiment and in the future the experimental system would be refined to double the rotation speed.

4.1.6 Partially Perforated Cylinders

Figure 4.11 show sequential observations of shock wave diffractions over a 100 mm diameter hollow cylinder made of brass. The cylinder had 10 mm wall thickness and was sandwiched between two acrylic observation plates of the test section of the 60 mm × 150 mm conventional shock tube for Ms = 1.165 in atmospheric air. As shown in Fig. 4.11a, along the upper side of the cylinder, fine slots of 1.0 mm wide and 1.5 mm interval were distributed and the lower part was a 10 mm thick brass tube connected to the slots. The slots were supported by 2.5 mm wide rims on the bottom. Then the ratio of opening was 40%. The structure was so delicate that it survived only for 50 runs.

Figure 4.11a shows the fine slot structure and the early stage of its interaction with the IS. The reflection pattern on the slotted surface was a subsonic regular reflection or in short SbRR, whereas it was a simple Mach reflection SMR on the solid surface. On roughened or perforated wedge surfaces, θ_{crit} is smaller than the solid surface. In Fig. 4.11b, c, the effect of slotted wall was distinguished comparing the reflection pattern between those along the upper and lower surfaces. The trajectory of the TP position along the slotted wall is lower than that along the solid surface.

As the test piece was not rigidly sandwiched between the observation windows so that the IS or the transmitting shock wave leaked through the narrow gap forming faint shadows of the shock wave leakage inside the cylinder.

The shock waves transmitting through the slots were reflected from the 2.5 mm wide rims at the bottom of slots. From the sequential observations, the critical transition angle θ_{crit} cn be readily estimated. The value of the resulting θ_{crit} is much smaller than that over solid cylinders.

Figure 4.12 show the evolution of shock wave for Ms = 1.52 propagating along the slotted cylinder. The transmitting shock wave through the slotted wall propagated obliquely inside the cylinder. The convexly shaped shock wave propagated toward the convex wall and its reflection formed the shock wave focusing as seen in Fig. 4.12j.

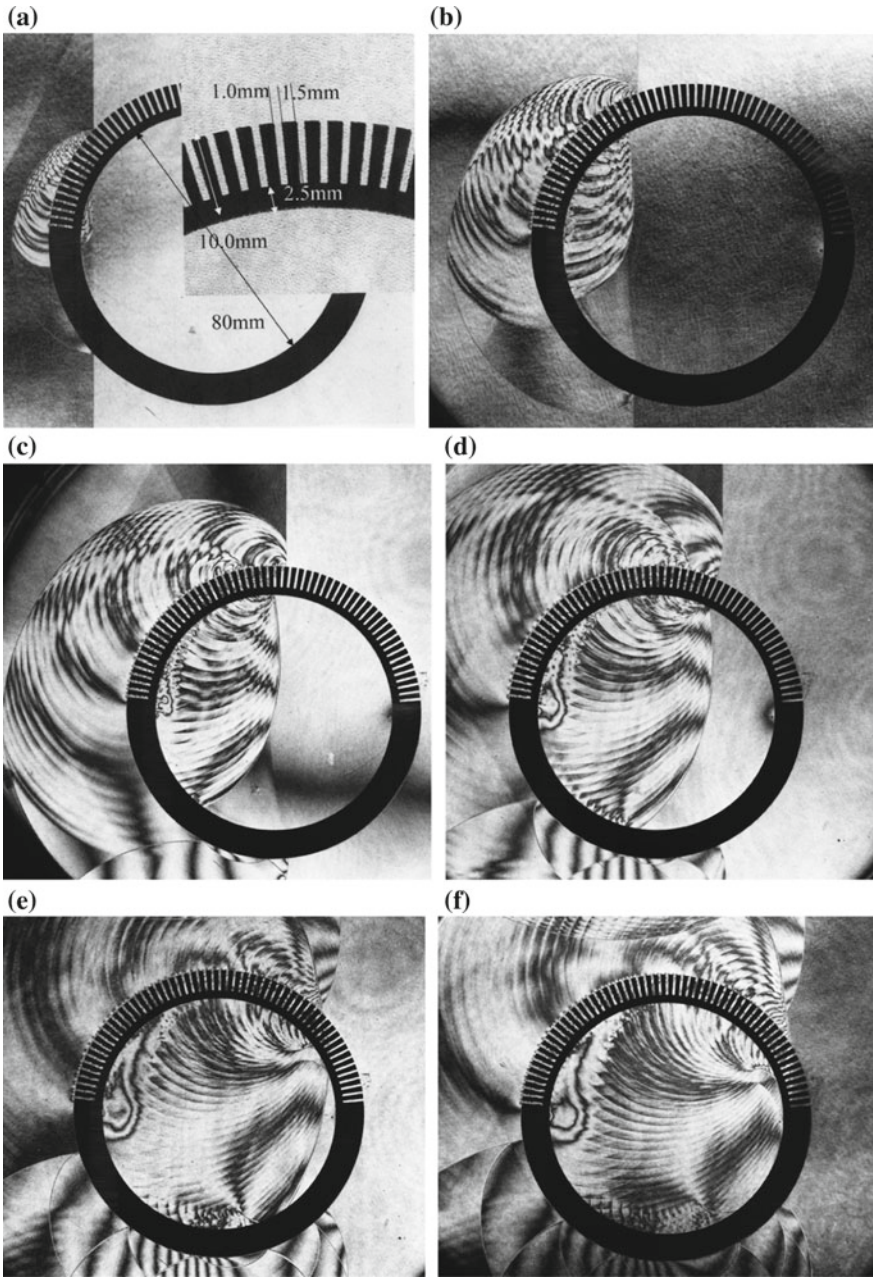

Fig. 4.11 Shock wave interaction with a perforated cylinder for Ms = 1.17 in atmospheric air, at 288 K: **a** #86121908, 275 μs from trigger time, Ms = 1.165; **b** #86121904, 375 μs, Ms = 1.171; **c** #86121911, 450 μs, Ms = 1.170; **d** #86121912, 475 μs, Ms = 1.170; **e** #86121914, 525 μs, Ms = 1.171; **f** #86121915, 550 μs, Ms = 1.161; **g** #86121916, 575 μs, Ms = 1.174; **h** #86121917 600 μs, Ms = 1.166

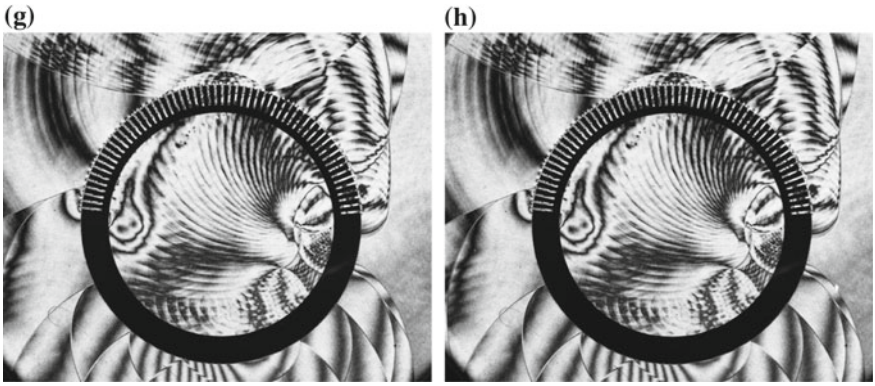

Fig. 4.11 (continued)

4.1.7 Tilted Cylinders

The shock wave interaction with a cylinder was one of the basic research topics of the shock wave research. The critical transition angle θ_{crit} of reflected shock waves over cylinders were experimentally determined. It would be a natural course of questions to know how the value of θ_{crit} over tilted cylinders would be different from that from the two-dimensional cylinders. Tilted cylinders were installed in the test section of the 60 mm × 150 mm conventional shock tube.

4.1.7.1 30° Tilted Cylinder

Figure 4.13a–f show sequential observation of reflection and diffraction of shock waves over a 30 mm diameter cylinders tilted 30°. The observations were conducted by the double exposure holographic interferometry for Ms ranging from 1.7 to 3.05 in air. All the reflection patterns are three-dimensional and show a SMR along the frontal side. If one can visualize the reflection patter along the sidewall and the other side of the tilted cylinder, the MS would reflect and causing complex wave interactions. Probably at this inclination angle of cylinder, the SMR will prevail. It will be interesting to reproduce the shock wave reflection over the tilted cylinders in the similar physical significance to reproduced the shock wave reflection over a tilted cone as shown in Sect. 2.1.7.5.

4.1.7.2 45° Tilted Cylinder

Figure 4.14a–c show sequential observations of the shock wave reflection and diffraction along a 45° tilted cylinder for Ms = 1.26 in air. Figure 4.14d–f show the sequential observation of the shock wave reflection and diffraction along a 45° tilted

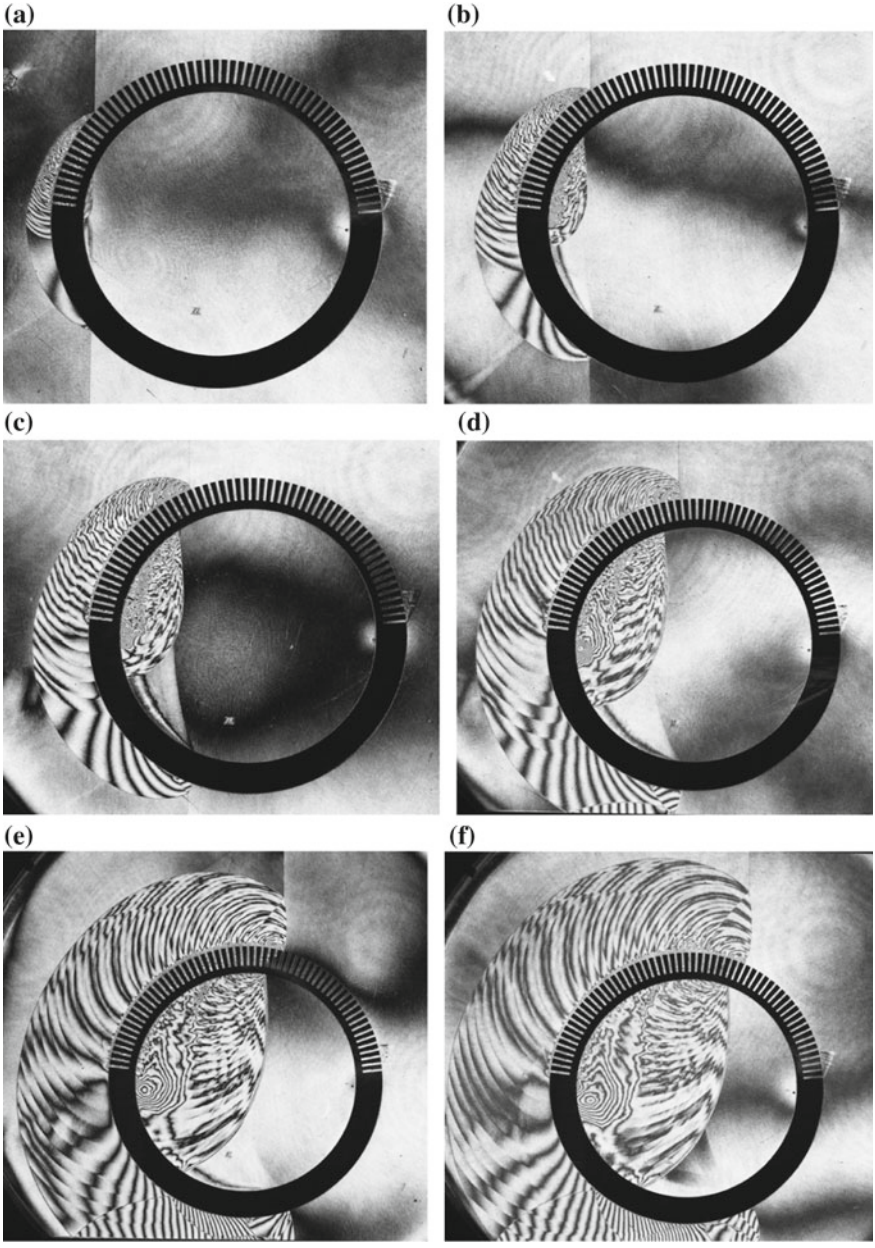

Fig. 4.12 Shock wave interaction with a perforated cylinder at Ms = 1.52 in air at 866 hPa, 289.0 K: **a** #86121918, 135 μs from the trigger point, Ms = 1.512; **b** #86121919, 155 μs, Ms = 1.512; **c** #86121920, 175 μs, Ms = 1.528; **d** #86121904,195 μs, Ms = 1.517; **e** #86121923, 235 μs, Ms = 1.522; **f** #86121924, 255 μs, Ms = 1.517; **g** #86121925, 275 μs, Ms = 1.517; **h** #86121926, 295 μs, Ms = 1.512; **i**#86121927, 315 μs, Ms = 1.513; **j** #86121930, 375 μs, Ms = 1.514

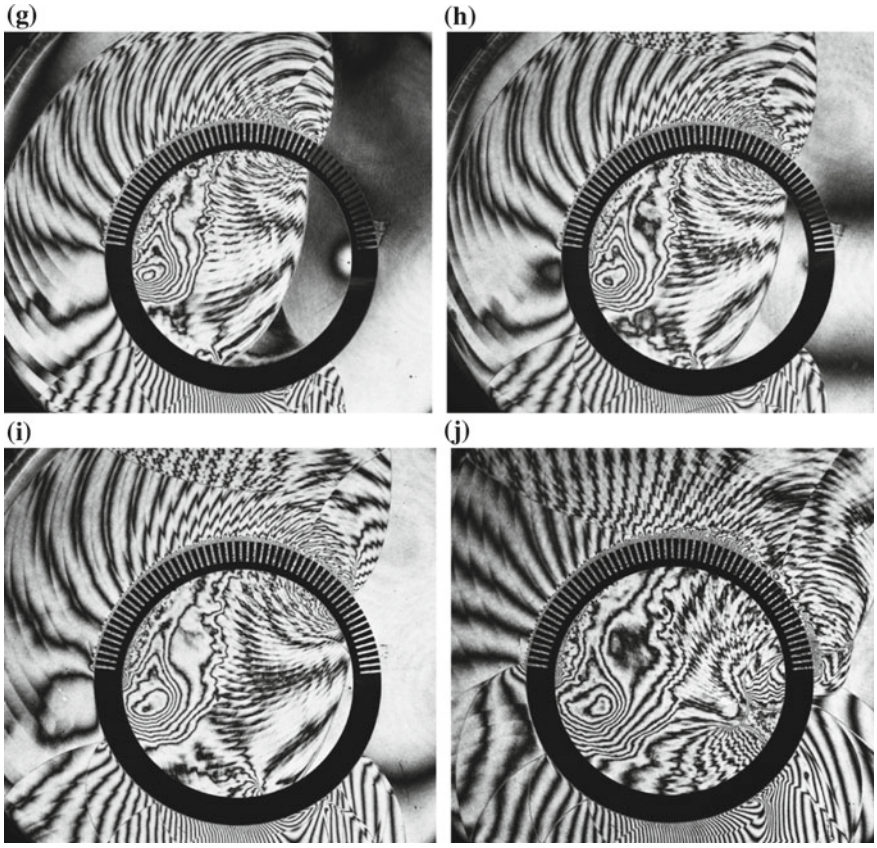

Fig. 4.12 (continued)

cylinder for Ms = 1.70. In Fig. 4.14a, the reflection pattern is a supersonic regular reflection SuRR, whereas in Fig. 4.14b–f, it is SMR. When the shock wave passed the top corner, the reflection pattern is SMR in a similar manner to the case of a convex double wedge. In Fig. 4.14a, a second discontinuous line visible closer to the tilted cylinder is a reflection of the incident shock wave from the side walls.

4.1.7.3 60° Tilted Cylinder

Figure 4.15 show sequential observation of the reflection and diffraction of shock waves over 60° tilted cylinder. The reflection patterns are SuRR all over the cylinder surface. In Fig. 4.15d, when the shock wave passed the corner of the flat top of the tilted cylinder, the reflection pattern became SMR. This trend is similar to

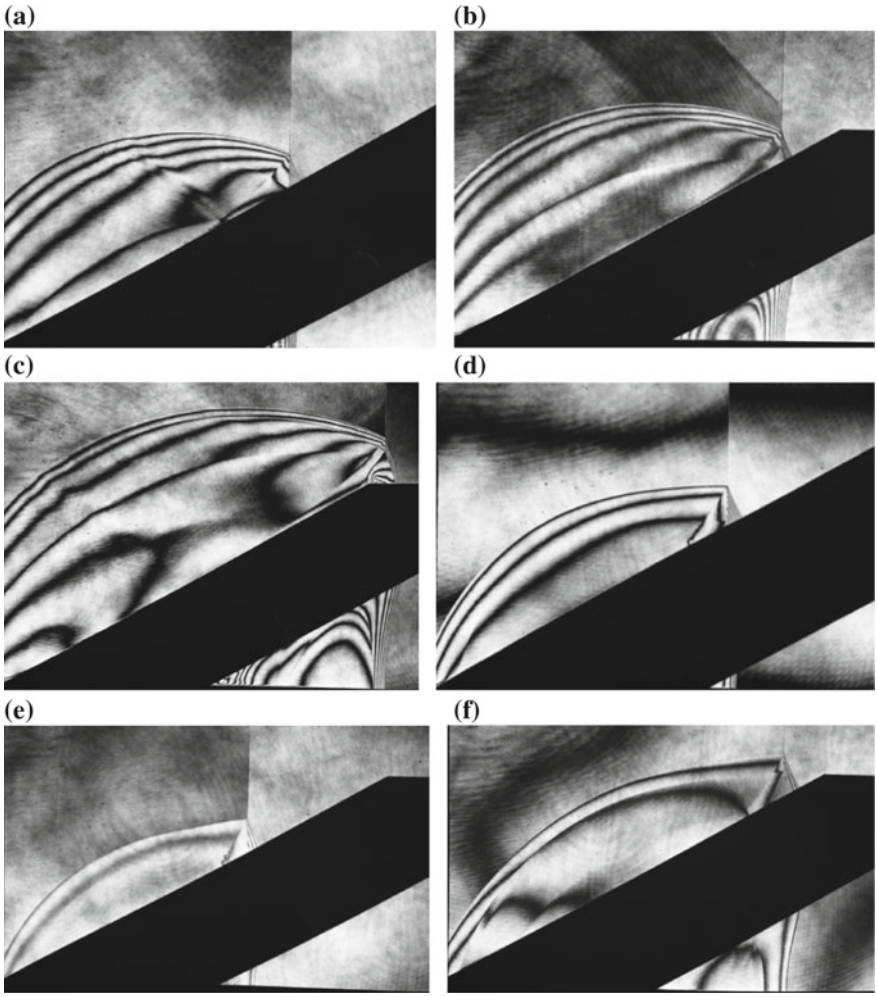

Fig. 4.13 Shock wave diffraction over a 30° tilted cylinder: **a** #87121501, Ms = 1.709, 500 hPa 292.7 K; **b** #87121502, Ms = 1.712, 500 hPa 292.7 K; **c** #87121503, Ms = 1.716, 500 hPa 291.8 K; **d** #87121511, Ms = 2.568, 130 hPa, 294.3 K; **e** #87121513, Ms = 3.067, 50 hPa, 294 K; **f** #87121512, Ms = 3.053, 50 hPa, 294 K

the shock wave propagation over a convex wall. Other than this effect, the reflected shock waves will transit to the SMR when the local inclination angle approaches to the critical transition angle θ_{crit} somewhere in the sidewall. However, there is no method to quantitatively visualize the transition of the reflected shock wave over tilted cylinder.

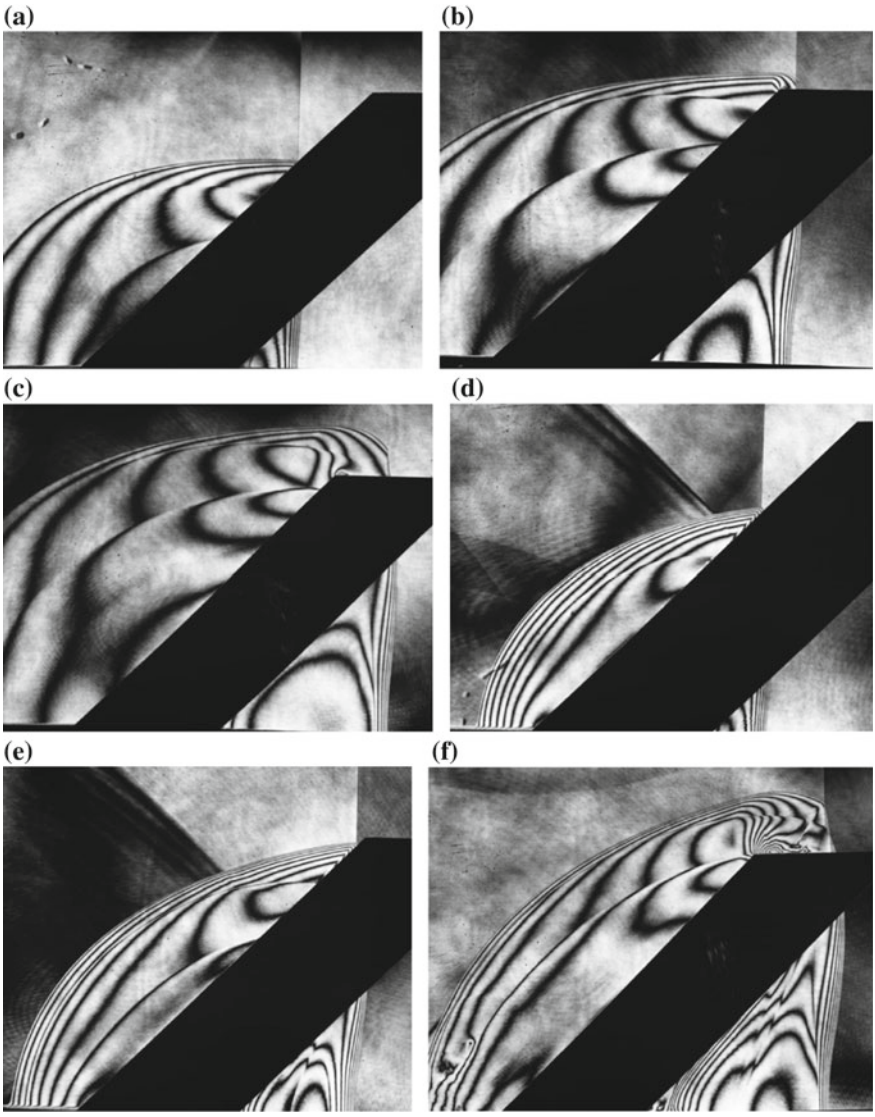

Fig. 4.14 Shock wave reflection and diffraction from a 45° tilted cylinder: **a** #87121204, Ms = 1.258, at 1013 hPa, 293.1 K; **b** #87121206, Ms = 1.259, 1013 hPa, 293.6 K; **c** #87121207, Ms = 1.263 at 1013 hPa, 293.6 K; **d** #87121211, Ms = 1.721 at 500 hPa, 293.0 K; **e** #87121212, Ms = 1.706, at 500 hPa, 291.0 K; **f** #87121213, Ms = 1.711 at 500 hPa, 292.6 K

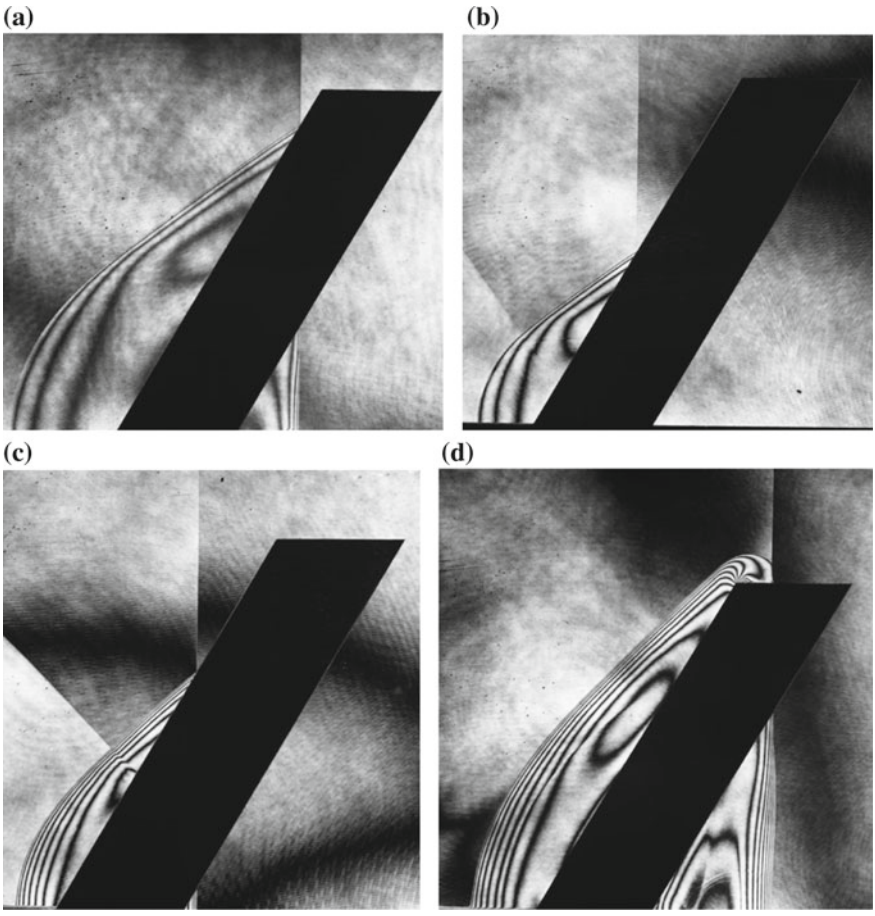

Fig. 4.15 Shock wave reflection and diffraction from a 60° tilted cylinder: **a** #87121109, Ms = 1.260 at 1013 hPa 294.4 K; **b** #87121110, Ms = 1.580 at 1013 hPa, 294.4 K; **c** #87121108, Ms = 1.713 at 500 hPa 294.5 K; **d** #87121106, Ms = 1.722 at 500 hPa 294.5 K

4.1.7.4 Truncated Vertical Cylinder

This is a very trivial experiment. The shock wave reflection and transmission over a truncated 30 mm diameter cylinder standing in a 60 mm × 150 mm shock tube was visualized. Figure 4.16 show the sequence of shock wave transitions for Ms—1.70. The reflection pattern is RR at the frontal surface but the pattern of the shock wave at the side and the top of cylinder is SMR. Unlike the shock interaction with a two-dimensional cylinder, the three-dimensional diffraction at the edge of the upright cylinder shows a complex pattern.

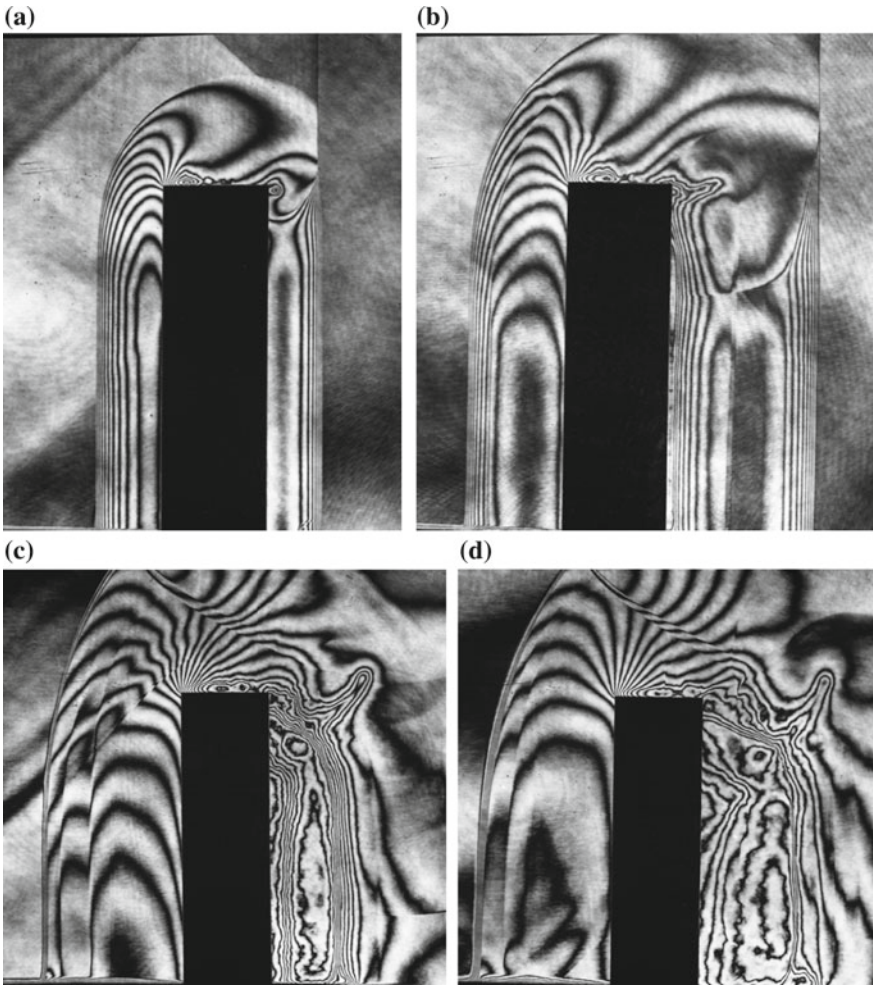

Fig. 4.16 Shock wave reflection and diffraction from truncated cylinder for Ms = 1.70 in air at 500 hPa, 295.1 K: **a** #87121001, Ms = 1.690; **b** #87121002, Ms = 1.696; **c** #87121004, Ms = 1.707; **d** #87121005, Ms = 1.878

4.1.8 Diffuse Holographic Observation Over a 60° Tilted Cylinder

This is a summary of the previous experiments. A 60° tilted cylinder was placed in the 60 mm × 150 mm conventional shock tube. The cylinder and the entire test section of the shock tube was coated with a fluorescent paint in the same way as the diffuse holographic observation. Then synchronizing the shock wave motion, the *OB* illuminated the shock tube test section from a slightly oblique direction. The *OB*

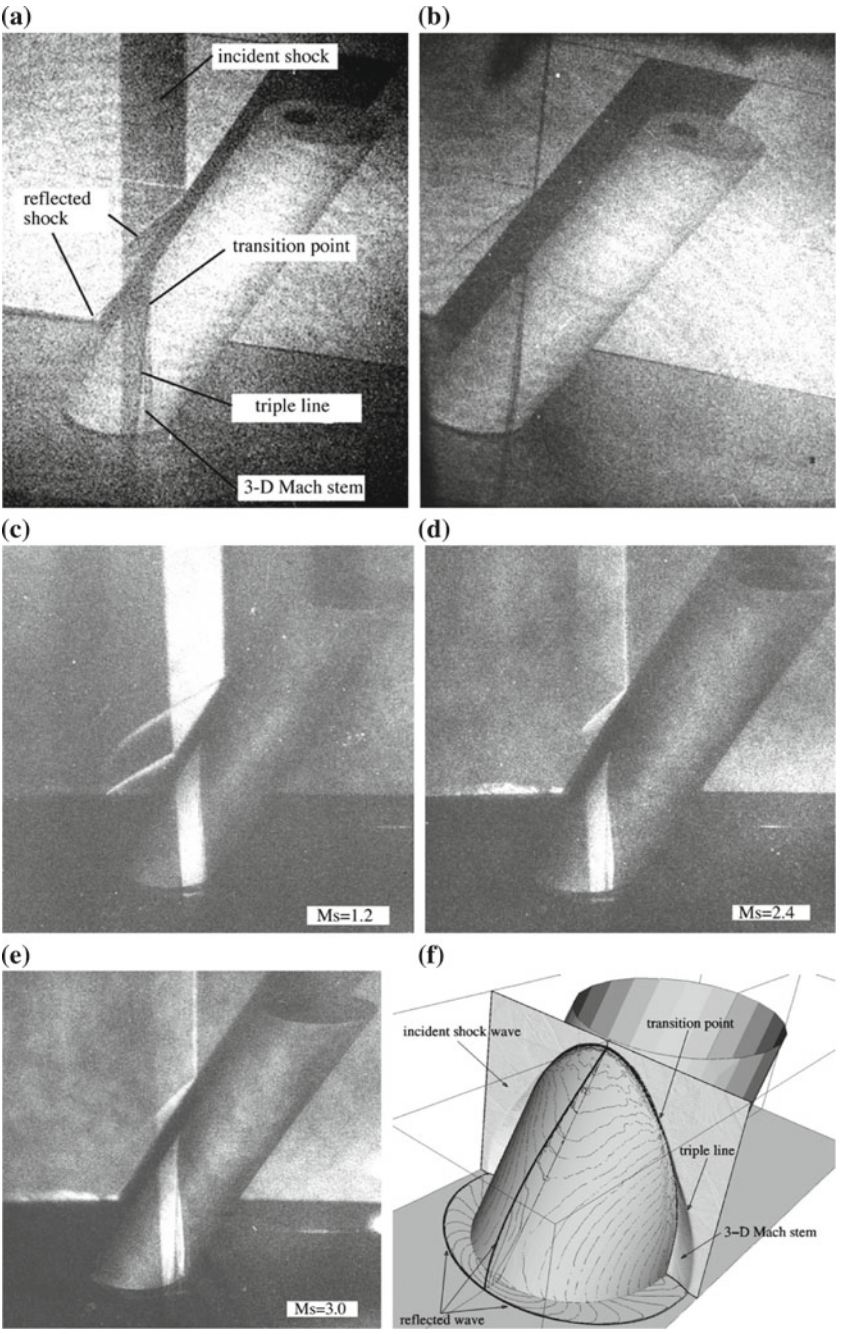

Fig. 4.17 Shock wave reflection over a tilted cylinder: **a** explanation of 60° tilted cylinder for Ms = 1.50; **b** holographic display of Ms = 1.50 different view angle; **c** holographic display of Ms = 1.20 different view angle; **d** holographic display of Ms = 2.4; **e** holographic display of Ms = 3.0; **f** determination of critical transition angle

was diffused passing a smoked glass plate. Then, the diffused *OB* reflected from the coated wall carried holographic information of the event and was recorded on a holo-film. Figure 4.17a is a reconstructed image which clearly shows the reflected shock wave from the cylinder for Ms = 1.5. In Fig. 4.17b, the reconstruction angle is normal to the view field (Timofeev et al. 1997).

A SuRR is observed on the frontal surface. The spot at which dark grey shadows discontinuously change the contract indicates the triple point and is clearly identified in Figs. 4.13, 4.14, 4.15 and 4.16. From these images, the θ_{crit} can be determined relatively accurately. Figure 4.17b–d show the three-dimensional images for Ms = 1.2, 2.4 and 3.0. The positions of the triple points on the side wall were determined. Timofeev et al. (1997) numerically identified the transition point of the shock wave reflection in Fig. 4.17f. Figure 4.17d shows that the transition from RR to SMR occurred at the angle similar to the transition over an elliptic cylinder. The boundary layer separations neither on the bottom wall nor on the truncated flat top are observed as seen in Figs. 4.13, 4.14, 4.15 and 4.16.

Figure 4.18 summarizes the θ_{crit} over the tilted cylinder against the inverse strength of shock wave ξ. The ordinate designates the θ_{crit} in degree and the abscissa shows inverse shock strength ξ. Red filled circles show the θ_{crit} over 60° tilted cylinder. A solid line shows the detachment criterion (Courant and Friedrichs 1948). Open circles show experimental results of wedges (Smith 1948) and black filled circles show the results of water wedges as discussed in Sect. 2.6.1. Filled triangles show the results of cones (Yang 1995). The transition over the tilted cylinder is 3-D phenomena but the results of θ_{crit} agree reasonably well with results over wedges, in particular, at stronger shock waves. For weak shock waves, the present results depart from the wedge and cone experiments.

This is a preliminary experiments of tilted 60° and should be compared with transition over concave wall experiments and to refer numerical results of solving Navier-Stokes Equations.

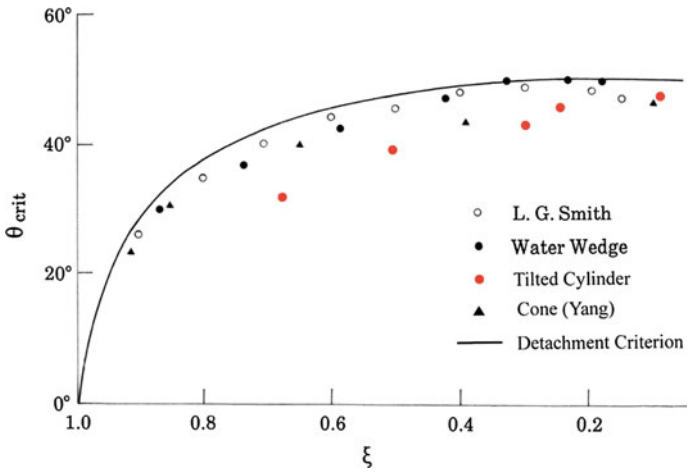

Fig. 4.18 Critical transition angle θ_{crit} versus inverse shock strength ξ

4.2 Unsteady Drag Force on a Sphere

Shock wave reflections over spheres are one of the fundamental experimental topics of shock wave dynamics. In the past there were efforts for measuring drag forces of shock wave laden spheres. The aim of this experiment is the direct measurement of a drag force of a shock laden 80 mm diameter sphere (Tanno et al. 2004).

Figure 4.19a shows a vertical conventional shock tube having about 7 m in total height. The shock tube is comprised of a 1.8 m long and 250 mm diameter high pressure chamber made of stainless steel and a 3 m long and 300 mm × 300 mm cross sectional low pressure chamber, a 600 mm long and 300 mm × 300 mm cross sectional test section made of stainless steel, and a 1.5 m long and 1.0 m diameter dump tank. A double diaphragm system is used. The reproducibility of the IS was poor. A 80 mm diameter sphere made of aluminum alloy was suspended vertically and placed in a test section positioned just before the dump tank. Figure 4.19b, c show the view of the shock tube and a 80 mm diameter sphere model suspended in the test section. In order to reliably measure the drag force, an accelerometer (Endevco piezoelectric accelerometer 2250A-10, 80 kHz) was installed in the sphere model.

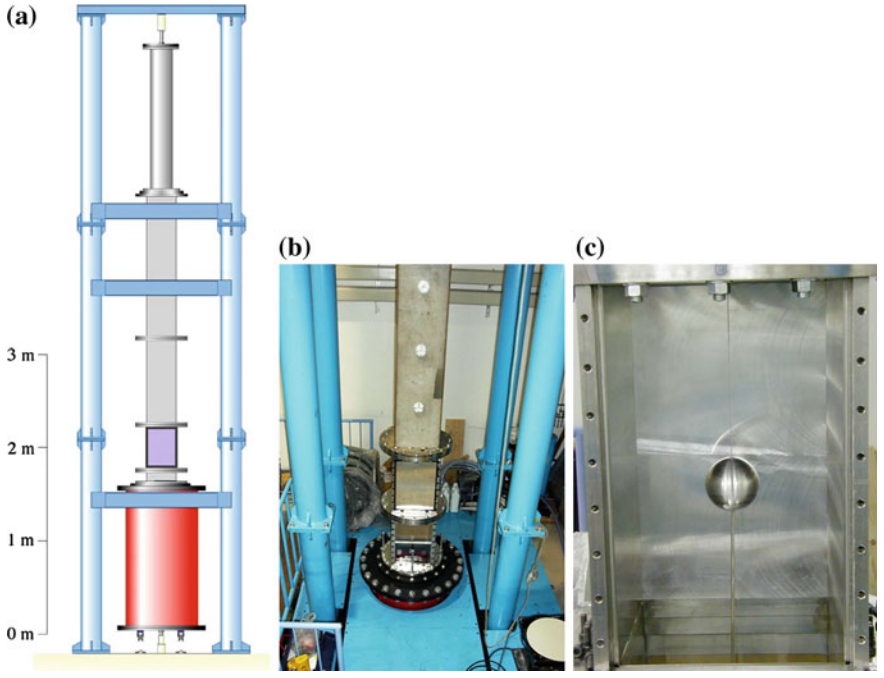

Fig. 4.19 Unsteady drag force of a 80 mm sphere: **a** facility; **b** vertical section; **c** 80 mm suspended sphere model

Heilig (1969) distributed pressure transducers over a 100 mm diameter cylinder installed in a shock tube and measured the drag force of a 100 mm diameter cylinder. He measured, for the first time, directly the time variation of pressure distributions over the cylinder exposed to the shock wave for Ms = 1.25 in air. He then reported that unsteady drag forces on a cylinder showed temporarily a peak value and monotonously reduced to the value of the drag force in the steady flow behind the shock wave. It was a question whether or not the unsteady drag force of a sphere might change in a similar fashion as that of cylinders. This was one of the motivations of the present experiment.

A 80 mm diameter sphere was suspended by a thin wire from just below the position of the double-diaphragm section along the center of the shock tube. When the shock impacted the sphere, the stress wave propagated along the wire and reflected back from the supporting point. The accelerometer installed in the sphere measured the acceleration of the shock laden sphere. The measurement would be terminated when the reflected stress wave from the support arrived at the sphere. However, the wire was so long that when the reflected stress wave arrived at the sphere, the sphere was already impinged by the reflected shock wave from the sidewall, which was the end of unsteady drag force measurement.

The output signal of the accelerometer was transmitted to the recorder through a cable from a hole on the bottom of the sphere. The uniform flow condition behind the IS was maintained for over 600 μs. This duration of time was long enough to measure the entire sequence of the drag forces. Applying the convolution function of the accelerometer to the output signal, the time variation of unsteady drag force was obtained. The convolution function was determined by measuring the frequency response of the accelerometer when it was impacted by a hummer.

Figure 4.20a–u show sequential schlieren pictures recorded by a high-speed video camera Shimadze SH 100 at 10^6 frame/s. The schlieren pictures were compared with interferometric images. The arrival of wavelets observed in Fig. 4.20e–n created pressure perturbations which were also detected by the accelerometer. In Fig. 4.20i–l, when the MS of the transmitting shock wave focused at the rear stagnation area, pressures detected by the accelerometer became maximal. In the two-dimensional shock wave cylinder interaction, the pressure at the rear stagnation point was just enhanced, when the MS merged. However, in the case of the sphere, it was focusing that the reflected MS merged at the rear stagnation point. Therefore, the pressure created by shock wave focusing was so high that the peak pressure exceeded the drag force. Hence, the drag force became negative. In Fig. 4.20s–u, the arrival of reflected shock waves from the sidewall terminated the presence of negative drag force. The measured drag force was compared with a result of the Navier-Stokes solver.

In Fig. 4.21, the measured drag force and numerical results were compared (Tanno et al. 2004). The ordinate denotes the drag forces in N and the abscissa denotes the elapsed time in μs. Green lines show output signal directly recorded by the accelerometer. Applying the deconvolution function to the measured force date, the unsteady drag force was deduced. The variation of the processed drag force was shown in a red line. The measured drag forces were compared with the numerical

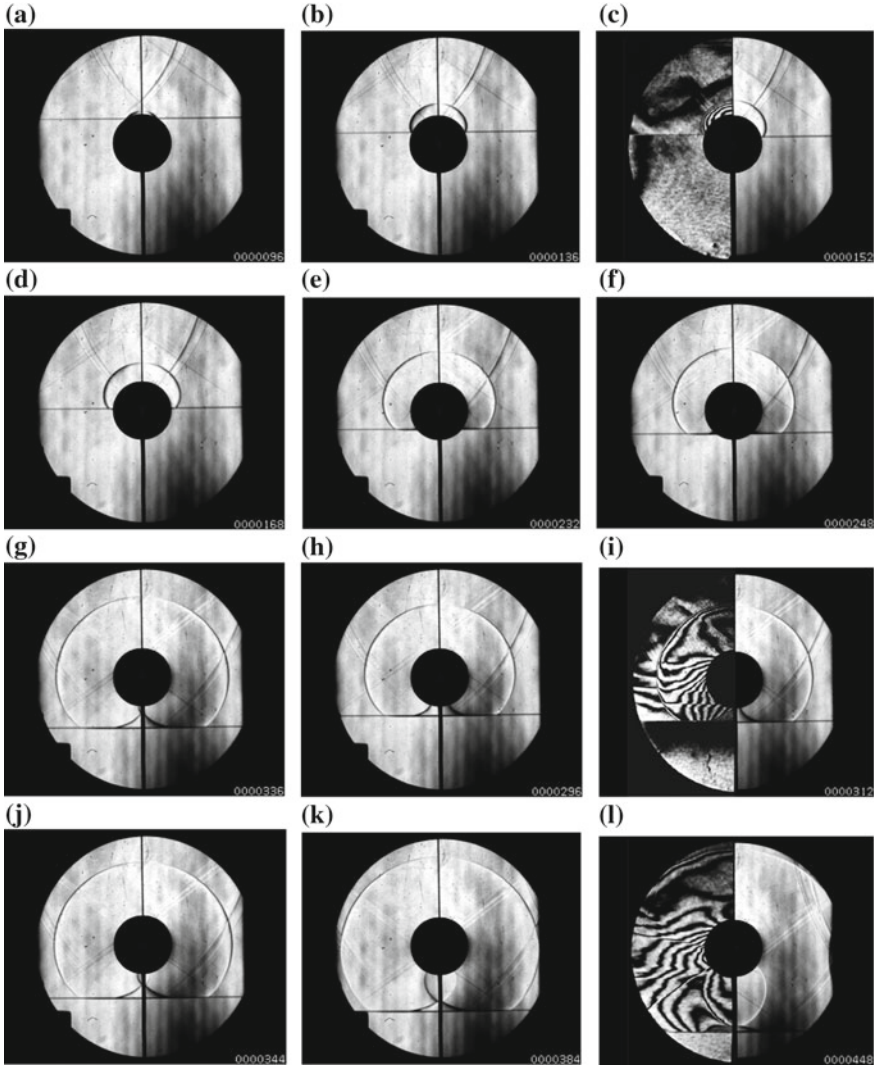

Fig. 4.20 Sequential observation of shock wave interaction with a 80 mm sphere for Ms = 1.25, comparison with interferograms

simulation solving the Navier Stokes Equations up to the elapsed time of 700 μs. The measured results agreed well with the result of the numerical simulation. The drag force had a maximum value then decreased to the value of the steady flow dag force. As seen in Fig. 4.20s–u, the focusing of MS at the rear stagnation point induced a peak pressure, and eventually the resulting drag force became negative. The negative drag force was maintained for about 150 μs. This is a unique feature of the sphere exposed by shock waves.

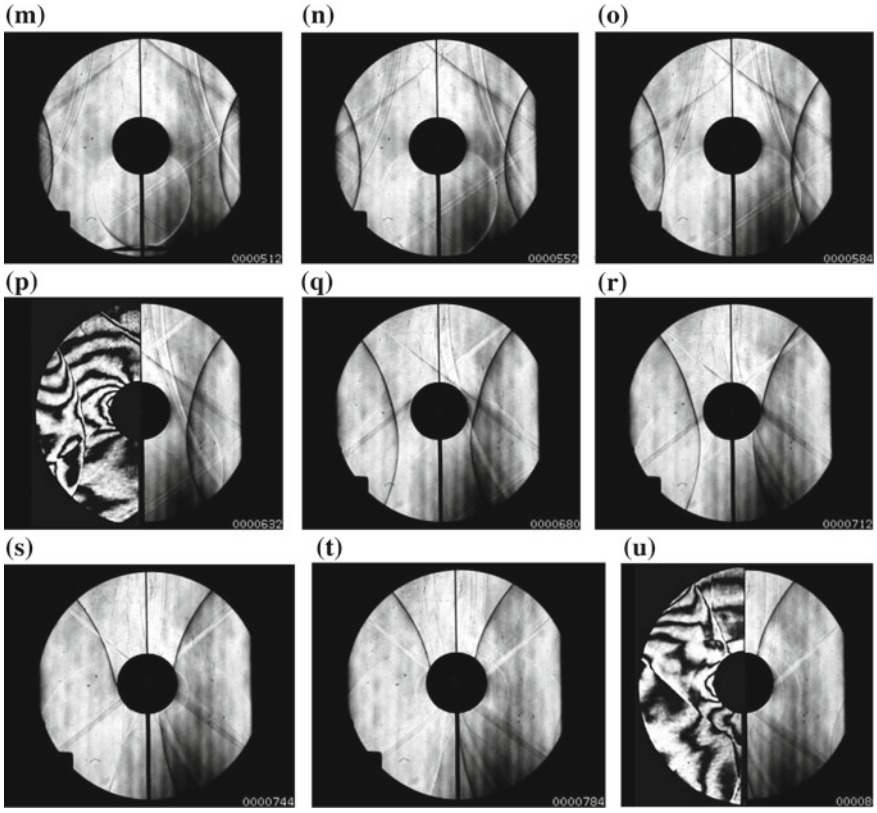

Fig. 4.20 (continued)

However, the presence of negative drag forces of shock laden spheres does not necessarily universally occur. Do dust particles of diameter about 5 μm as discussed in Sect. 4.1.4 have a negative drag forces when exposed to shock wave? Based on the comparison shown in Fig. 4.21, Sun et al. (2005) solved the Navier Stokes Equations and reproduced shock wave interaction for wide range of diameters of spheres ranging from 8 μm to 8 mm, in terms of the Reynolds number, Re ranging from 49 to 4.9×10^4 and Knudsen number, Kn ranging 9.4×10^{-2} to 9.4×10^{-6}.

The variation of so-defined drag coefficients, that is, the drag force normalized by condition behind the incident shock wave flow, was presented in Fig. 4.22. The ordinate denote the so-defined drag coefficient $C_D = 2f/\rho u^2 A$, where f, ρ, u, A are the drag force, the density and the particle velocity behind the shock wave, and the cross sectional area of the sphere under study, respectively. In conclusion, drag forces are consistently positive for spheres of 8 μm and 80 μm diameter whose Kn are still small enough to consider the continuum medium. The drag coefficient

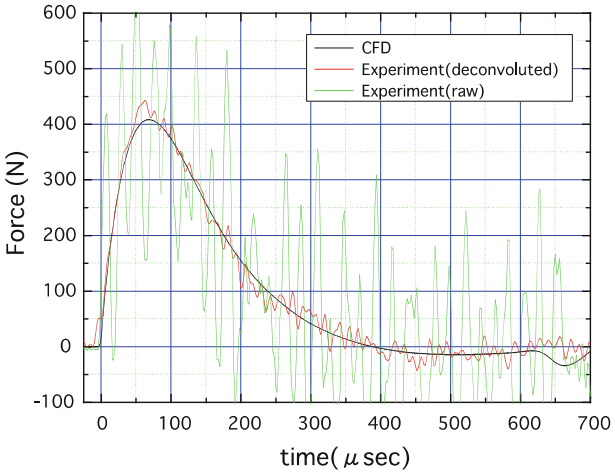

Fig. 4.21 Unsteady drag force over a 80 mm diameter sphere

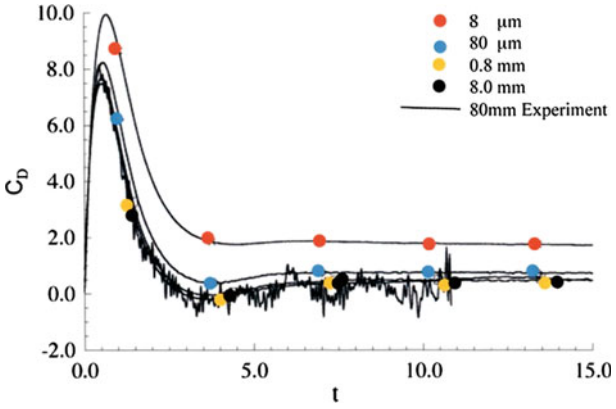

Fig. 4.22 Effect of time dependent drag force on diameter of sphere (Sun et al. 2005)

curves of 0.8 and 8 mm diameter spheres show nearly identical with the distribution in which negative pressure regions appear. It is noticed that in the shock wave interaction with a 10 mm diameter cylinder in the dusty gas shock tube flow, rarefied gas dynamic effects are negligible.

4.3 Shock Stand-off Distance Over a Free Flight Sphere

In supersonic steady flows, a bow shock wave appears in front of a blunt body. When the flow speed approaches to the sonic speed, a bow shock would appear in front of the blunt body. From an engineering point of view, wind tunnels can not technically generate a steady sonic flow. Hence, it is impossible to produce a bow shock wave in front of a blunt body in the sonic flows. However, shock tubes, in principle, can be a tool to produce transonic flows.

For testing such flows, a 10 mm diameter bearing ball was placed in the test section of the 60 mm × 150 mm conventional shock tube in order to produce a wide range of transonic flows. The flow Mach number behind an incident shock wave of Ms = 2.350 in air has a local flow Mach number is 1.10. Figure 4.23a, b show the interaction of the sphere with this flow at a delay time of 110 and 500 μs measured from the moment when the second exposure was synchronized with the shock wave, respectively. When the shock tube flow is used as a replacement of a transonic wind tunnel flow, the steady flow will be established at later time when the interaction of the incident shock wave with the model was suppressed. The conversion of shock tube flows in the 60 mm × 150 mm shock tube to a transonic flow can not be straightforward. This is so due to boundary layers developing along the shock tube walls as seen in Fig. 4.23b, and flow unsteadiness prevailing over the entire flow field. The shock tubes can never be a reliable transonic flow simulator (Kikuchi et al 2016).

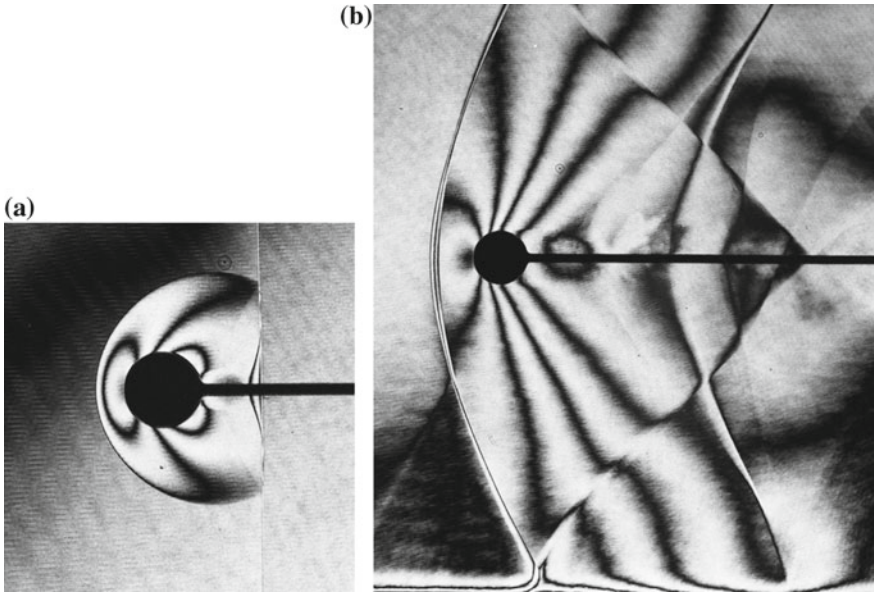

Fig. 4.23 Bow shock waves in transonic shock tube flows Ms = 2.350 in air at 150 hPa, 290.2 K, post-shock flow Mach number M = 1.10: **a** #83112215 110 μs from trigger point Ms = 2.350; **b** #83112220 500 μs

It was decided to use a ballistic range to accurately project spheres at transonic speed range. Figure 4.24a–c show a launching facility, a 40 mm diameter sphere and a 50 mm diameter sabot which can split into four pieces, and the arrangement to connect the launcher to a test chamber, respectively. A 40 mm diameter nylon sphere was contained in a 50 mm diameter polycarbonate sabot. The combination of the sabot and the sphere was launched into a ballistic range. Figure 4.24c explains the experimental arrangement. The sphere and sabot flew into the sabot remover through which sabot split into four pieces and sphere was separated from the sabot. Then sphere passed through the arrayed orifice plates removing blast wave. Eventually the sphere alone flew into the observation section and was visualized with 600 mm diameter interferometry.

Figure 4.25 shows 40 mm diameter spheres at the free flight speed ranging Ms = 0.986 to Ms = 1.104. In subsonic free flight, for example, in Fig. 4.25a–d, an apparent bow shock appears in front of the sphere. The waves observed were

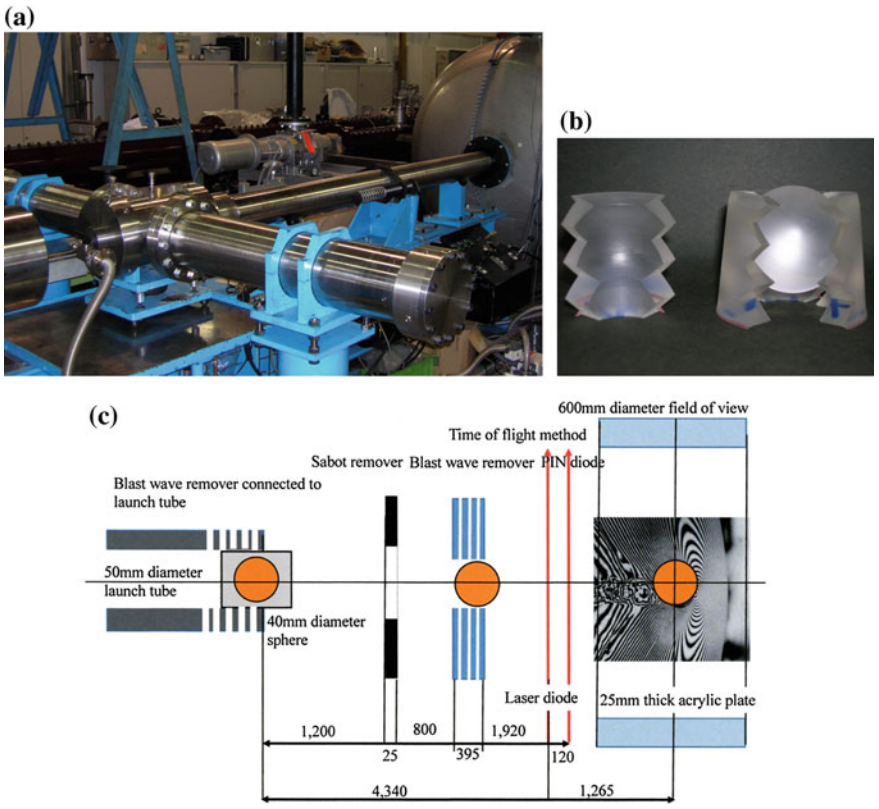

Fig. 4.24 Experimental setup of observing shock wave detachment distance from 40 mm sphere: **a** 10 mm bore gas gun; **b** a 40 mm nylon sphere and 50 mm policarbonate sabot; **c** experimental arrangement (Kikuchi et al. 2016)

subsonic, Ms < 1.0, which are not necessarily shock waves but must be a train of compression waves propagating at sonic speed. If a steady high subsonic wind tunnel flow, say Ms = 0.99, were operational, a bow shock wave might have been

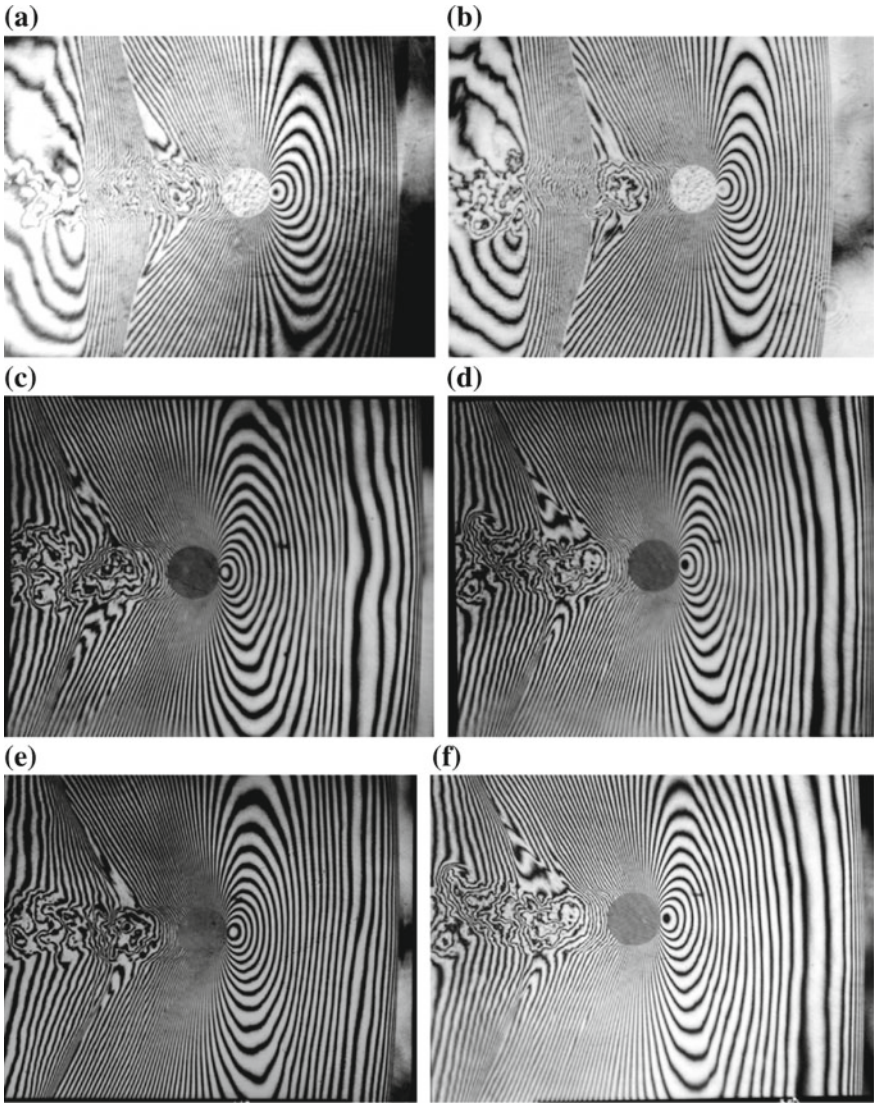

Fig. 4.25 Detached shock waves in front of a 40 mm diameter sphere: **a** Ms = 0.986, Re = 0.901 × 10^5; **b** Ms = 0.993, Re = 0.906 × 10^5; **c** Ms = 0.997, Re = 0.917 × 10^5; **d** Ms = 0.998, Re = 0.920 × 10^5; **e** Ms = 1.003, Re = 0.924 × 10^5; **f** Ms = 1.011; **g** Ms = 1.027, Re = 0.950 × 10^5; **h** Ms = 1.043, Re = 0.961 × 10^5; **i** Ms = 1.056, Re = 0.973 × 10^5; **j** Ms = 1.062, Re = 0.977 × 10^5; **k** Ms = 1.067, Re = 0.983 × 10^5; **l** Ms = 1.070, Re = 0.985 × 10^5; **m** Ms = 1.084; **n** Ms = 1.104

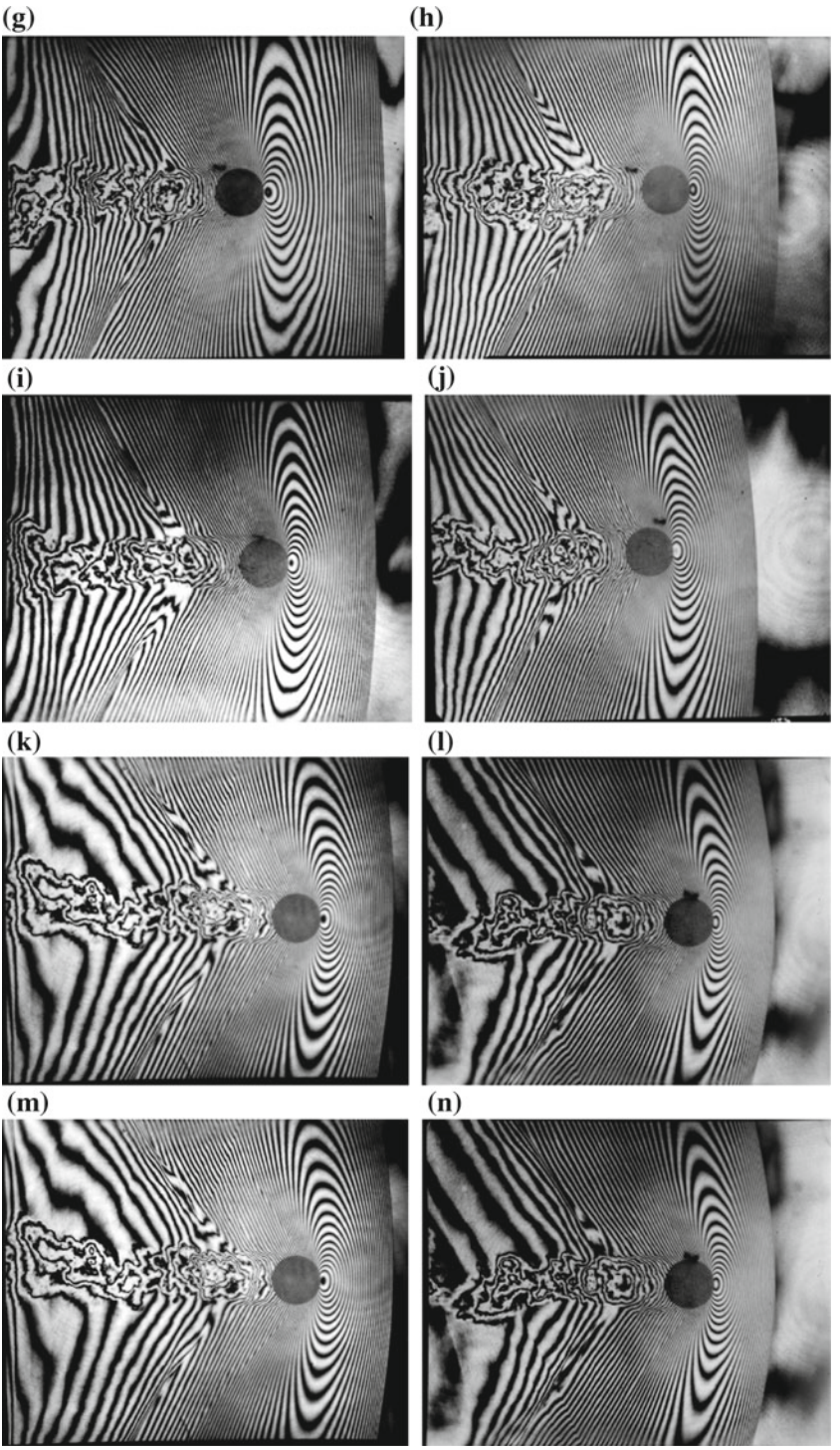

Fig. 4.25 (continued)

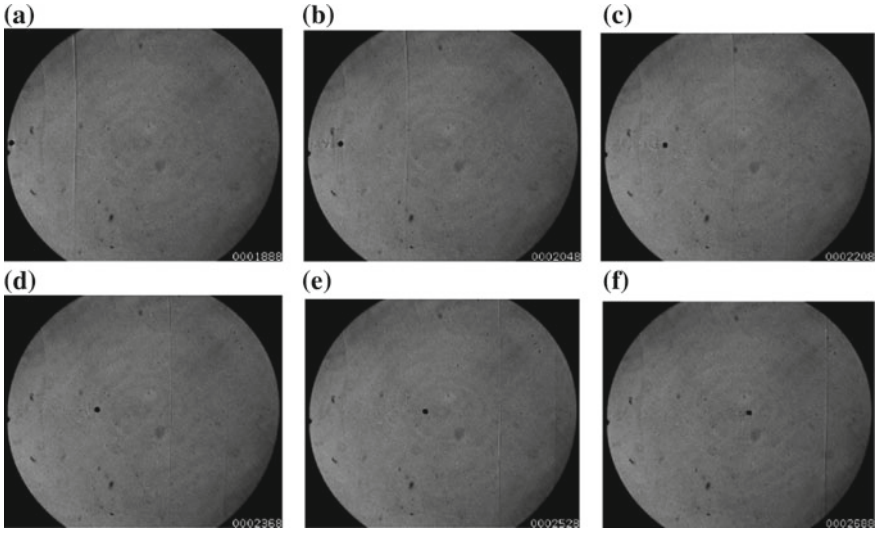

Fig. 4.26 Selective images of a 10 mm sphere in free flight for Ms = 0.949 at entry: **a** 60 μs; **b** 65 μs; **c** 70 μs; **d** 75 μs; **e** 80 μs; **f** 85 μs (Kikuchi et al. 2016)

observable in front of a blunt body. If a wind tunnel was operational at speed of Ms = 1 + ε, $0 < \varepsilon \ll 0.1$, the bow shock would be detached reasonably far away from a spherical model. However, no wind tunnel is operational at the flow Mach number unity. Such a wind tunnel is only imaginary. Such a critical condition never be stable, even if it may appear. In shock tube flows, it is nearly a useless effort to create a local flow Mach number of unity behind the incident shock waves.

Figure 4.26 show sequential direct shadow pictures of a 10 mm diameter bearing ball flying across a 500 mm view field. Images were recorded with the high speed video camera, Shimadzu SH100 at framing rate of 10^6 frame/s. The entry speed at the left hand side is Ms = 0.949, which attenuated to Ms = 0.939 at the right hand side. A detached wave was observed ahead of the sphere.

Figure 4.27 summarizes the trajectories of the shock wave and the sphere shown in Fig. 4.26. The ordinate denotes the flight distance in mm. The abscissa denotes the elapsed time in ms. Red filled circles show the position of the shock wave and green filled circles show the position of the sphere. Blue filled circles show the resulting shock stand-off distance δ/d. During a fight distance of 500 mm, the dimension-less stand-off δ/d increases from about 11 to 15, while the apparent Ms of the sphere changes from 0.949 to 0.939, and the shock wave propagates at the sonic speed. The shock stand-off distance δ/d increases with elapsing time. A bow shock wave is physically a train of compression wave propagating at sonic speed.

In Fig. 4.28, results of previous visualizations are summarized. The ordinate denotes the dimensionless stand-off distance δ/d and the abscissa denotes the spheres' Ms in free flight. Red filled circles show interferometric images of the 40 mm diameter spheres and blue filled circles show the 10 mm diameter spheres

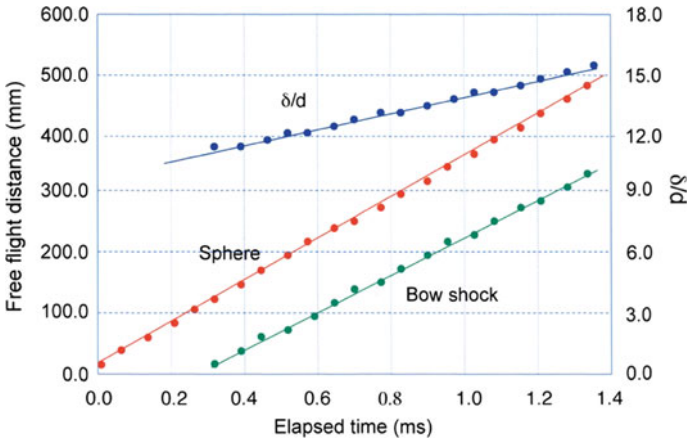

Fig. 4.27 Time variation of the detachment distance and the trajectories of the detached shock wave and the sphere (Kikuchi et al. 2016)

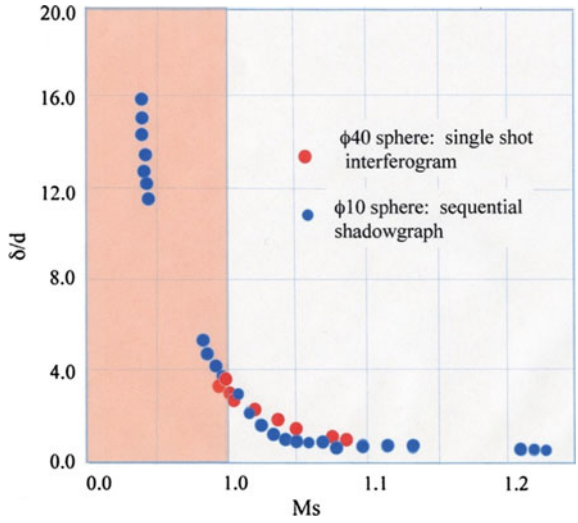

Fig. 4.28 Shock stand-off distance versus Ms (Kikuchi et al. 2016)

recorded by a high-speed video camera. It is noticed that bow shock waves appeared even in subsonic flows, Ms < 1. 0 The trend of data collected with 40 and 10 mm spheres agreed well with each other. Surprisingly the bow shock waves continuously crossed the boundary of Ms = 1.0 as if a bow shock exists in front of subsonic moving spheres.

Professor Ben-Dor once told the author his experience in a battle front. While listening to booms induced by a gun shell, soldiers immediately judged whether or not it would land close to them or a distance away. The sonic booms were composed of trains of compression waves driven by gun shells propagating at high subsonic speed. In short, booms were detached at reasonably long distance from the gun shells. Figure 4.28 demonstrates that in unsteady flows sonic waves exist in front of subsonic moving blunt bodies.

A train of compression waves and a weak shock wave are both visualized as a discontinuous sharp line and it is hard to distinguish between weak shock waves and a train of compression waves.

4.4 Elliptic Cylinders

Elliptical cylinders of the major radius of 40 mm and the minor radii of 40 mm, 20 mm, and 10 mm, respectively, were installed in the 60 mm × 150 mm conventional shock tube in a similar manner as shown in Fig. 4.1. The 40 mm cylinder was equivalent to an elliptical cylinder having the ratio of the major radius to the minor radius of 1:1. Therefore, in the series of the present experiments, the shock wave interaction with ellipse of their aspect ratios from 4:1. 2:1, 4:3, 1:1 were visualized for Ms = 1.30 in air and the Reynolds number referred to the major diameter $Re = 5.0 \times 10^5$.

4.4.1 4:3 Elliptic Cylinders

Figure 4.29a–d show the evolution of shock wave reflections from the 4:3 elliptical cylinders for Ms = 1.30 in atmospheric air. The reflection patterns are similar to those shown in Fig. 4.2. Figure 4.30a–g show the identical case for Ms = 2.60 at 120 hPa in air. In Fig. 4.30a, the reflection pattern is RR at the frontal side of the ellipse. In Fig. 4.30b it becomes SMR at the equator. It is noticed that since the flow behind the shock wave for Ms = 2.60 is supersonic, the reflected shock wave departs gradually from the frontal side of the ellipse with elapsed time and reaches a consistent shock stand-off distance δ. This trend is clearly observable in Fig. 4.30f, g. Slightly irregular pattern visible along the reflected shock wave shows the bifurcation of the reflected shock wave which is created due to its interaction with the boundary layer developing along the shock tube side wall. The bifurcation of the reflected shock wave will be discussed in the Sect. 4.6.2 (Mark 1956). In Fig. 4.30e–g, the SL

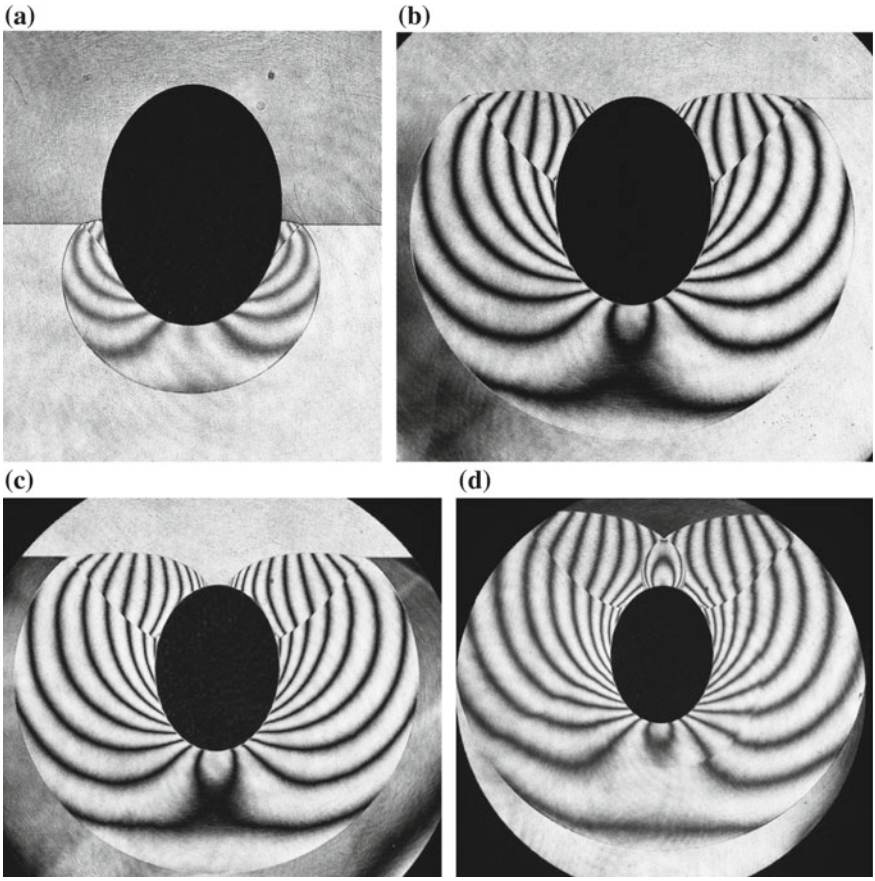

Fig. 4.29 The evolution of shock wave interaction with a 4:3 elliptical cylinder interaction for Ms = 1.30 in atmospheric air at 298.7 K attack angle $\alpha = 0°$: **a** #85082816, Ms = 1.294; **b** # 85082820, Ms = 1.302; **c** #85082822, Ms = 1.306; **d** #85082902, Ms = 1.298

emanating from the TP intersects with the ellipsoid surface and its interaction with the reflected MS forms complex wave interactions. The fringe pattern reminds one of deformation of a barking tiger face.

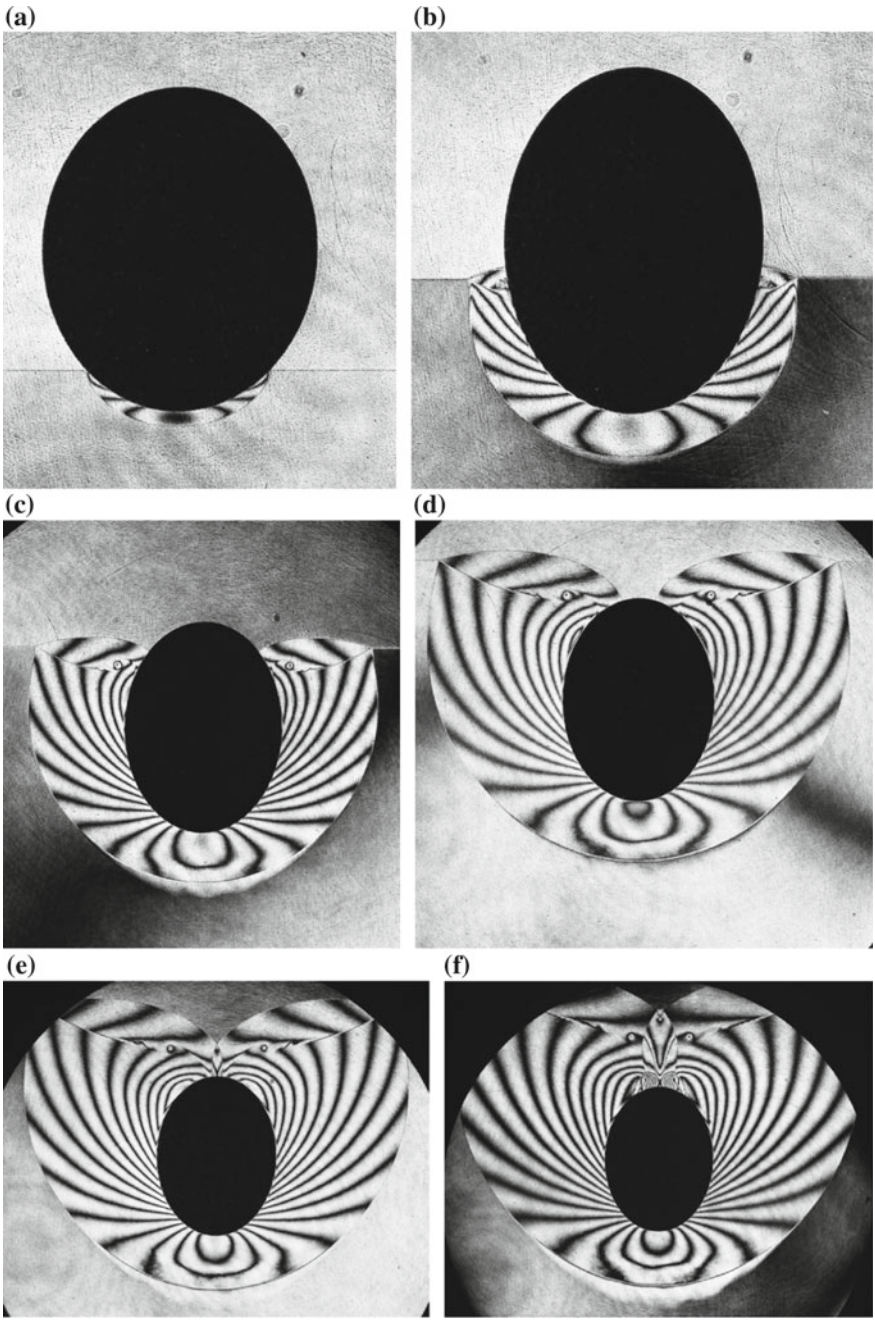

Fig. 4.30 The evolution of the shock wave interaction with a/4:3 elliptical cylinder interaction for Ms = 2.60 in air at 120 hPa, 298.7 K, attack angle $\alpha = 0°$: **a** #85082922, Ms = 2.605; **b** #85083007, Ms = 2.593; **c** 85083006, Ms = 2.613; **d** #85083012, Ms = 2.578; **e** #85083013, Ms = 2.583; **f** #85083014, Ms = 2.584; **g** enlargement of (**f**)

Fig. 4.30 (continued)

4.4.2 2:1 Elliptic Cylinders

Figure 4.31a–g show the evolution of shock wave reflections from the 2:1 elliptical cylinder for Ms = 1.30 in atmospheric air. The reflection patterns are similar to those observable in Fig. 4.29. Figure 4.32a–f show the identical case for Ms = 2.60 at 120 hPa in air. The reflection patterns are similar to the patterns observed in Fig. 4.30.

Figures 4.33 and 4.34 show the evolution of the shock wave reflection from a 2:1 elliptic cylinder for Ms = 1.70 in air with attack angles of $\alpha = 5°$ and 10°, respectively. The interaction of the reflected MS with the boundary layer developing along the ellipse is enhanced with elapsing time and with increase in the attack angle. Figure 4.33c–d show development of vortices at the rear side of the ellipse. Figure 4.33d–i show the vortices shedding from the rear side.

A similar trend is observed in Fig. 4.33 for Ms = 1.70 and $\alpha = 5°$; it is also observed in Fig. 4.34 for Ms = 1.70 and $\alpha = 10°$.

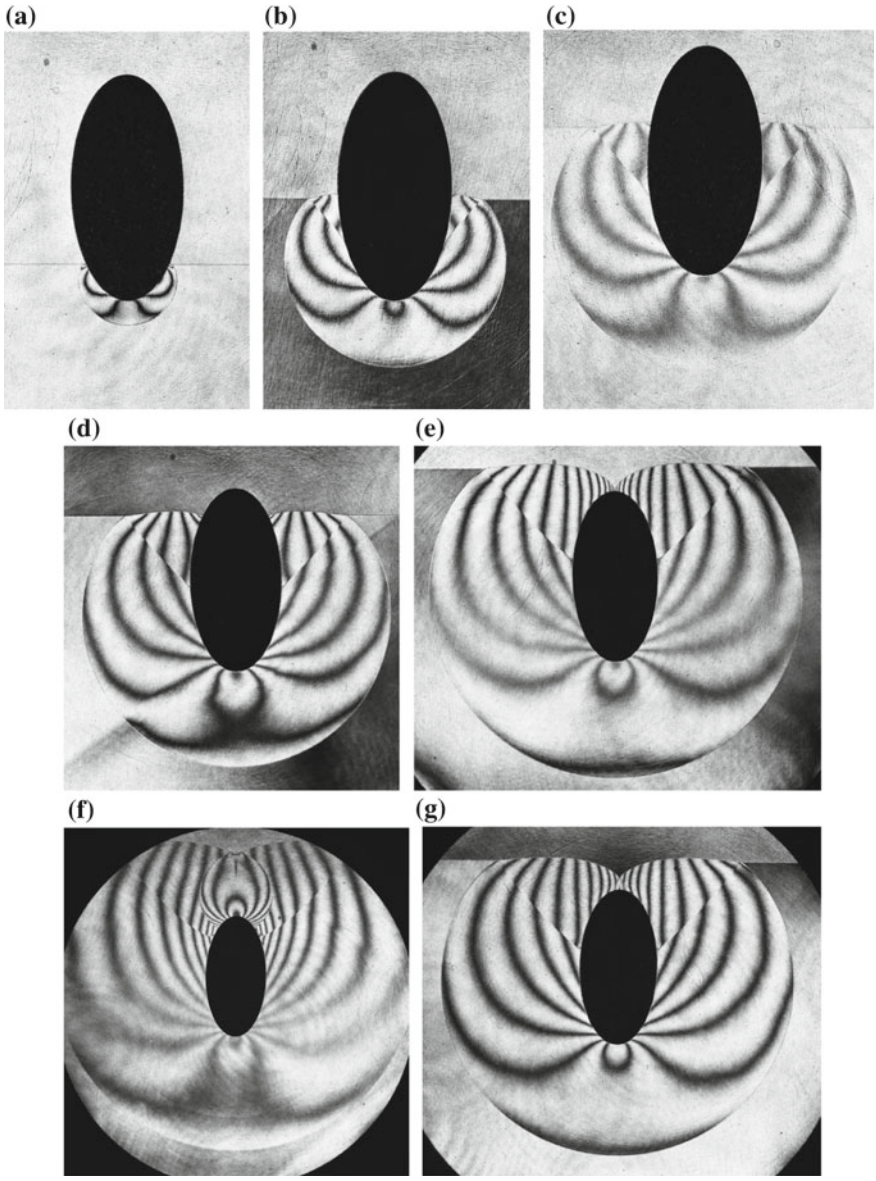

Fig. 4.31 The evolution of the shock wave interaction with a 1:2 elliptical cylinder for Ms = 1.30 in atmospheric air at 298.9 K, attack angle $\alpha = 0°$: **a** #85083017, Ms = 1.300; **b** #85083020, Ms = 1.295; **c** #85083104, Ms = 1.298; **d** #85083106, Ms = 1.302; **d** #85083106, Ms = 1.302; **e** #85083107, Ms = 1.304; **f** #85083109, Ms = 1.298; **g** #85083108, Ms = 1.295

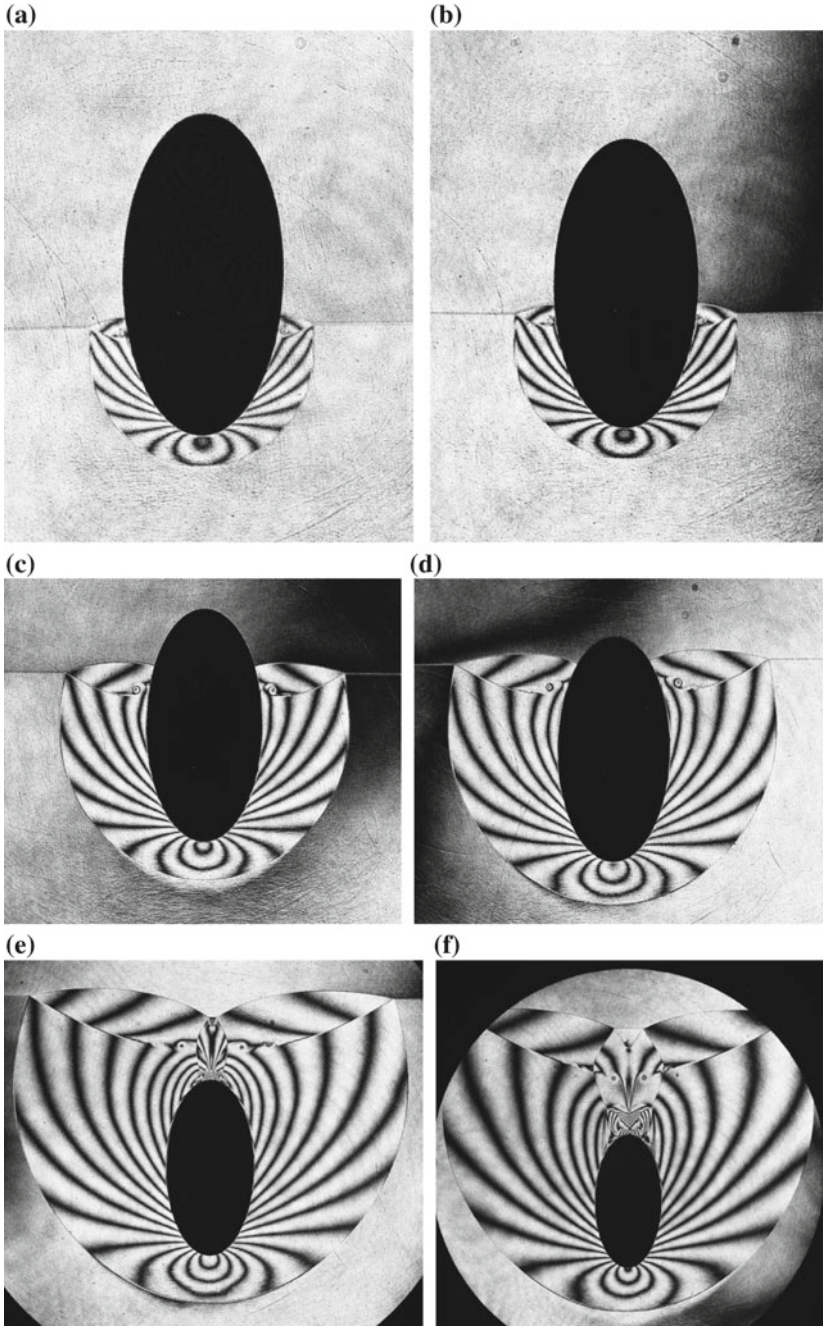

Fig. 4.32 Shock wave interaction with a 2:1 elliptical cylinder interaction for Ms = 2.60 in air at 120 hPa, 298.8 K, attack angle $\alpha = 0°$: **a** #85090215, Ms = 2.589; **b** #85090207, Ms = 2.611; **c** #85090206, Ms = 2.574; **d** #85090204, Ms = 2.589; **e** #85090216, Ms = 2.571; **f** #85090205, Ms = 2.649

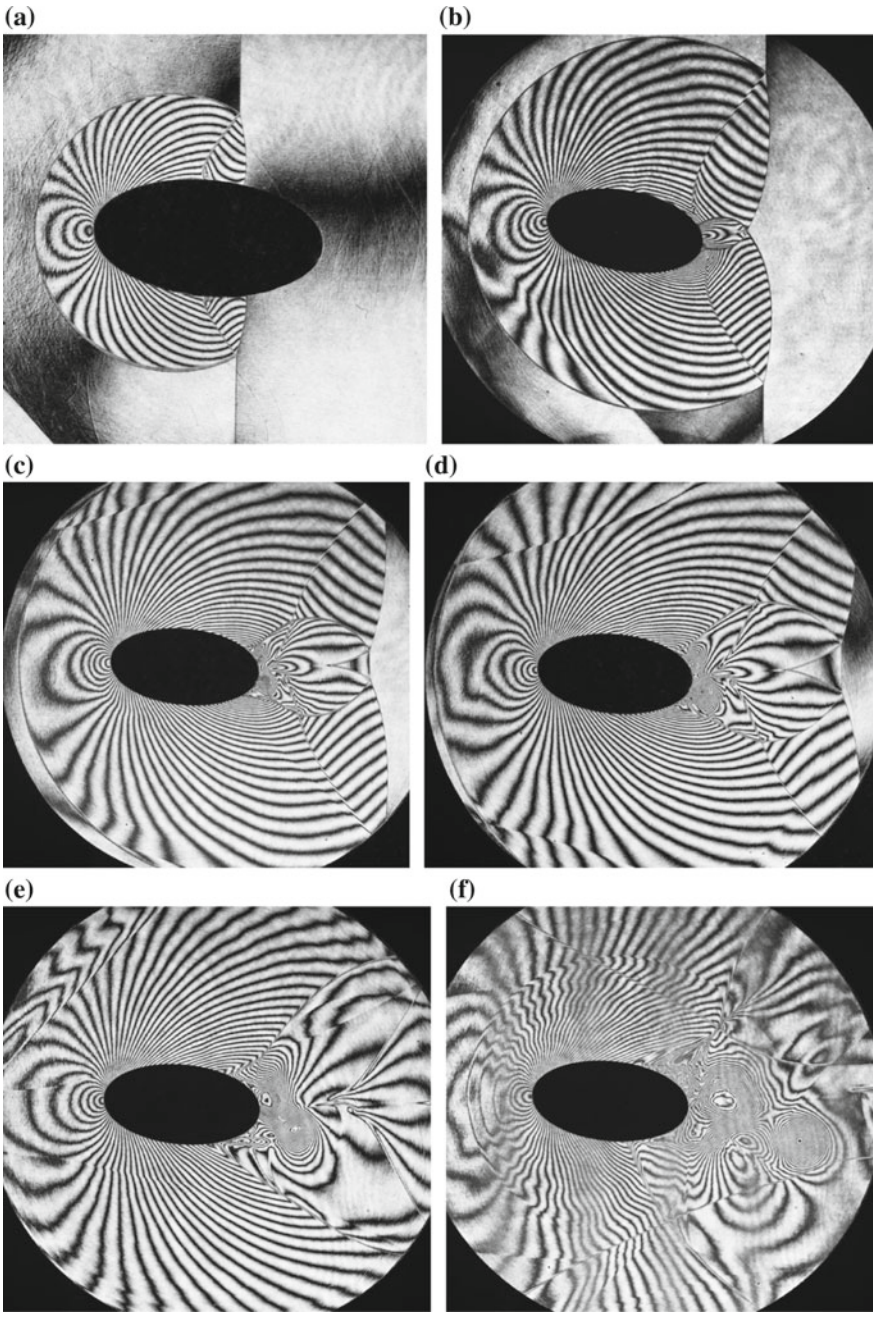

Fig. 4.33 Evolution of shock wave interaction with a 2:1 elliptical cylinder interaction for Ms = 1.70 in air at 900 hPa, 288.1 K, attack angle α =5°: **a** #87012204 1.5 ms, Ms = 1.677; **b** #87012215 150 μs Ms = 1.687; **c** #87012207 160 μs Ms = 1.686; **d** #87012202 200 μs Ms = 1.701; **e** #87012209 200 μs Ms = 1.701; **f** #87012212 350 μs Ms = 1.601; **g** #87012306 250 μs Ms = 1.682; **h** #87012213 400 μs Ms = 1.683; **i** enlargement of (**h**)

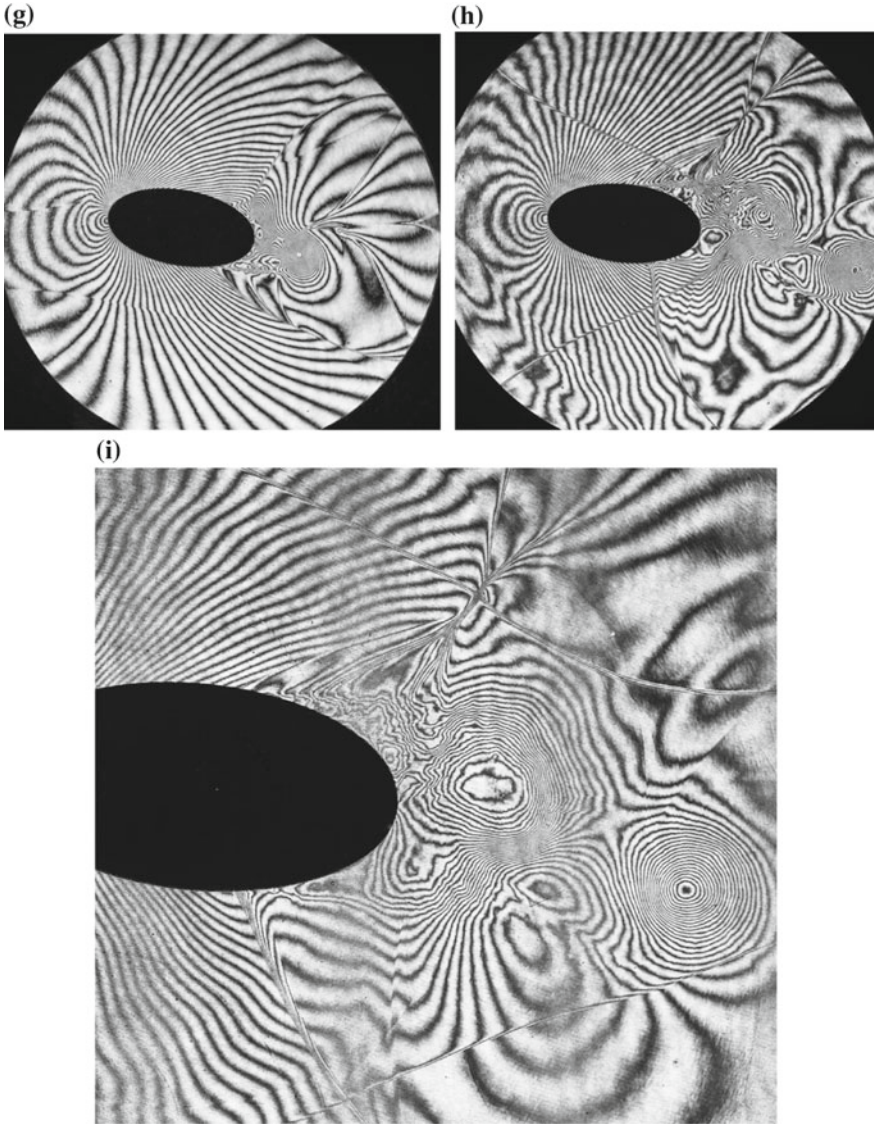

Fig. 4.33 (continued)

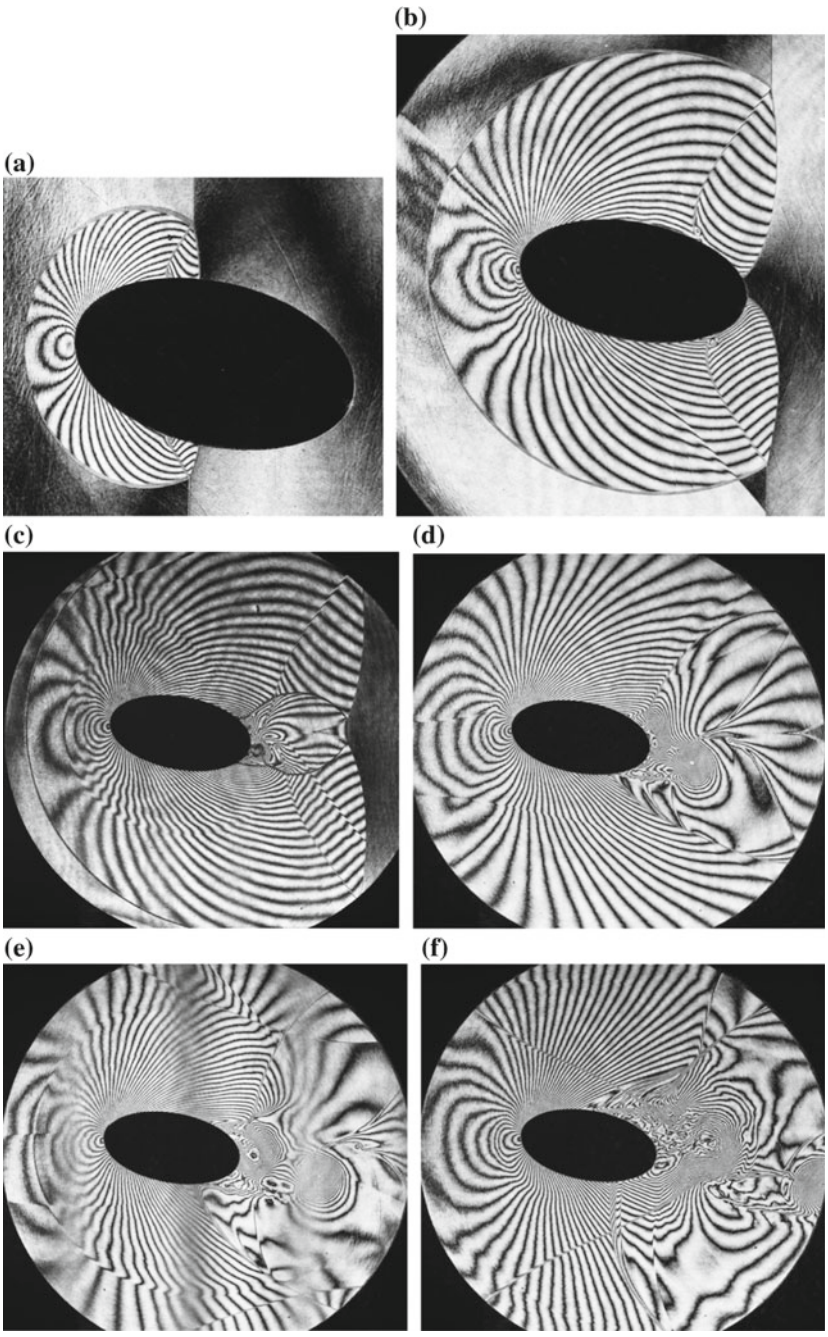

Fig. 4.34 Evolution of shock wave interaction with a2:1 elliptical cylinder interaction at Ms = 1.70 in air at 900 hPa, 288.1 K, attack angle $\alpha = 10°$: **a** #87012302, Ms = 1.702; **b** #87012305, Ms = 1.671 8701; **c** #87012301, Ms = 1.679; **d** #87012306, Ms = 1.682; **e** #87012307 300 μs Ms = 1.693; **f** #87012602 400 μs Ms = 1.691

4.4.3 4:1 Elliptic Cylinders

Figures 4.35 and 4.36 show the evolution of the shock wave interaction with a 4:1 elliptic cylinder at attack angle $\alpha = 0°$ for Ms = 1.7 and 2.6 respectively.

The interferograms have precise spatial distributions over the elliptic cylinders enough to resolve the density distributions on elliptical cylinder surface as observed, for example in Fig. 4.29 and Fig. 4.31. The time variation of density distributions over the elliptical cylinders can be experimentally determined out of the sequential interferograms. If assuming isothermal condition on the cylinder surface, the pressure p on the cylinder can be estimated out of the density distribution on the cylinder surfaces by assuming $p/\rho^{\gamma} = p_0/\rho_0^{\gamma}$ where p_0 is ambient pressure, ρ_0 is ambient density. Then integrating the pressure profile along the cylinder surface, the drag force on the cylinders can be estimated. Itoh (1986) summarized the time variation of the drag coefficient C_D over 40 mm major diameter and 30 mm, 20 mm and 10mm minor diameter elliptical cylinders for Ms = 1.30 in atmospheric air. Figure 4.37 summarizes the results. The ordinate denotes C_D and the abscissa denotes dimensionless time tUs/D where t, Us, D denote elapsed time in μs, the shock speed m/s, and the major diameter of the cylinder. Red, black, blue, and green filled circles denote the experimental results of the aspect ratio of the cylinders 1.0, 4:3, 2:1 and 4:1, respectively. Just for reference, numerical simulation based on TVD finite difference scheme solving the Navier Stokes solver (Itoh 1986). Fair agreements between the experiments and the simulation are obtained. It should be noticed that the C_D can be maximal and monotonously decreases to the steady flow value. The unsteady drag force over a shock laden sphere was experimentally measured by Tanno et al. (2004) and discussed in the Sect. 2.4.

Figure 4.37 summarized the time variation in the drag coefficients for Ms = 1.30 of a 40 mm diameter cylinder, and 4:3, 2:1, 4:1 elliptic cylinders, all having a major diameter of 40 mm. The ordinate denotes drag force normalized by initial condition, $C_{D,}$ and the abscissa denotes dimension-less time tUs/D. Black, blue, green, and red filled circles denote 4:3, 2:1, and 4:2 elliptic cylinders, respectively. Solid lines denote numerical simulation using TVD scheme (Itoh 1986). Fair agreement is observed between the simulation and experimental findings.

Figures 4.38 and 4.39 show the evolution of shock wave interaction with a 4:1 elliptic cylinder for Ms = 1.70 with attack angles of $\alpha = 10°$ and $\alpha = 45°$, respectively. In Fig. 4.38, the evolution of interaction of the reflected MS with the boundary layer is observed. At an attack angle of $\alpha = 10°$, a vortex is formed at the rear edge of the 4:1 slender shaped ellipse and it is shading with the elapsed time as shown in Fig. 4.38g–h, creating a lift force. On the contrary at attack angle $\alpha = 45°$ in Fig. 4.39, the boundary layer separation occurs at the leading edge. The flow pattern is typical to stall.

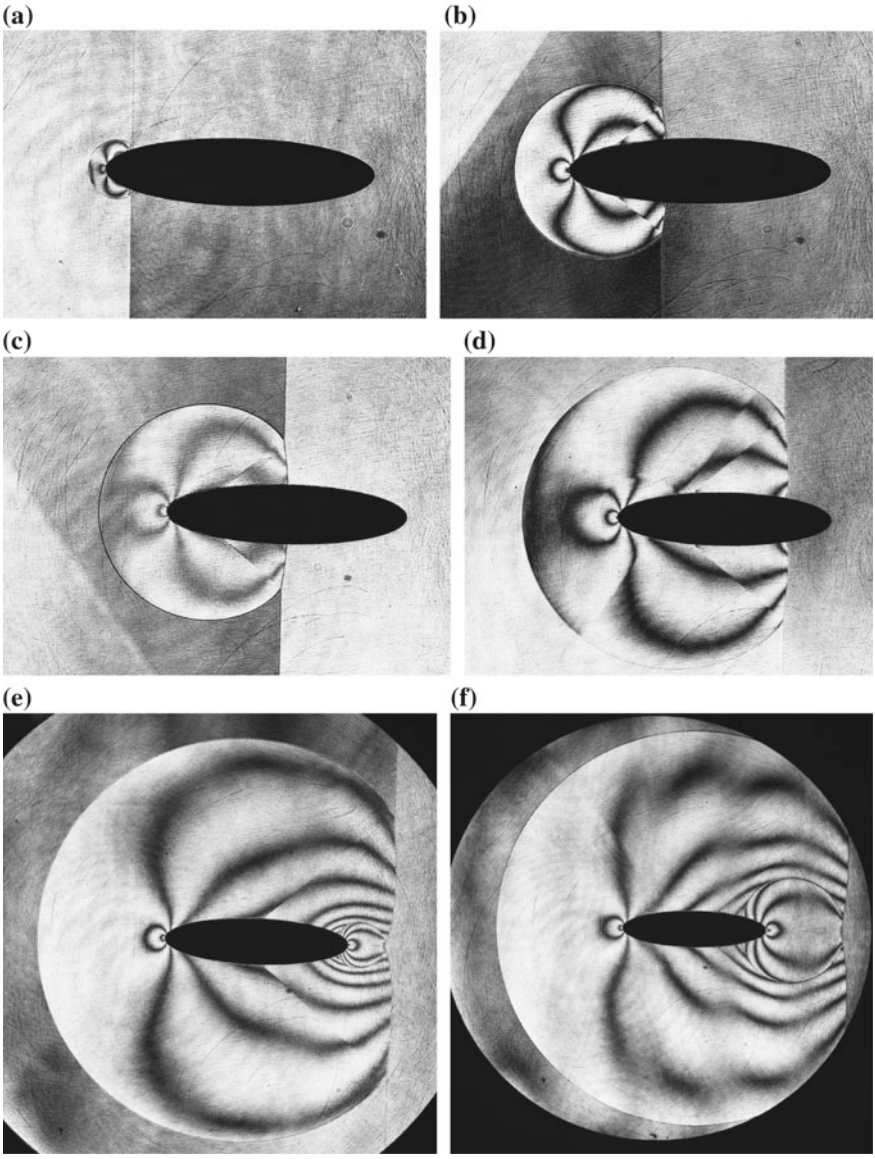

Fig. 4.35 The evolution of the shock wave interaction with a 4:1 elliptical cylinder interaction at Ms = 1.70 in air at 900 hPa, 288.1 K, attack angle $\alpha = 0°$: **a** #85090310, Ms = 1.305; **b** #85090312, Ms = 1.310; **c** #85090314, Ms = 1.300; **d** #85090315, Ms = 1.308; **e** #85090317, Ms = 1.300; **f** #85090319, Ms = 1.288

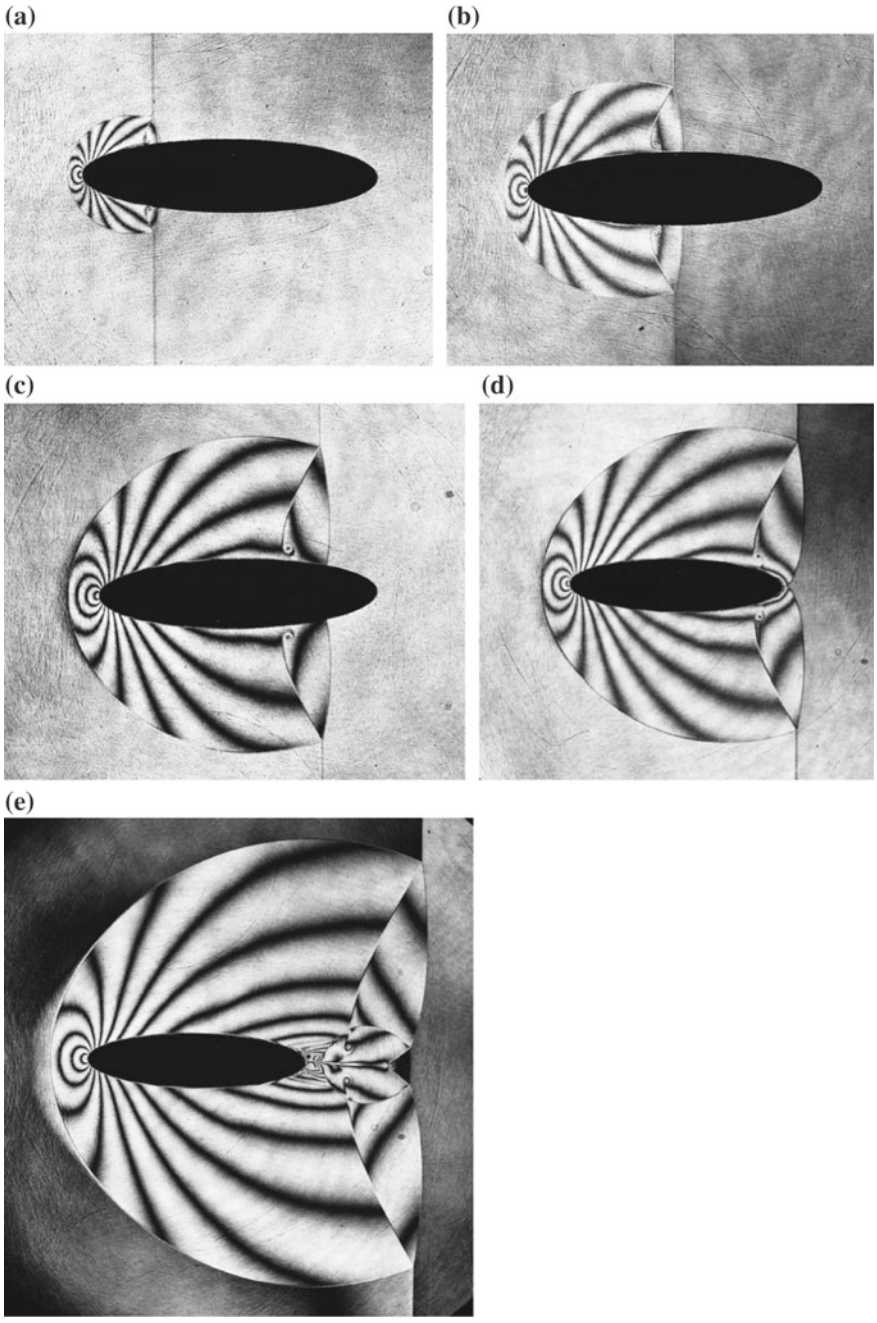

Fig. 4.36 The evolution of the shock wave interaction with a 4:1 elliptical cylinder for Ms = 2.60 in air at 120 hPa, 283.7 K, attack angle $\alpha = 0°$: **a** #85090219, Ms = 2.571; **b** #85090220, Ms = 2.597; **c** #85090218, Ms = 2.601; **d** #85090222, Ms = 2.594; **e** #85090301, Ms = 2.588; **f** enlargement of (**e**)

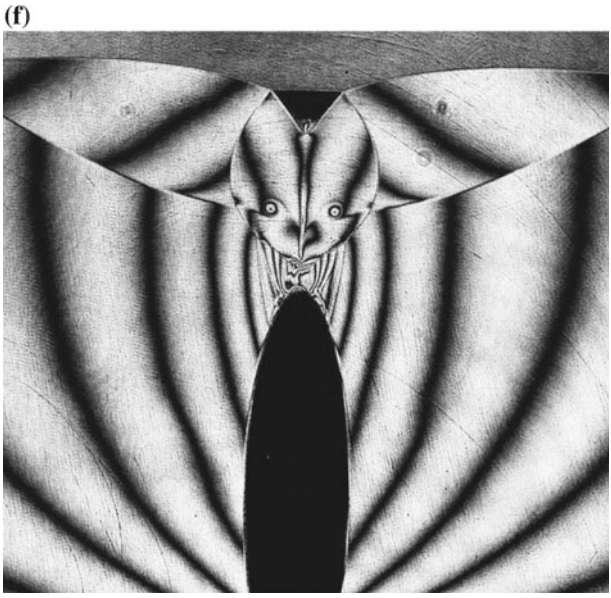

Fig. 4.36 (continued)

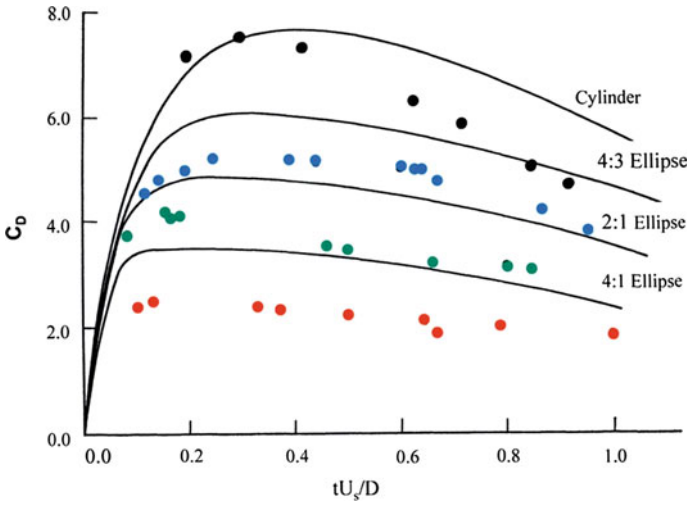

Fig. 4.37 Time variation of drag forces over a cylinder and ellipses at $\alpha = 0°$ for Ms = 1.30 in air (Itoh 1986)

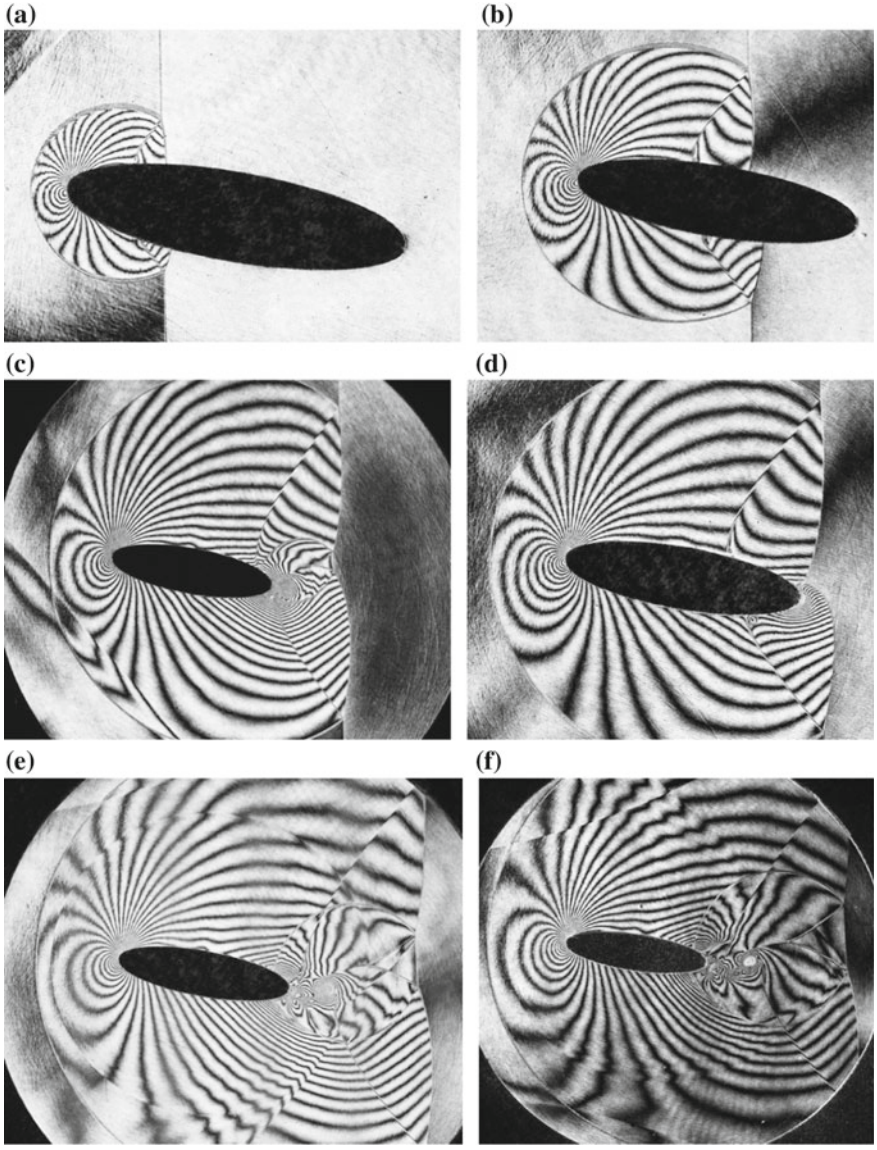

Fig. 4.38 Evolution of shock waves interaction with a 4:1 elliptical cylinder for Ms = 1.70 in air at 900 hPa, 283.7 K, attack angle $\alpha = 10°$: **a** #87012802, Ms = 1.700; **b** #87012803, Ms = 1.704; **c** #87012801, Ms = 1.721; **d** #87012805, Ms = 1.713; **e** #87012808, Ms = 1.707; **f** #87012701, Ms = 1.661; **g** #87012703, Ms = 1.680; **h** #87012704, Ms = 1.685; **i** enlargement of (**h**)

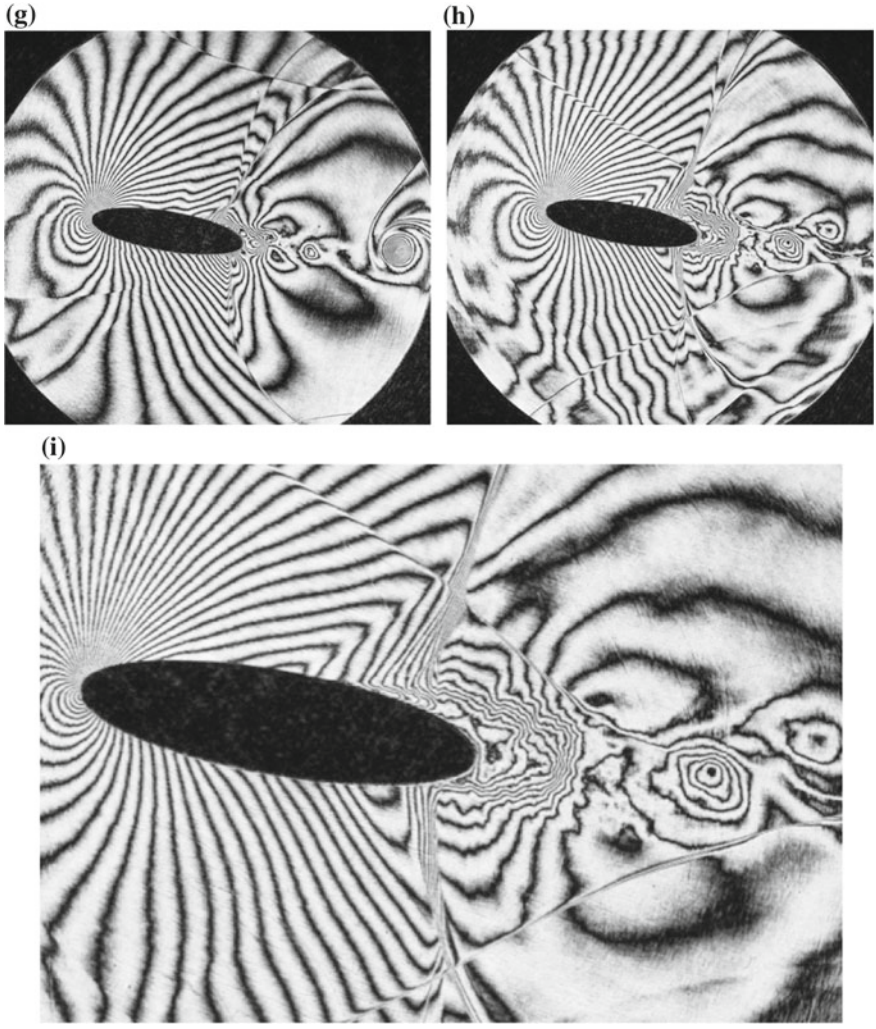

Fig. 4.38 (continued)

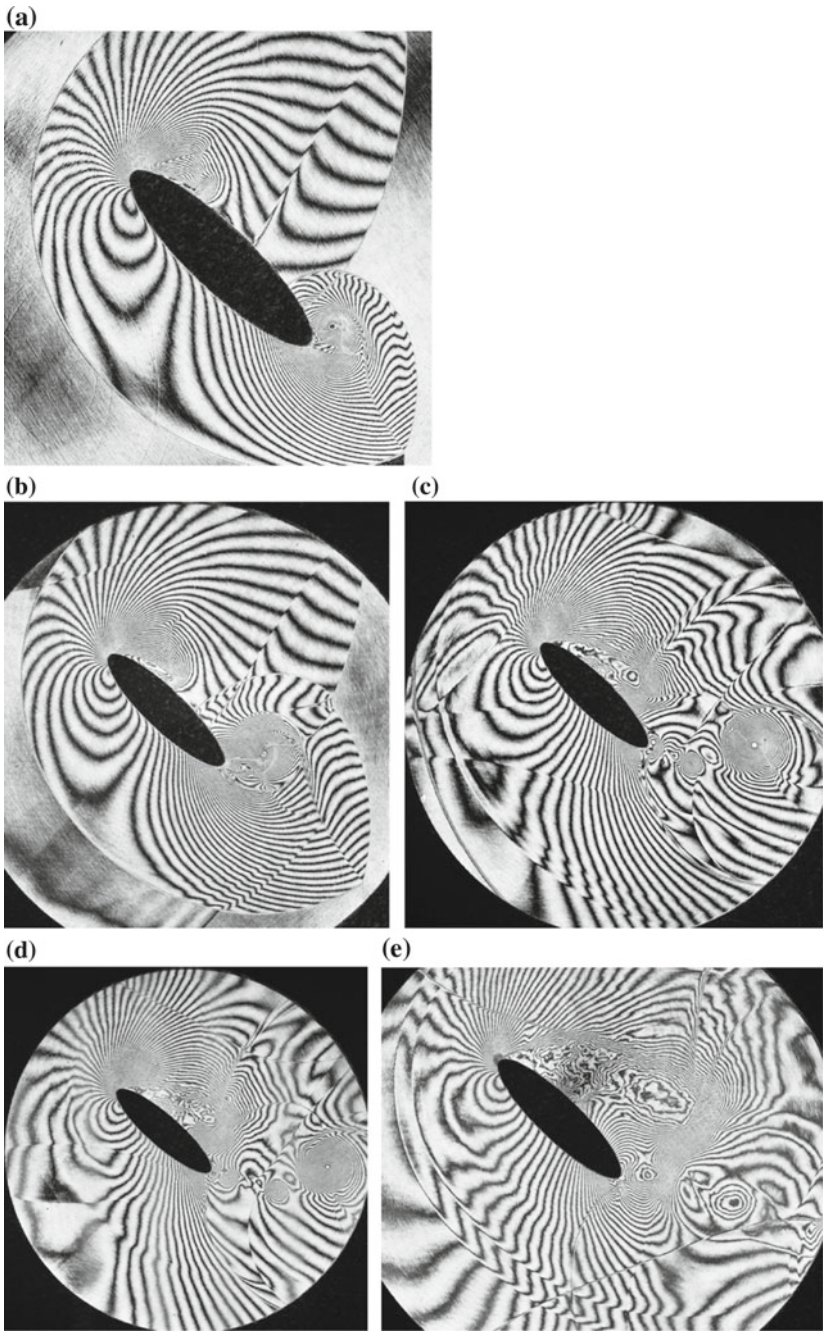

Fig. 4.39 The evolution of the shock wave interaction with a 4:1 elliptical cylinder for Ms = 1.70 in air at 900 hPa, 290.7 K, attack angle $\alpha = 45°$: **a** #87012904, Ms = 1.674; **b** #87012908, Ms = 1.690; **c** #87012910, Ms = 1.697; **d** #87012901, Ms = 1.675; **e** #87012902, Ms = 1.689

4.4.4 Rectangular Plates

4.4.4.1 Rectangular Plate with Attack Angle $\alpha = 0°$

Figure 4.40a–j show the evolution of shock wave interaction for Ms = 1.40 in atmospheric air with a 10 mm thick and 40 mm wide rectangular plate of aspect ratio of 4:1 installed in the 60 mm $\times$150 mm conventional shock tube at attack angle $\alpha = 0°$. The resulting Reynolds number referred to the test condition is about $Re = 5.0 \times 10^5$. The transmitting shock wave is diffracted at the rear corners and the reflected expansion wave propagates to the reverse direction. Figure 4.41a–i show

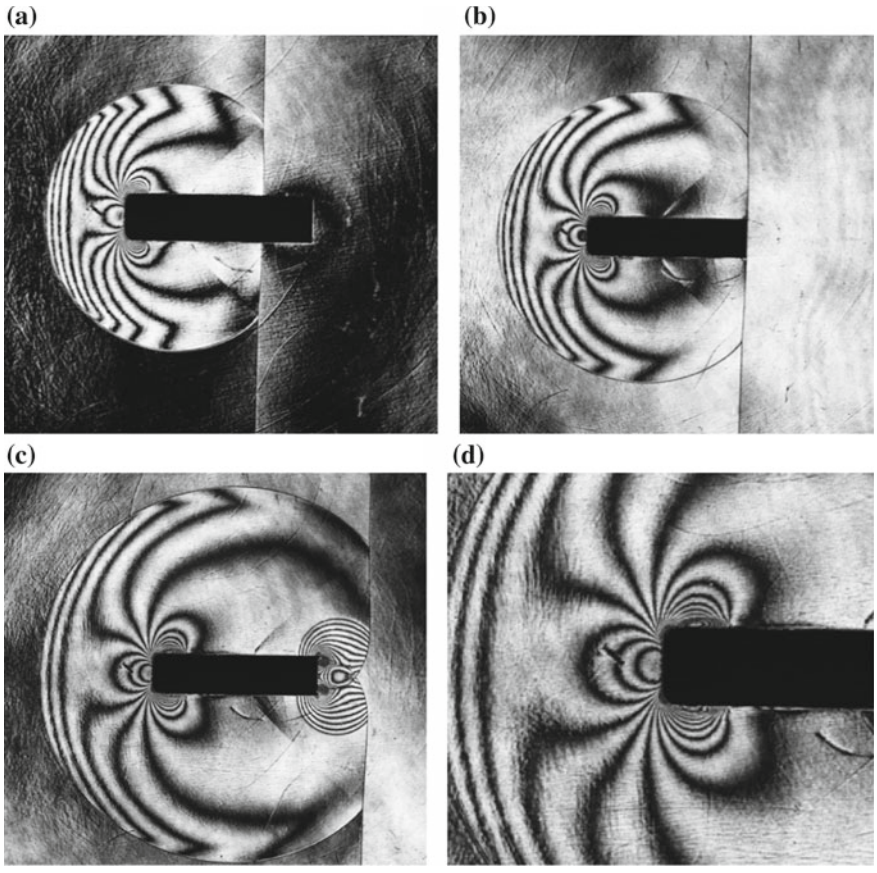

Fig. 4.40 The evolution of the shock wave interaction with a 4:1 rectangular plate for Ms = 1.40 in atmospheric air at 290.0 K and attack angle $\alpha = 0°$: **a** #88021524, Ms = 1.387; **b** #88021525, Ms = 1.392; **c** #88021522, Ms = 1.400; **d** enlargement of (**c**); **e** #88021516, Ms = 1.398; **f** 88021517, Ms = 1.401; **g** #88021518, Ms = 1.398; **h** #88021519, Ms = 1.395; **i** #88021520, Ms = 1.403; **j** 88021521, Ms = 1.405

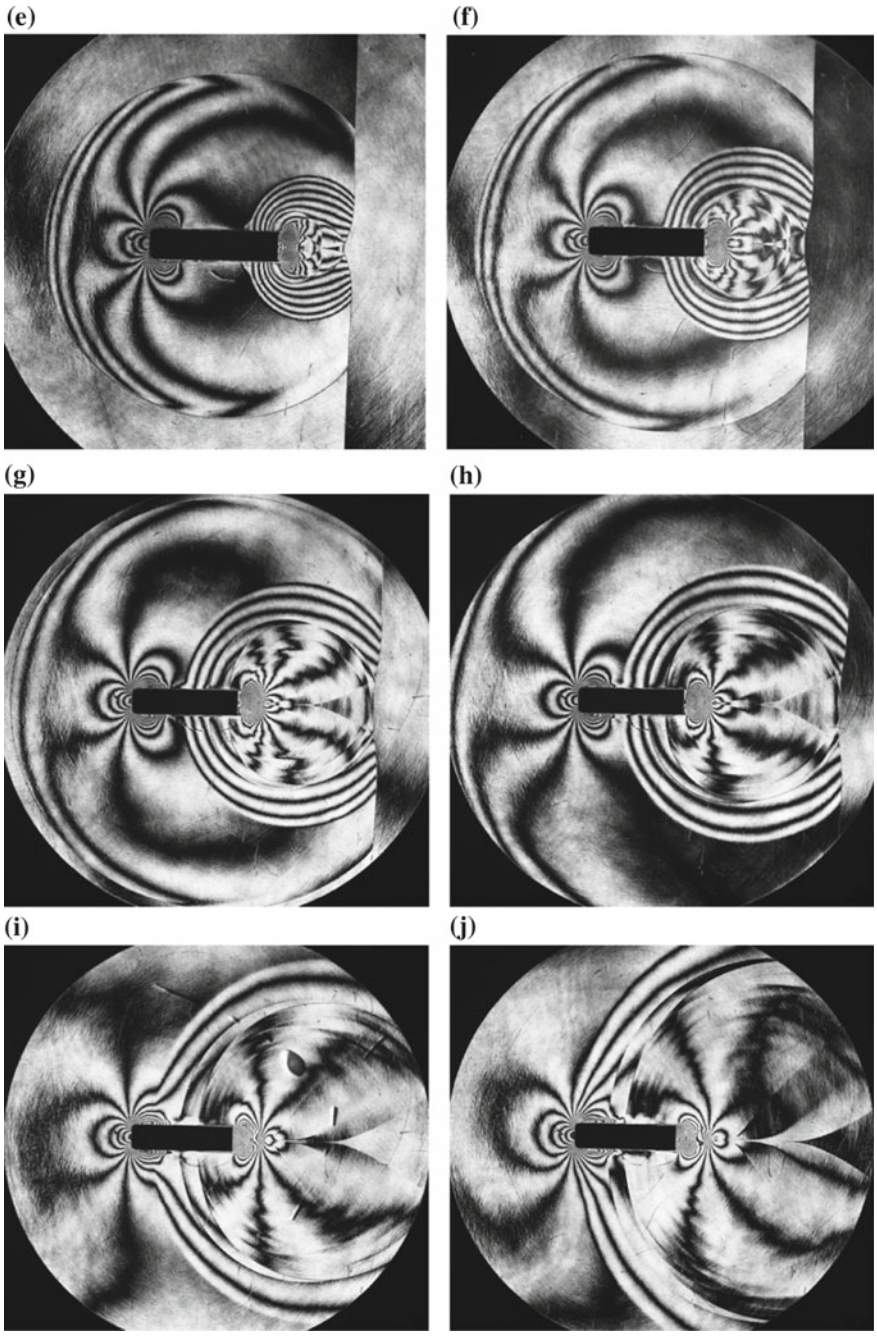

Fig. 4.40 (continued)

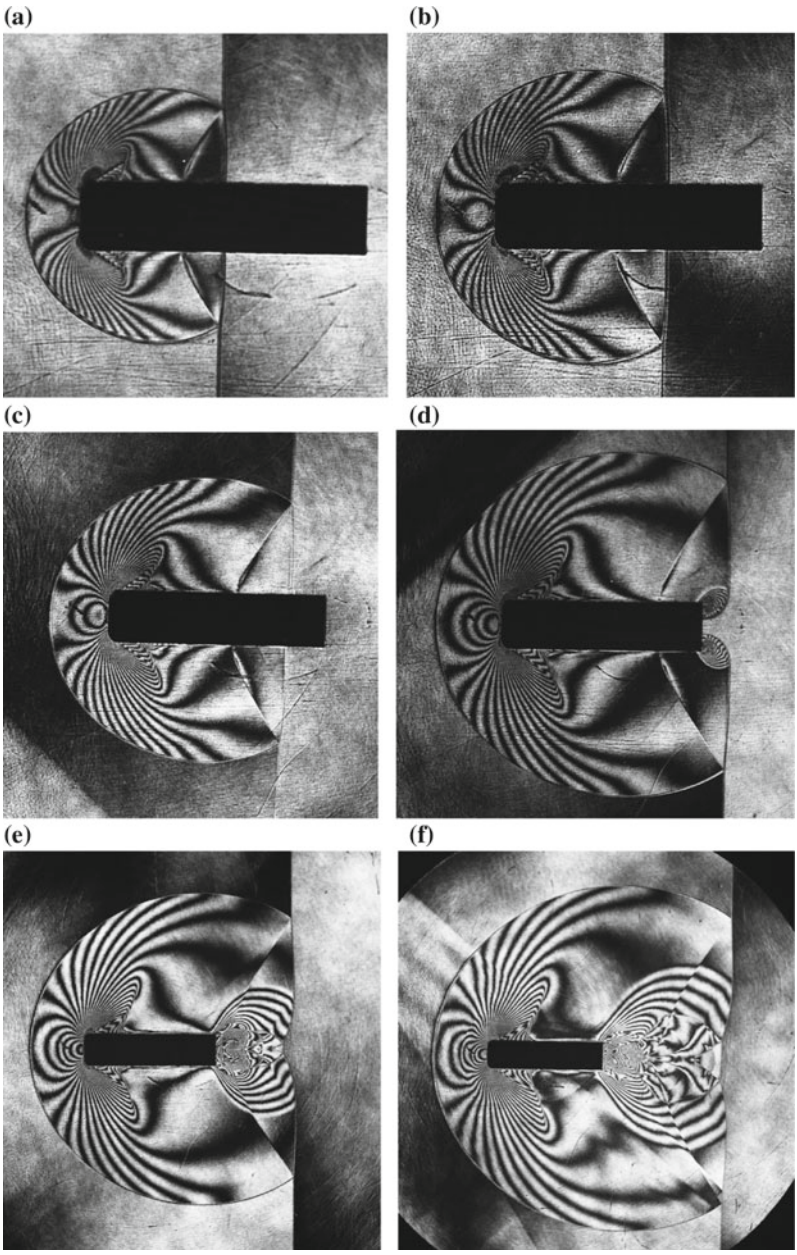

Fig. 4.41 The evolution of the shock wave interaction with a 4:1 rectangular plate for Ms = 2.20 in air at 300 hPa, 291.2.0 K, attack angle $\alpha = 0°$: **a** #88021503, Ms = 2.168; **b** #88021504, Ms = 2.150; **c** #88021505, Ms = 2.141; **d** #88021506, Ms = 2.188; **e** #88021508, Ms = 2.210; **f** #88021510, Ms = 2.157; **g** #88021512, Ms = 2.118; **h** #88021513, Ms = 2.185; **i** enlargement of (**h**)

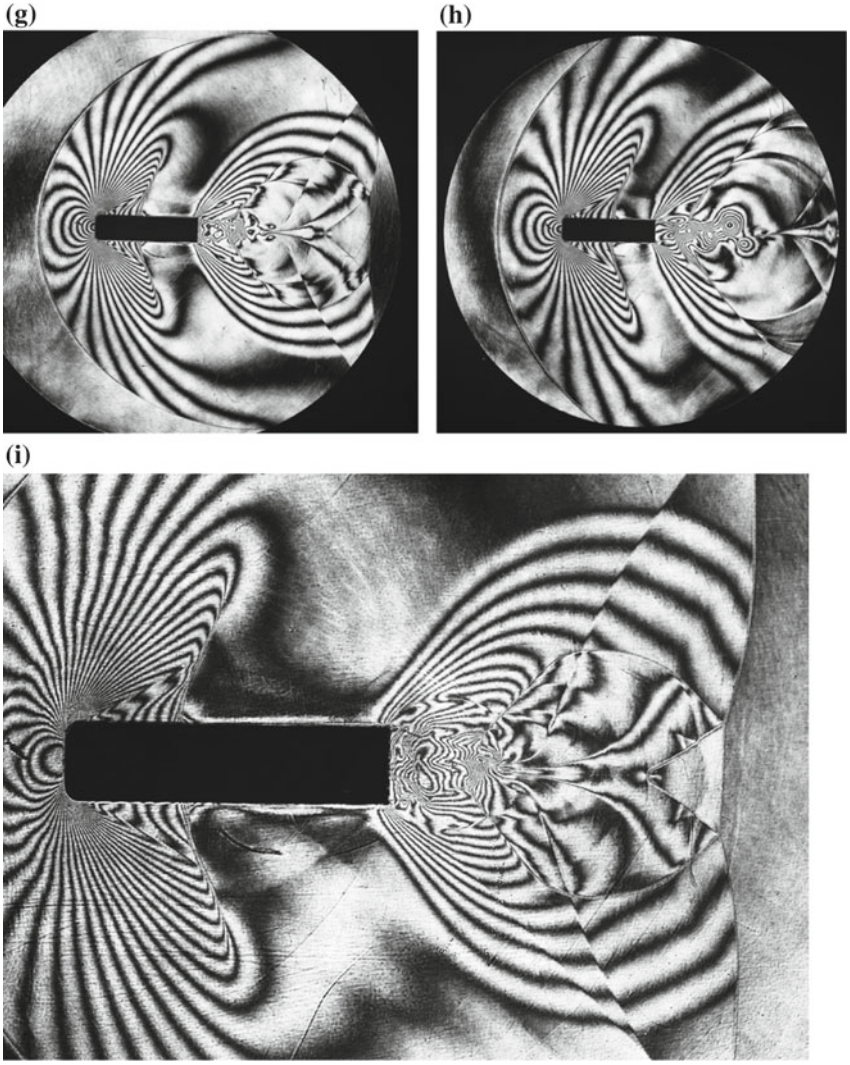

Fig. 4.41 (continued)

the evolution of the shock wave interaction of the rectangular plate of aspect ratio 4:1 for Ms =2.20. Impinging on the rectangular plate, the IS is diffracted at the frontal corner forming separation bubbles. The transmitting shock wave is diffracted again at the rear corners.

4.4.4.2 Attack Angle $\alpha = 5°$

Figure 4.42a–f show reflected shock wave interactions for Ms = 1.70 in atmospheric air with the 4:1 rectangular plate at attack angle $\alpha = 5°$. Upon the shock wave impingement, the IS was diffracted at the upper corner of the frontal side forming a separation bubble which developed with elapsed time. The transmitting shock wave was diffracted at the corner of the rear side of the rectangular plate.

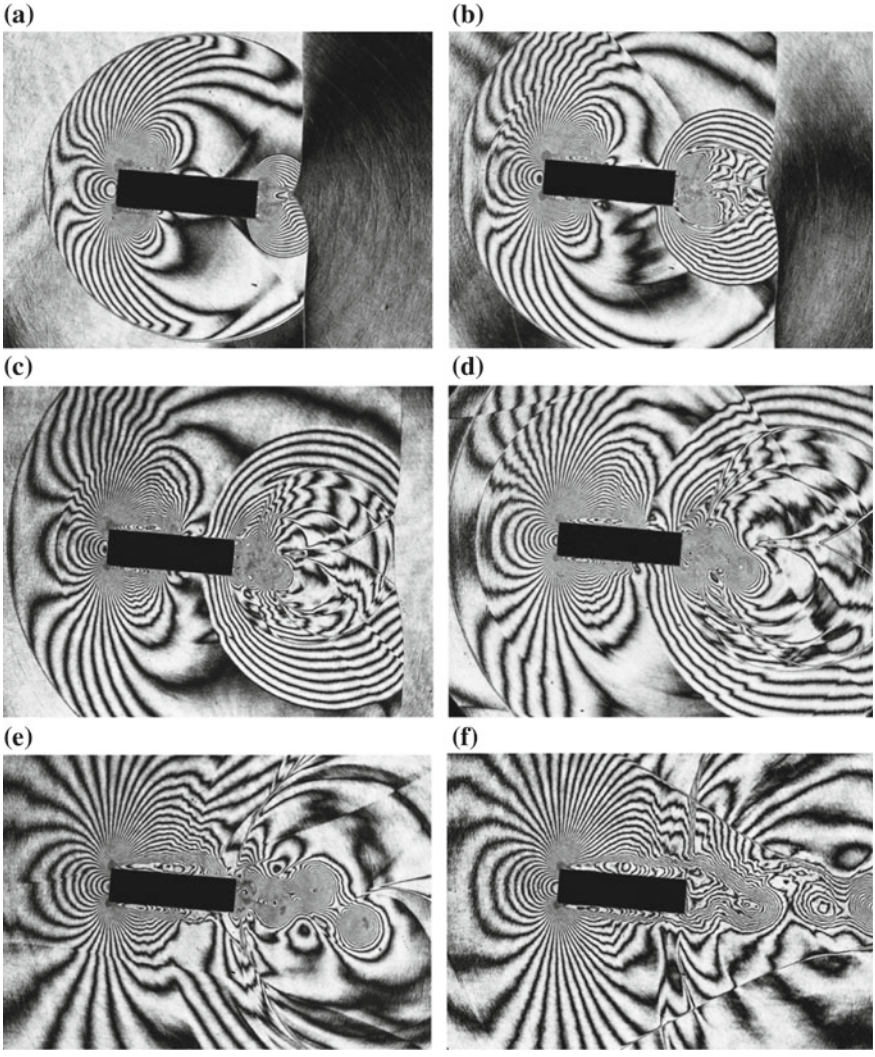

Fig. 4.42 The evolution of the shock wave interaction with a 4:1 rectangular plate for Ms = 1.70 in atmospheric air at 290.0 K, attack angle $\alpha = 5°$: **a** #87012006, Ms = 1.714; **b** #87012002, Ms = 1.700; **c** #87012010, Ms = 1.684; **d** #87012001, Ms = 1.696; **e** #87012007, Ms = 1.722; **f** #87012009. Ms = 1.685

4.4.4.3 Attack Angle $\alpha = 10°$

Figure 4.43a–d show reflected shock wave interaction for Ms = 1.70 in atmospheric air with 4:1 rectangular plate at attack angle $\alpha = 10°$. Upon the shock wave impingement, the IS was diffracted more significantly at the upper corner of the frontal side forming a separation bubble which developed with elapsing time. The train of vortices was intermittently released from the corners of the rear side.

4.4.4.4 Attack Angle $\alpha = 45°$

Figure 4.44a–f show reflected shock wave interaction for Ms = 1.70 in atmospheric air with 4:1 rectangular plate at $\alpha = 45°$. In Fig. 4.44a the IS was reflected from the lower corner and was diffracted at the upper corner of the frontal side.

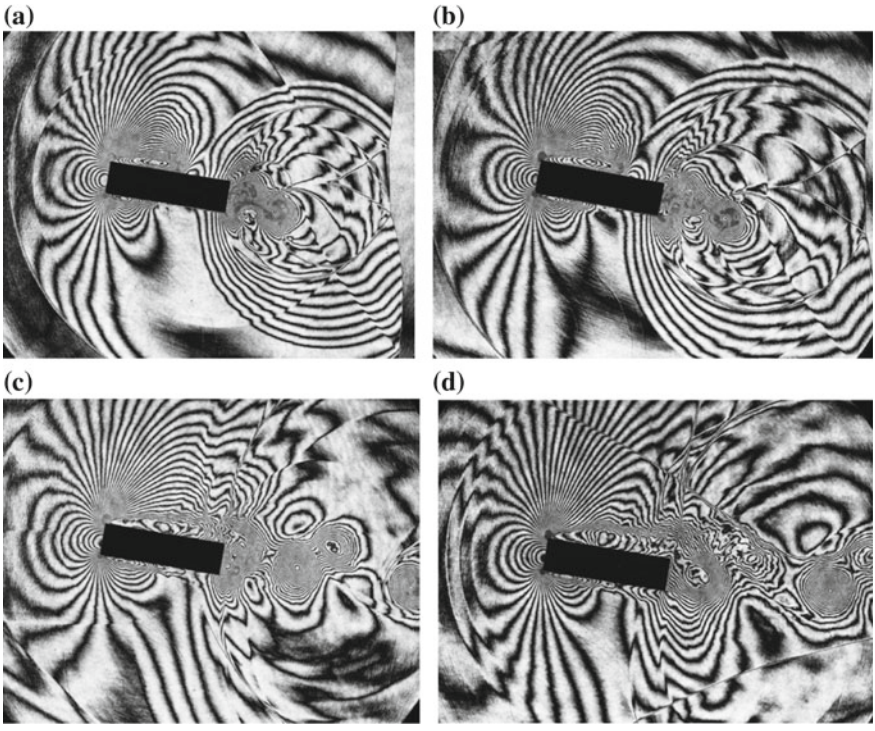

Fig. 4.43 Evolution of shock wave interaction with a 4:1 rectangular plate for Ms = 1.70 in atmospheric air at 290.0 K, attack angle $\alpha = 10°$: **a** #87012103, Ms = 1.689; **b** #87012011, Ms = 1.663; **c** #87012107, Ms = 1.696; **d** #87012013, Ms = 1.658

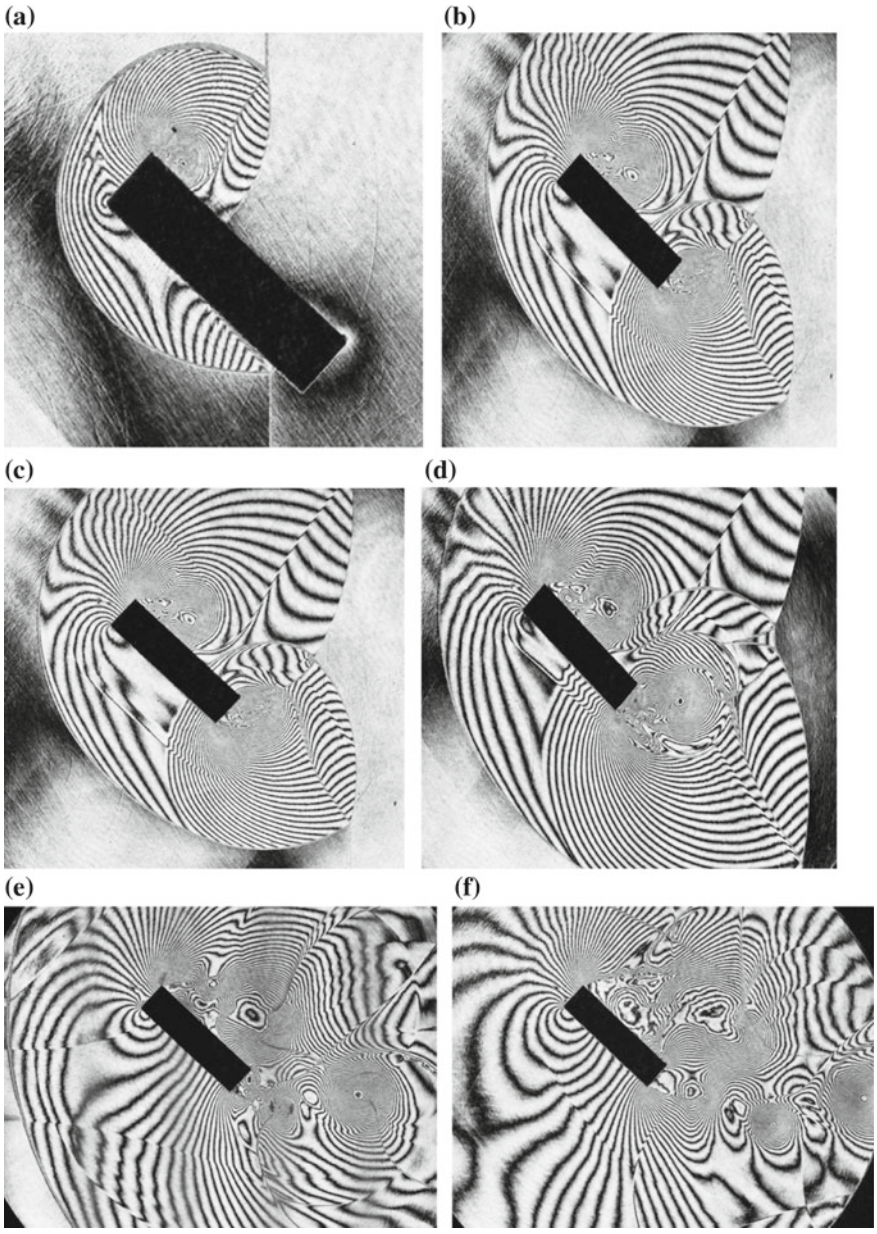

Fig. 4.44 The evolution of the shock wave interaction with a 4:1 rectangular plate for Ms = 1.70 in air at 900 hPa, 284.6 K, attack angle $\alpha = 45°$: **a** #87013009, Ms = 1.673; **b** #87013008, Ms = 1.684; **c** #87013003, Ms = 1.686; **d** #87013006, Ms = 1.706; **e** #87013005, Ms = 1.687; **f** #87013010, Ms = 1.679

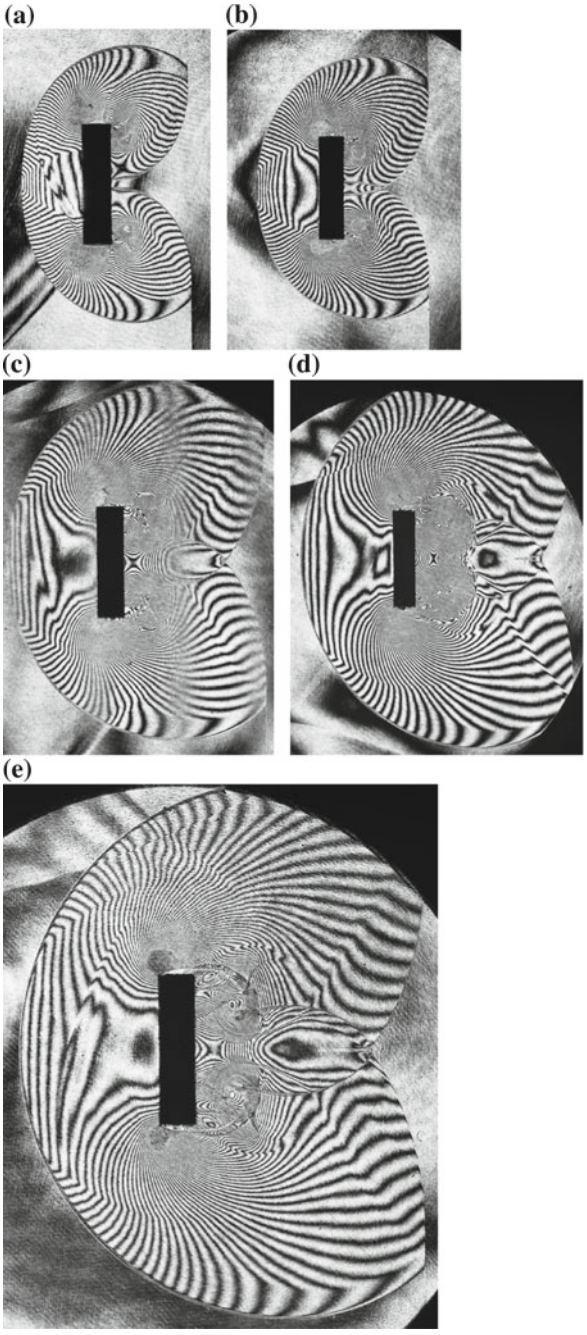

Fig. 4.45 Interaction with a 4:1 rectangular plate for Ms = 1.70 in air at 900 hPa, 284.6 K and attack angle $\alpha = 90°$: **a** #87020601, Ms = 1.719; **b** #87020902, Ms = 1.718; **c** #87020603, Ms = 1.719; **d** #87020702, Ms = 1.703; **e** #87020901, Ms = 1.718

4.4.4.5 Attack Angle $\alpha = 90°$, Head-on Collision

Figure 4.45a–e show head reflection of shock wave for Ms = 1.70 from the 4:1 rectangular plate at $\alpha = 90°$.

4.4.5 NACA 0012 Airfoil

An NACA0012 airfoil having a 60 mm chord length is sandwiched between two circular acrylic plates and installed in the test section of the 60 mm × 150 mm conventional shock tube. However, shock tubes are not necessarily useful tools for generating transonic flows ranging the flow Mach number from 0.95 to 1.05. However, moderately strong transonic flows are relatively easily reproduced in shock tubes. As the blockage ratio of the airfoil was about 0.2 and wavelets were readily suppressed, the resulting transonic flow was established after 1.3 ms transient period of time and was maintained for about 1.5 ms.

For a Ms = 1.74 shock wave in air at 700 hPa, 293 K, the local flow Mach number M is 0.8 and the Reynolds number Re is 5×10^5. To adjust an attack angle, the entire observation windows were rotated to a specified attack angle (Itoh 1986). Figure 4.46 show the sequence of establishing the transonic flow. The IS of Ms = 1.80 impinged on the airfoil as seen in Fig. 4.46a–c. The reflected Mach stems propagated reversely and the reflected waves from the upper and lower walls passing along the airfoil surface were suppressed with elapsing time as seen in Fig. 4.46d.

Figure 4.47 show an NACA0012 airfoil placed in the transonic flow of M = 0.8 and Re = 5×10^5 while changing its attack angle from 0° to 7.0°.

Figure 4.48c, d show a finite fringe double exposure interferogram and an infinite fringe double exposure interferogram, respectively. The finite fringe interferogram and the infinite fringe interferogram have their inherited merits and demerits when analyzing their fringes. Therefore, it would be very appropriate for image analysis, if the two types of interferograms can be combined in one interferogram. Figure 4.48a is a triple exposure interferogram. The first exposure was conducted under no flow condition and the second exposure was conducted with a *RB* the collimating lens as shown in Fig. 1.2 was rotated and shifted appropriately. Then the third exposure was conducted synchronizing the motion of the incident shock wave. Eventually the triple exposure interferogram was obtained as shown in Fig. 4.48a.

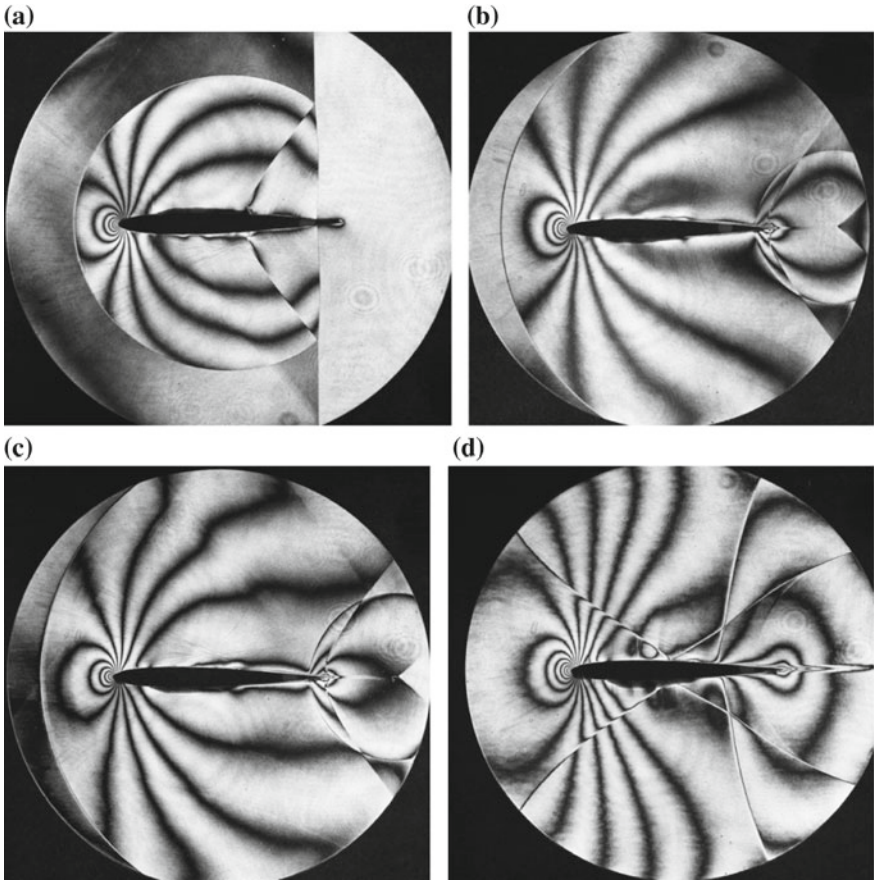

Fig. 4.46 Formation of transonic flows over an NACA0012 airfoil for Ms = 1.80, M = 0.85 in air at 500 hPa, 287.5 K: **a** #83020916 340 μs Ms = 1.798; **b** #83020912, 360 μs Ms = 1.799; **c** #83020913, 370 μs Ms = 1.798; **d** #83020920, 800 μs Ms = 1.804

Figure 4.49 show supersonic flows over an NACA 0012 airfoil at different attack angles ranging from $\alpha = 0.5°$ to 6.5° for Ms = 2.38 and local flow Mach number M = 1.03 in air. Comparing airfoils in subsonic flow to that observed in supersonic flows, it is relatively easy to analyze. Measuring fringe distributions recorded in interferograms, the density contours over the airfoil are readily deduced. Hence assuming that the isothermal wall condition prevails, the density contours are readily converted to an appropriate pressure distribution along the airfoil surface.

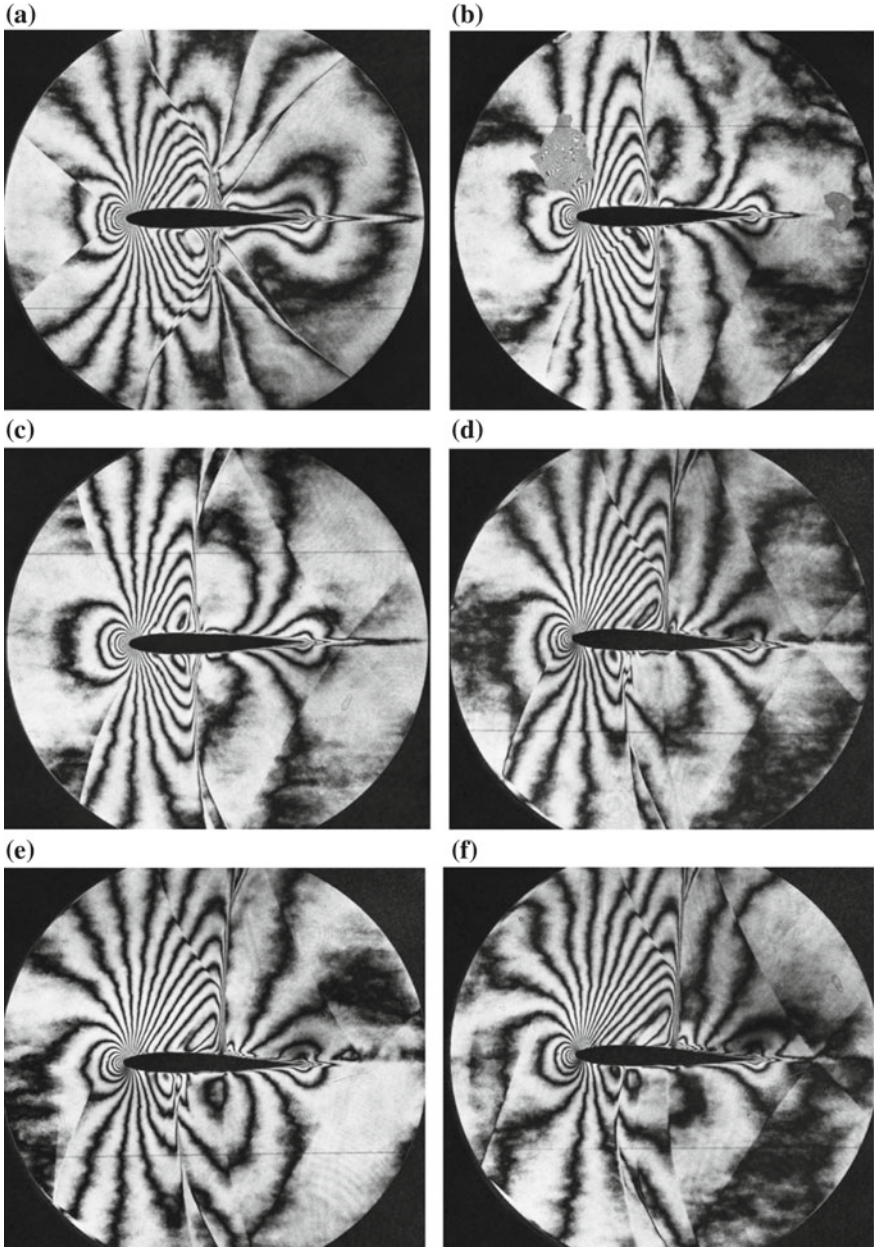

Fig. 4.47 Shock wave interaction with an NACA 0012 airfoil for Ms = 1.74, local transonic flow M = 0.80, Re $\sim 5 \times 10^5$ at 700 hPa, 293 K: **a** #83040603, 1.3 ms time delay from trigger point and attack angle $\alpha = 0.0°$; **b** #83040610, $\alpha = 0.5°$; **c** #83040607, $\alpha = 1.0°$; **d** #83040703, $\alpha = 1.25°$; **e** #83040705, $\alpha = 1.5°$; **f** #83040708, $\alpha = 1.75°$; **g** #83040802, $\alpha = 2.0°$; **h** #83040805, $\alpha = 2.5°$; **i** #83040808, $\alpha = 3.0°$; **j** #83040815, $\alpha = 3.5°$; **k** #83040813, $\alpha = 4.0°$; **l** #83040815, $\alpha = 4.5°$; **m** #83040817, $\alpha = 5.0°$; **n** #83040809, $\alpha = 5.5°$; **o** #83041101, $\alpha = 6.5°$; **p** #83040818, $\alpha = 6.9°$; **q** #83040707, $\alpha = 7.0°$; **r** enlargement of (**q**)

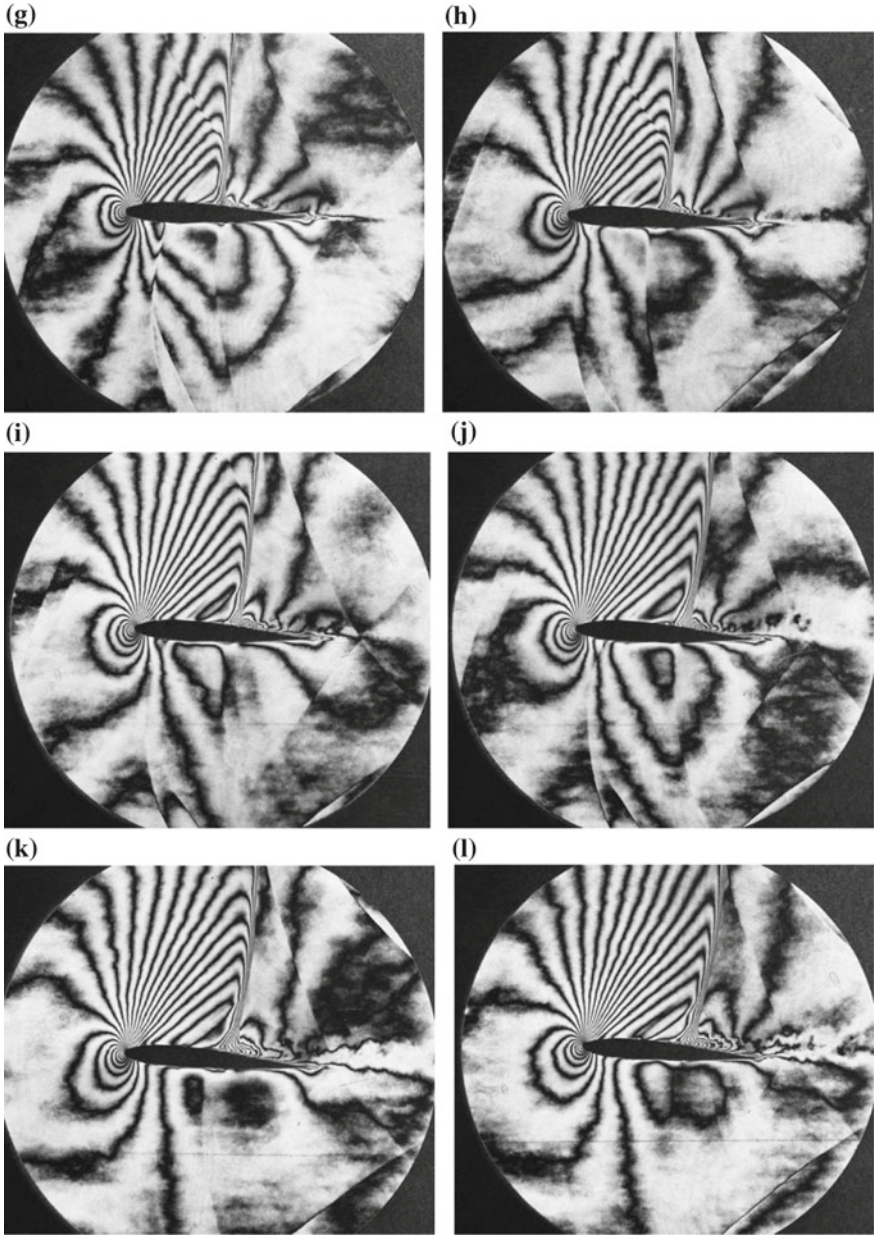

Fig. 4.47 (continued)

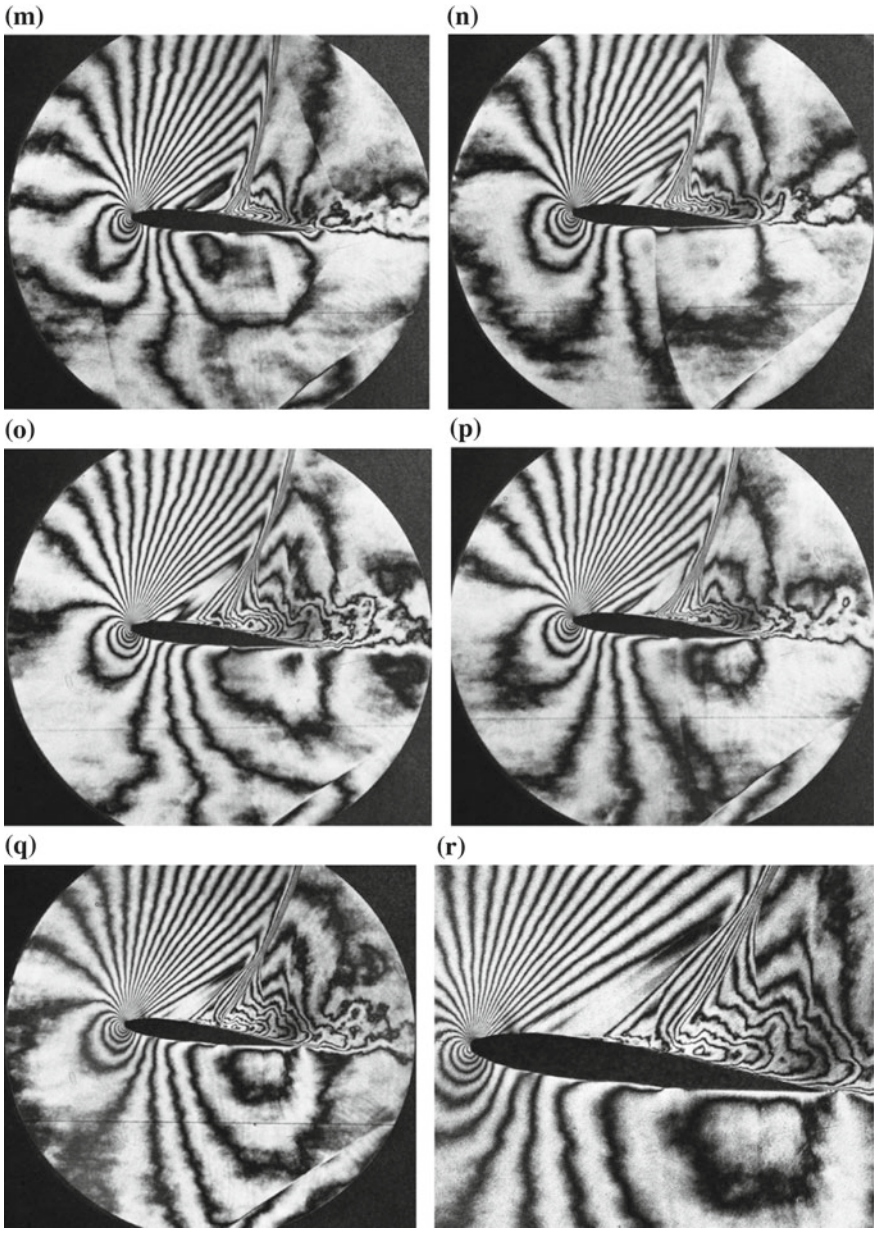

Fig. 4.47 (continued)

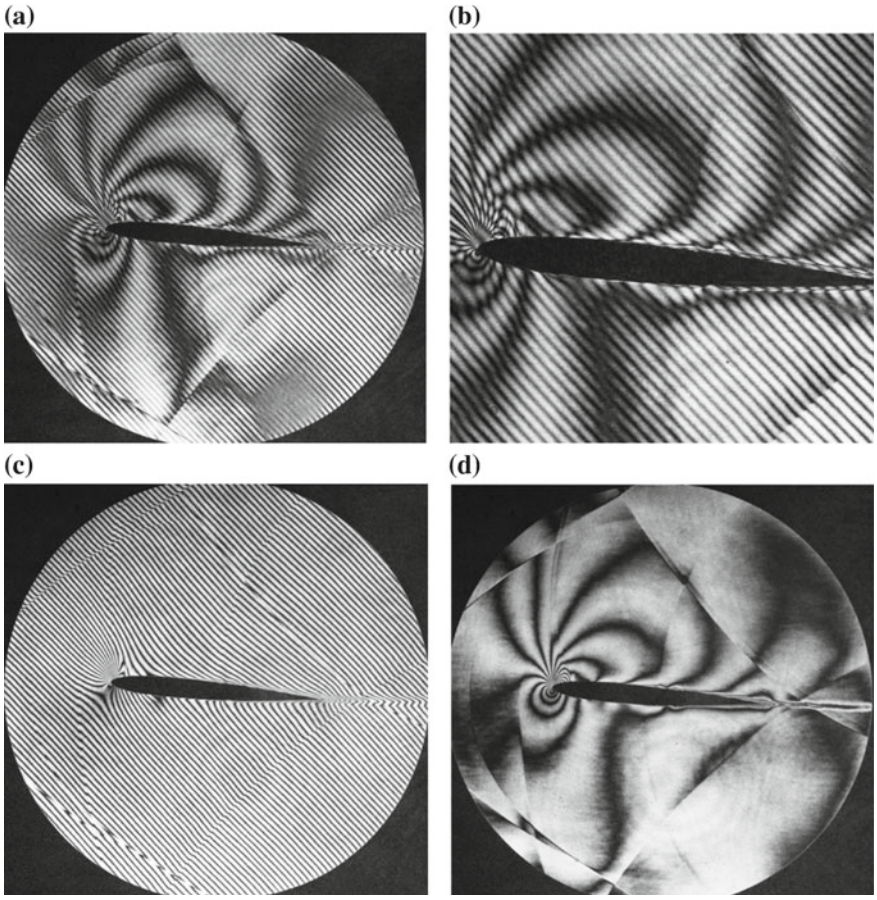

Fig. 4.48 Finite and infinite fringe double exposure interferograms and triple exposure interferogram: **a** triple exposure interferogram #83021710, Ms = 1.483; **b** enlargement of (**a**); **c** finite fringe #83021711, Ms = 1.483; **d** infinite fringe #83021712, Ms = 1.484

Therefore, the pressure coefficient of the airfoil is experimentally determined; that is, the lift coefficient and drag coefficients are determined. In Fig. 4.49, the shock stand-off distance from the airfoil was unvaried during the experiments. The black circle was the plug filling the hole of the pressure transducer. The surface of the plug was so smooth that it never disturbed the flows.

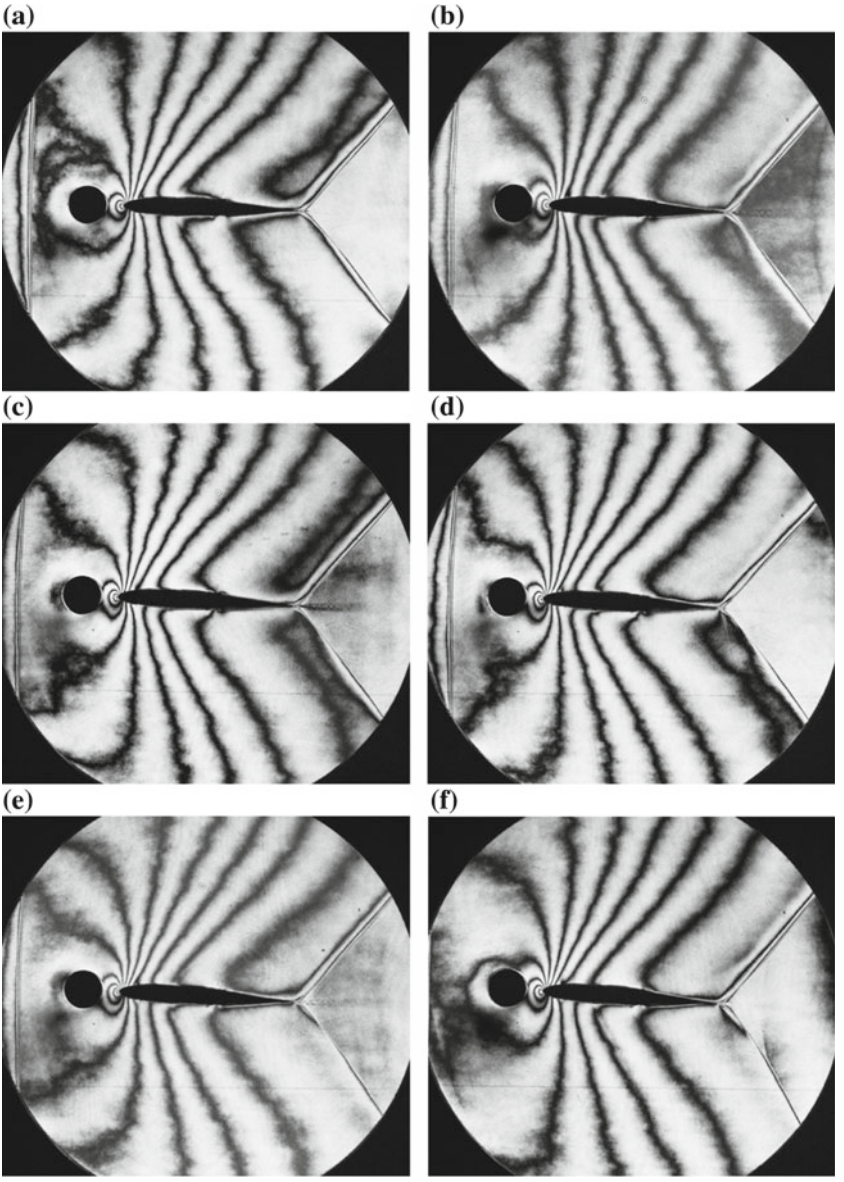

Fig. 4.49 Transonic flow of M = 1.15, Re = 6×10^4 over an NACA 0012 airfoil at variable attack angles α for Ms = 2.38 at 1.5 ms time delay from trigger point in air at 150 hPa, 293: **a** #83111512, Ms = 2.382, $\alpha = 0.5°$; **b** #83111511, Ms = 2.375, $\alpha = 1.0°$; **c** #83111509, Ms = 2.375, $\alpha = 1.5°$; **d** #83111508, Ms = 2.367, $\alpha = 2.0°$; **e** #83111507, Ms = 2.359, $\alpha = 2.5°$; **f** #83111506, Ms = 2.355, $\alpha = 3.0°$; **g** #83111505, Ms = 2.378, $\alpha = 3.5°$; **h** #83111415, Ms = 2.384, $\alpha = 4°$; **i** #83111503, Ms = 2.409, $\alpha = 4.5°$; **j** #83111418, Ms = 2.368, $\alpha = 5°$; **k** # 83111419, Ms = 2.346, $\alpha = 5.5°$; **l** # 83111501, Ms = 2.333, $\alpha = 6.0°$; **m** #83111502, Ms = 2.348, $\alpha = 6.5°$

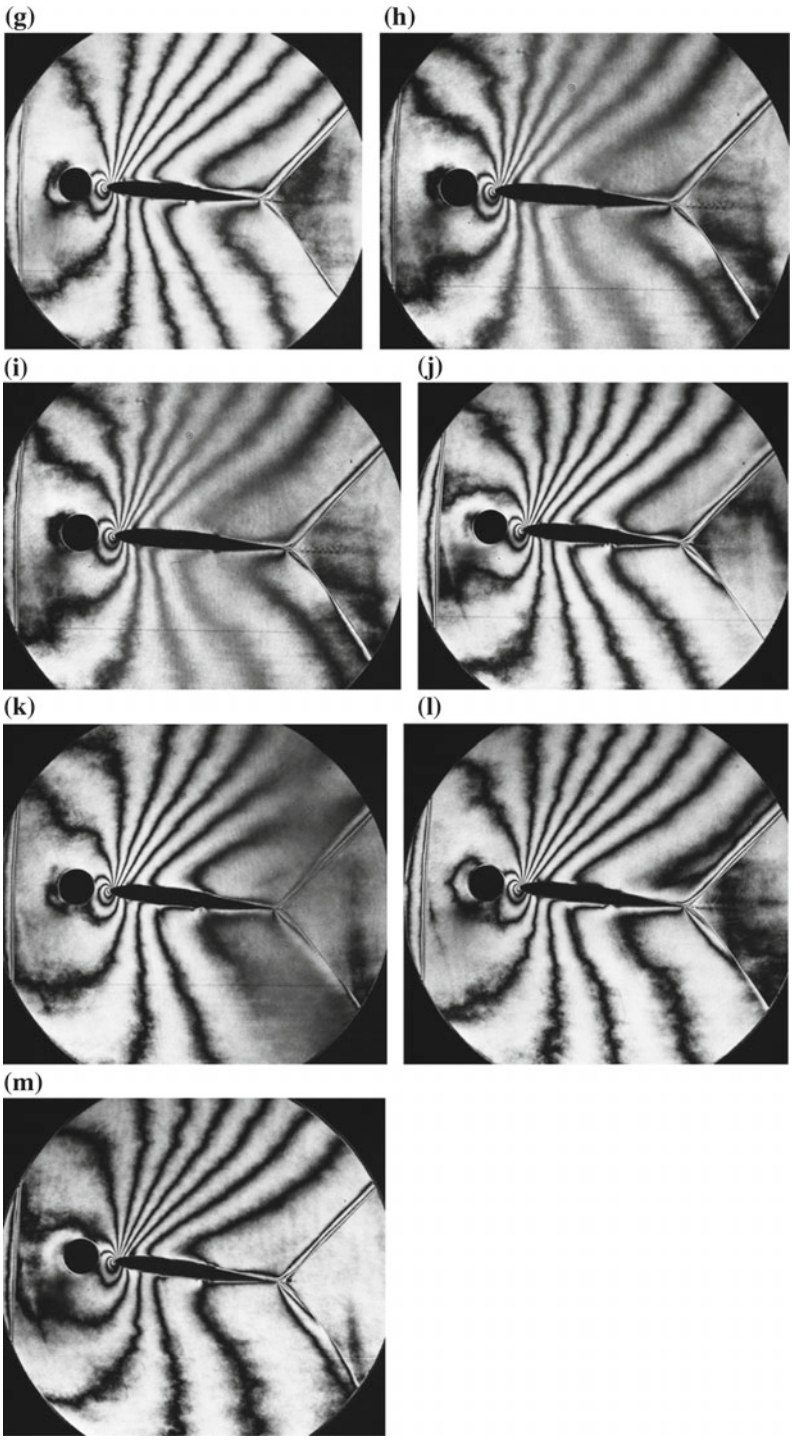

Fig. 4.49 (continued)

4.5 Nozzle Flows

4.5.1 Diverging Nozzle

In Fig. 4.50, a diverging nozzle of apex angle 25° was installed in the 60 mm 150 mm conventional shock tube (Saito et al. 2000) A shock wave of Ms = 2.40 at 150 hPa, 292.1 K impinged at the entry wall is shown in Fig. 4.50a. The shock wave was diffracted at the corner and the interaction took place. With the elapsed time, so-called nozzle starting process occurred. In Fig. 4.50i, a uniformly expanding flow region appeared. Usually the shape of diverging section is designed to promote the uniformly expanding flow region.

4.5.2 Converging and Diverging Nozzle

A diverging nozzle as shown in Fig. 4.50 is the simplest way for establishing a steady supersonic in a shock tube. In order to obtain a more uniform flow region by suppressing the unsteady starting process, converging diverging nozzle having a throat was used. From practical point of view, the nozzle starting is a benign topic for numerical code validations (Saito et al. 2000). However, it was not a simple problem. It was found that the Euler solvers worked only at early stage of the shock wave propagation inside the nozzle. The Navier-Stokes solvers which assumed the existence of a laminar boundary layer worked well only up to early stage of nozzle starting. To reproduce the recorded fringe distributions, it is required to establish a reliable turbulent model.

Figures 4.50 and 4.51 showed experimental results conducted repeatedly for identical Mach numbers and Reynolds numbers and identical initial conditions. The comparison between Figs. 4.50 and 4.51 revealed that the nozzle starting processes are significantly different depending on the throat configuration. The nozzle throat had a straight shape as shown in Fig. 4.50 but is rounded as shown in Fig. 4.47.

Figure 4.52 show very early stage in flow establishment inside a converging and diverging nozzle starting. At very early stage, a laminar boundary layer prevails and therefore, a viscous simulation is relatively benign. When the flow built-up completely, a fully turbulent boundary layer developed. For simulating the flow at this stage, the selection of a suitable turbulent models becomes an important issue. At this time, these images will be useful in validating the numerical code.

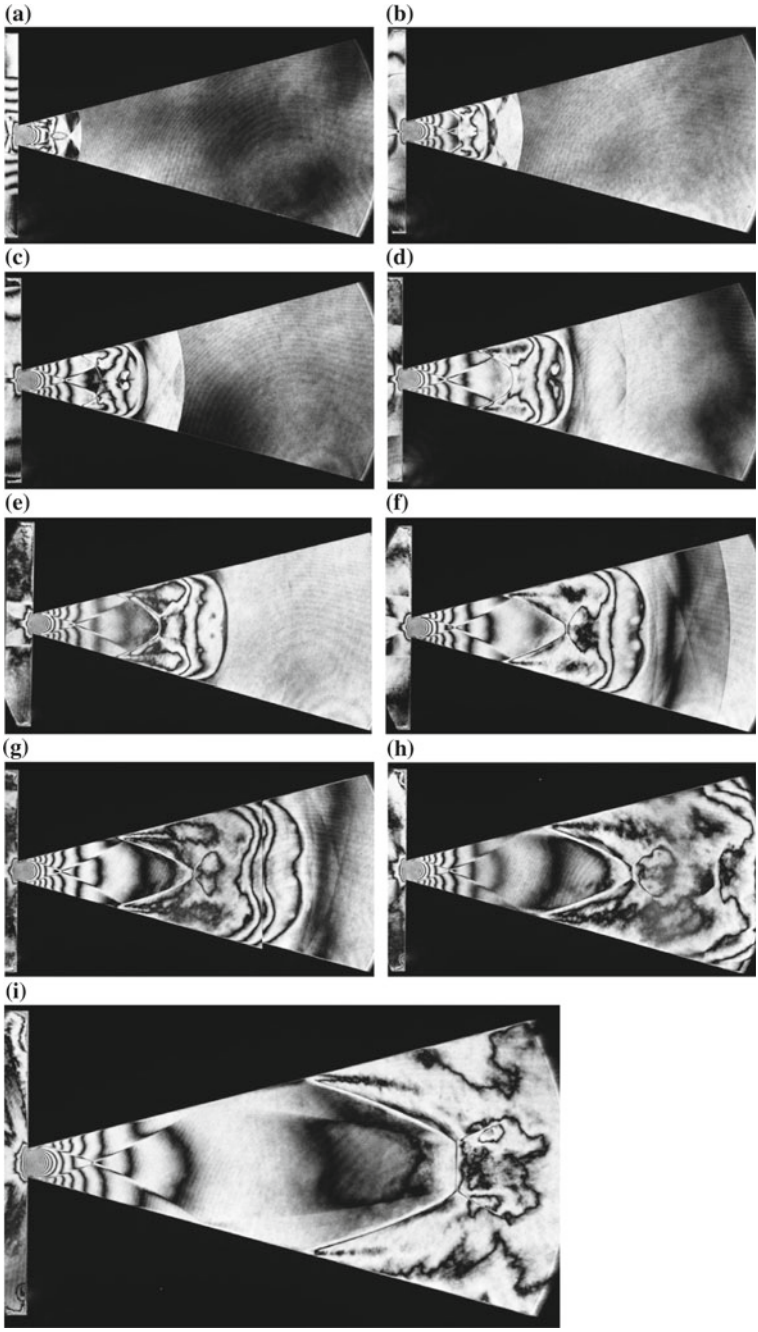

Fig. 4.50 Shock wave propagation in a diverging nozzle in air for Ms = 2.40 at 150 hPa, 292.1 K: **a** #83090804, Ms = 2.430, 298.4 K; **b** #83090805, Ms = 2.430; **c** #83090806, Ms = 2.430; **d** #83090807, Ms = 2.448; **e** 83090809, Ms = 2.391; **f** #83090810, Ms = 2.473: **g** #83090811, Ms = 2.368; **h** #83090812, Ms = 2.408; **i** #83090814, Ms = 2.415

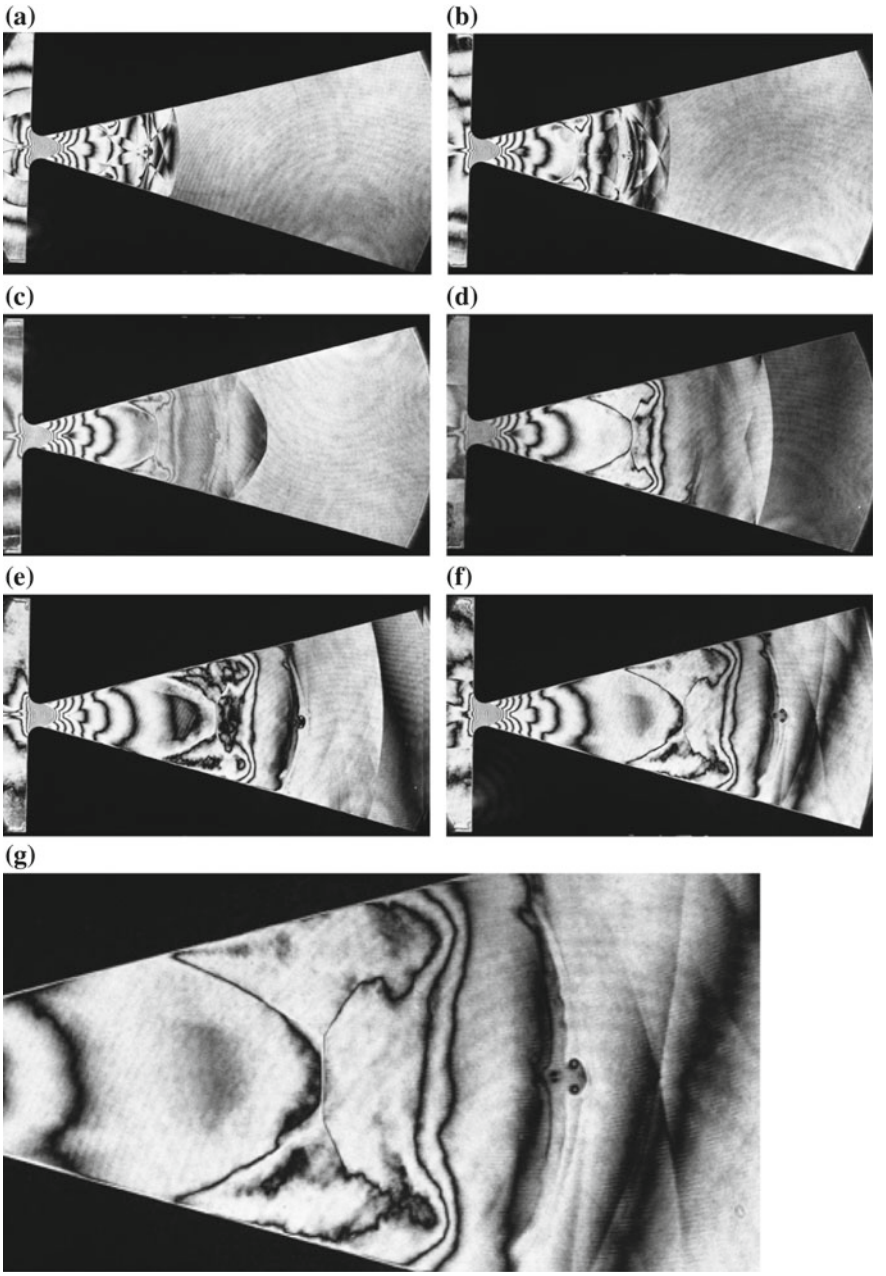

Fig. 4.51 Shock wave propagation inside a converging and diverging nozzle for Ms = 2.45 in air at 150 hPa, 292.1 K: **a** #83082902, 20 μs from starting, Ms = 2.437; **b** #83082905, 50 μs, Ms = 2.455; **c** #83082906, 100 μs, Ms = 2.455; **d** #83082907, 150 μs, Ms = 2.447; **e** #83082909, 200 μs, Ms = 2.422; **f** #83083001, 250 μs, Ms = 2.437; **g** enlargement of (**f**)

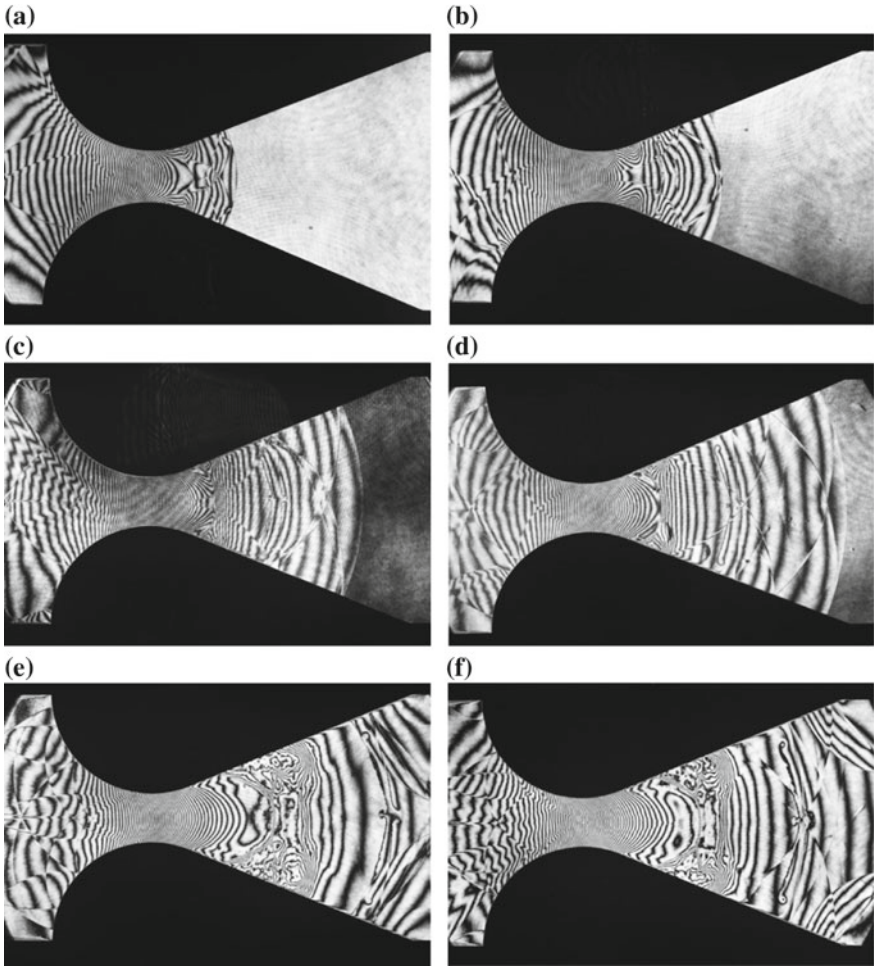

Fig. 4.52 Shock wave propagation in a de Laval nozzle for Ms = 1.50 in atmospheric air at 294.4 K: **a** #85101103 600 μs, Ms = 1.500, atm; **b** #85101104, 650 μs, Ms = 1.496; **c** #85101105, 750 μs, Ms = 1.496; **d** #85101106, 850 μs, Ms = 1.460; **e** #85101107, 950 μs, Ms = 1.524; **f** #85101108, 1050 μs, Ms = 1.487

4.6 Boundary Layers

Some shock wave researchers were tempted to trust analytical models rather than to believe experimental results. They sometimes dared to say "Experiments had errors and uncertainty, whereas theory had a clear background" Analytical models have a clear background. The clear that analytical model have is sometime akin to fiction. Experimentalists working in gas-dynamics are struggling with the flow non-uniformity and unsteadiness or turbulence. The presence of wall boundary

layers is a problem to overcome. Nevertheless, in shock tube experiments, the boundary layer plays an important role (Schlichting 1960).

4.6.1 Boundary Layer in Shock Tube Flows

Figure 4.53a, b show shock tube flows and boundary layers developing along the shock tube side walls of the 60 mm × 150 mm conventional shock tube. Shock waves are propagating from the left to the right. The particle flow is moving from the left to the right. Figure 4.53a–d are displayed upside down. 3.2 mm plastic beads distributed on the wall disturbed the boundary layer development. Figure 4.53c, d show the wavelets created by the beads and their interactions with boundary layers. This was a transient flow and hence the density was uniformly distributed and hence the boundary layer profile could be estimated. However, it should be noticed that these fringe distribution was not truly two-dimensional.

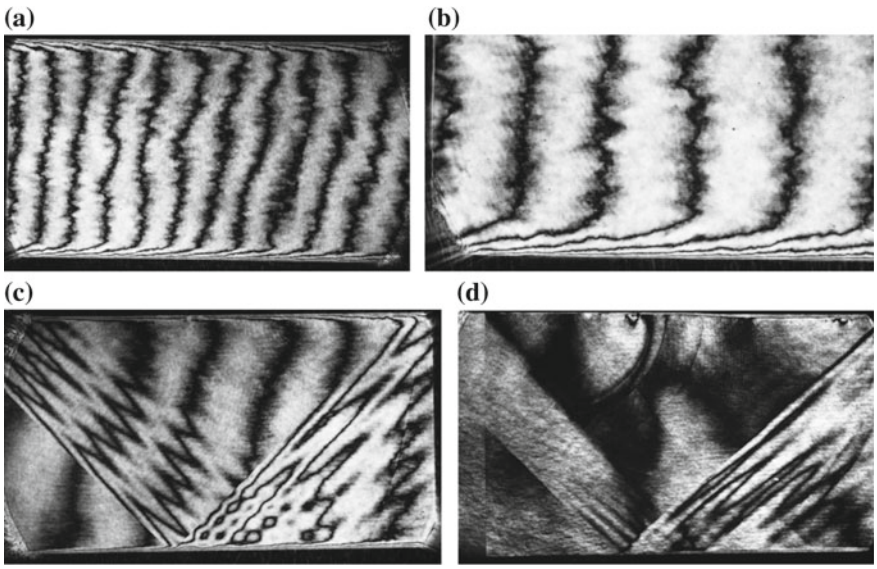

Fig. 4.53 Boundary layers developing behind incident shock wave, 3.2 mm diameter plastic beads are distributed on the upper floors: **a** #90020606, 2.0 ms from the trigger point, Ms = 1.514, in atmospheric air at 289.9 K; **b** enlargement of (**a**); **c** #90020604, 1.0 ms from the trigger point, Ms = 1.498 in atmospheric air at 289.4 K; **d** #90020904, 170 μs from the trigger point, Ms = 1.814 in air at 700 hPa 290.2 K

4.6.2 Reflected Shock Wave/Boundary Layer Interaction

A reflected shock wave reflected from a shock tube end wall interacts with the boundary layer developed behind the incident shock wave. In the advent of the hypersonic flow experiments, a throat and a diverging nozzle were connected to the end of the shock tube and the high enthalpy stagnant condition behind the reflected shock wave was used as the reservoir for the hypersonic flows. Such a shock tube facility is called shock tunnel. In the past, studying high-pressure and high temperature generated behind the reflected shock waves was the hot topics in shock tube technology. The operation of shock tubes was so tuned as to elongate the stagnation condition behind the reflected shock waves near the end wall. This operational method was named as Tailoring (Gaydon and Hurle 1963). This funny name was taken from the profession of making suits. Then in the 1960s, the topic attracted shock wave researchers. It was reported that, depending on the condition, the reflected shock waves interact significantly with the sidewall boundary layer and then bifurcate.

Mark (1956) proposed an analytical model for the bifurcation criterion. When the stagnation pressure in the boundary layer is higher than that prevailing the reflected shock wave, then the reflected shock wave propagates straight in upstream direction. However, if the stagnation pressure in the boundary layer is lower than the pressure ahead of the reflected shock wave, the boundary layer separates and the separation bubble develops with evolving time, Therefore, the foot of the reflected shock wave bifurcates and eventually forms an oblique shock wave.

The degree of the bifurcation is variable, depending on the value of the specific heats ratio of the working gas. The bifurcation becomes violent with the value of γ approaches unity. As in monatomic gas $\gamma = 1.667$, it occurs only in a limited region of Ms and the degree of the bifurcation degree becomes modest. The effect of γ on the bifurcation was experimentally investigated in Honda et al. (1975). Figure 4.54 are sequential observation of reflected shock waves interacting with the boundary layer for Ms = 2.5 in air at 200 hPa 290.4 K. The series of experiments was conducted in a 40 mm $\times$ 80 mm conventional shock tube. Bifurcation was not observed in this experiment of Ms = 2.50 as seen in Fig. 4.54.

Figure 4.55 shows the enlargement of a reflected shock wave shown in Fig. 4.56a for Ms = 3.60 in CO_2 at 50 hPa, 290.3 K. As seen, the foot of the reflected shock wave bifurcated. An oblique shock wave is formed starting from the boundary layer separation point. The boundary layer separation generated a separation bubble. The bifurcated shock wave and the reflected shock wave intersected forming a triple point. The third shock wave and a faintly visible slip line emerge from this triple point. Sequential observation shown in Fig. 4.56 indicates that the triple point is moving toward the center of the shock tube, which implies that the triple point and its three-shock confluence forms an inverse MR. Then, the oblique shock wave is equivalent to the IS, the reflected shock wave is equivalence to the MS and the third shock wave is equivalent to the RS.

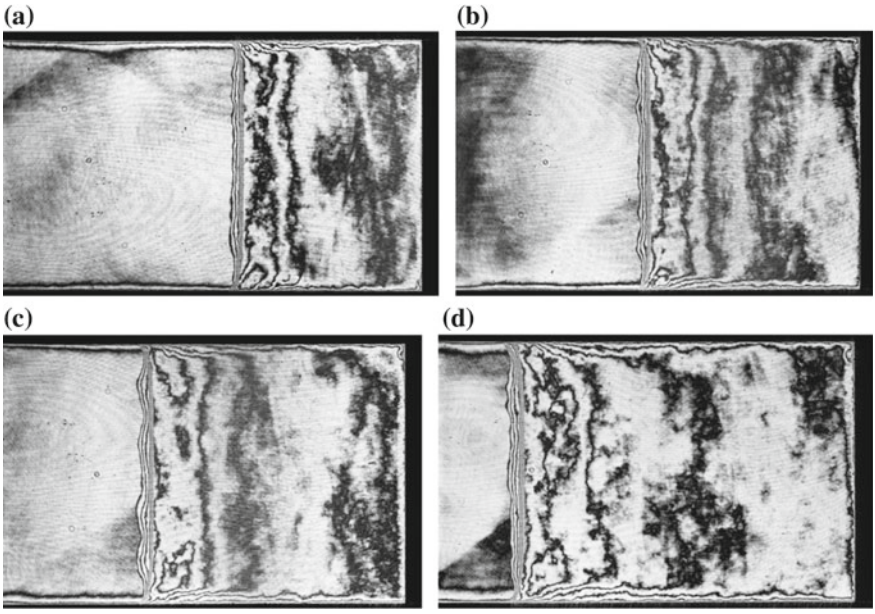

Fig. 4.54 Interaction of the reflected shock waves with the boundary layers for Ms = 2.5 in air at 200 hPa 290.4 K, $\gamma = 1.4$: **a** #81102601 for Ms = 2.561; **b** #81102602, Ms = 2.523; **c** #81102603, Ms = 2.506; **d** #81102606, Ms = 2.506

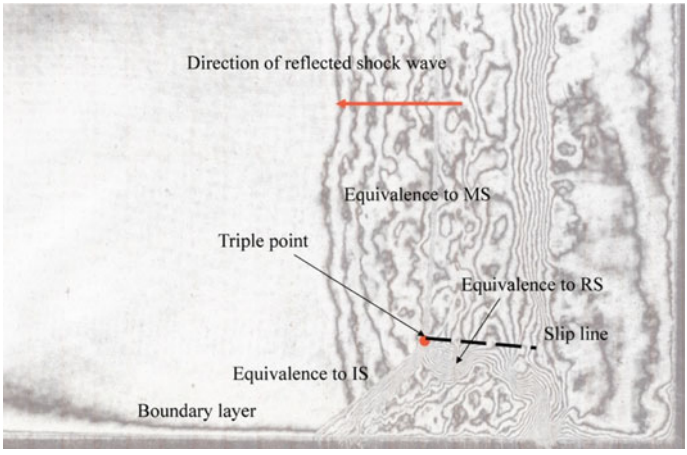

Fig. 4.55 The bifurcation of the reflected shock wave, enlargement of Fig. 4.52a #81102710, for Ms = 3.60 in CO_2 at 50 hPa 290.3 K

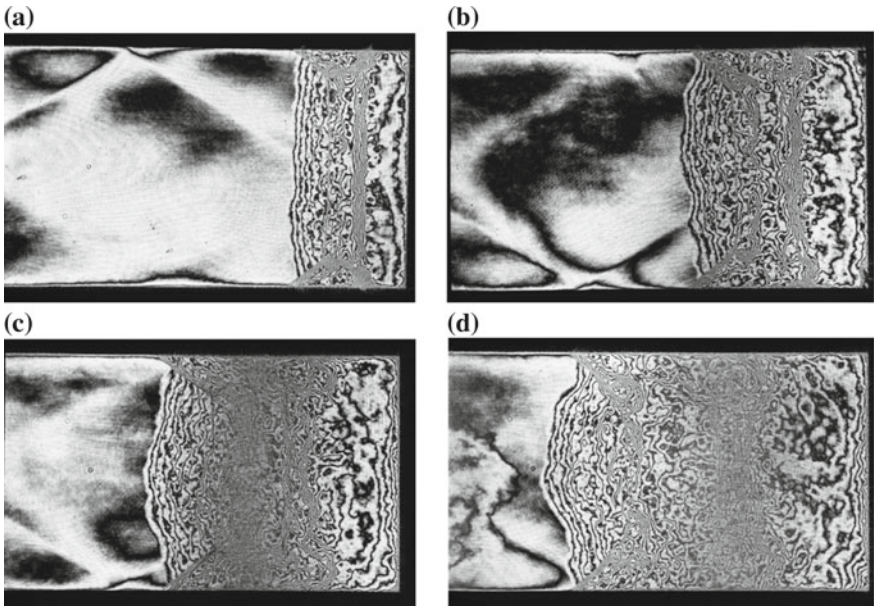

Fig. 4.56 Reflected shock wave/boundary layer interaction for Ms = 3.60 in CO_2 at 50 hPa 290.3 K, γ = 1.29: **a** #81102710, Ms = 3.647; **b** #81102711, Ms = 3.647; **c** #81102713, Ms = 3.774; **d** #81102712, Ms = 3.647

Some of the airbags installed in cars have a structure similar to a shock tube. When such airbags are activated, shock waves propagate in the tube, in which high pressure argon over 20 MPa is filled. Recently it was cleared why argon is used. Argon is a monatomic gas γ = 1.667. It minimizes the bifurcation and the pressure behind the reflected shock wave does not decrease.

In airbags that have similar structures as shock tubes; its operation is initiated by the explosion of explosive material. The explosion transmitted shock waves through the argon toward the end wall. When the end wall ruptured the shock gas flew into the inflator. At that time their bifurcation was suppressed at the end wall then the shocked argon and the resulting gases which were created by the chemical reaction of the explosive material flew into the inflator. At this stage, the role of argon was important.

Figure 4.56 show sequential observation of the reflected shock wave interaction with the side wall boundary layer. The bifurcation developed with the elapsed time. The triple points moved toward the center of the shock tube as seen in Fig. 4.56d.

Figure 4.57 shows an enlargement of Fig. 4.58a #81102718 for Ms = 5.20 in CO_2 at 10 hPa. At the reduced initial pressure, the image contrast seen in Fig. 4.57 is clearer than that seen in Fig. 4.55.

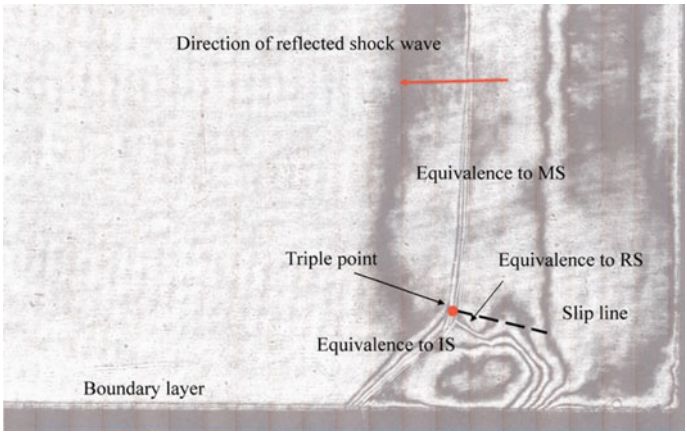

Fig. 4.57 Bifurcation of a reflected shock wave, enlargement of Fig. 4.54a, #81102718, for Ms = 5.20 in CO_2 at 10 hPa 290.3 K

Interpolating the positions of the triple points along the upper and lower walls from Figs. 4.56 and 4.58d, indicates that the trajectories intersected at the center of the shock tube. This means that the reflection patterns is the IvMR. The image data was missing for speculating how this reflection pattern transited to a RR.

As the sidewall boundary layers develop independently of the shock tube size. Therefore, in small shock tubes, the triple points would merger at a short distance from the end wall. Then, the significant pressure reduction would be induced. The effect of the reflected shock interaction with the sidewall boundary layer is governed by the shape of the shock tube cross section. In circular cross sectional shock tubes, the merger of triple point trajectories would be equivalent to focusing.

4.7 Pseudo Shock Waves in a Duct

When supersonic flows in a straight duct decelerate to subsonic flows, a train of shock waves appear, which successively interact with sidewall boundary layer. These shock waves are called pseudo shock waves. This phenomenon appears often in duct flows and pneumatic machineries. Often the pseudo shock wave induced oscillation in pipelines or generated noises. Professor Sugiyama of Muroran Institute of Technology visualized pseudo shock waves using a conventional schlieren method (Sugiyama et al 1987). We were once invited to visualize pseudo shock wave generated in his facility with double exposure holographic

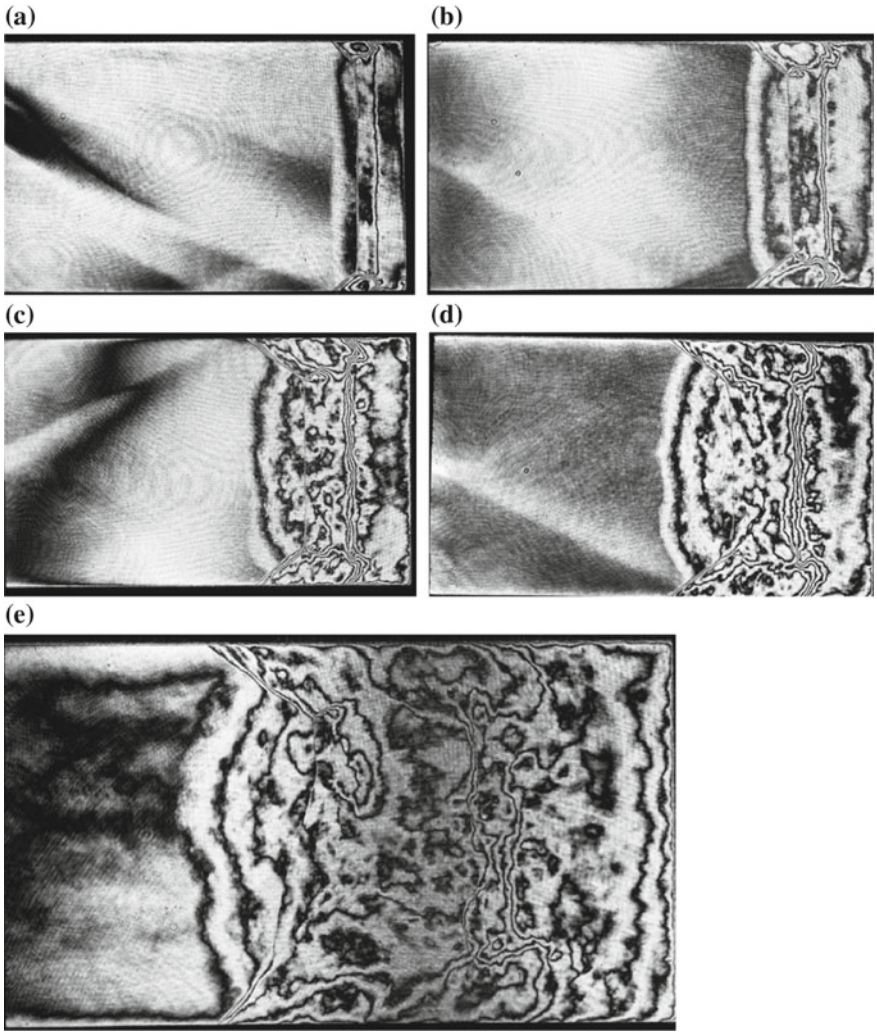

Fig. 4.58 Reflected shock wave/boundary layer interaction for Ms = 5.20 in CO_2 at 10 hPa 290.3 K, γ = 1.29: **a** #81102718, 100 μs from trigger point, Ms = 5.225; **b** #81102717, 150 μs, Ms = 5.043; **c** #81102801, 120 μs Ms = 5.120; **d** #81102716, 200 μs, Ms = 5.102; **e** #81102715, 250 μs, Ms = 5.237

interferometry. The facility was a 50 mm × 50 mm straight duct, the length to diameter ratio was L/D = 20.6–23.6 where the L was duct length, D = 50 mm and the flow Mach number ranged from 1.72 to 1.88. Figure 4.59 show sequential interferograms. It is noticed that the duct has a square cross section and its flow field

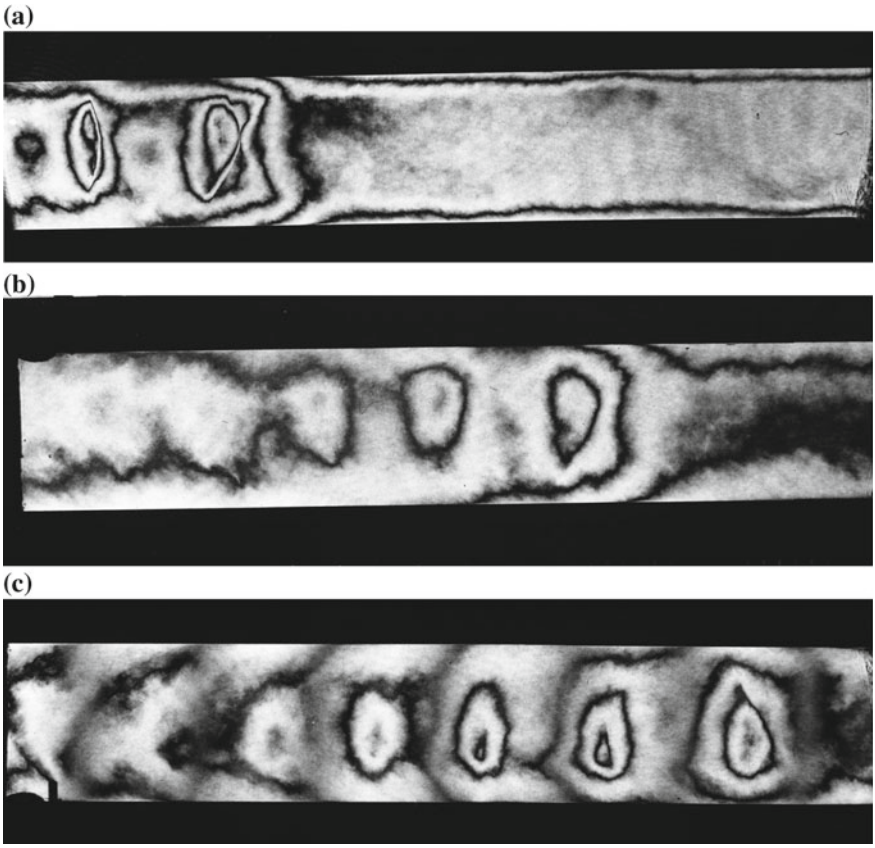

Fig. 4.59 Pseudo shock wave generated in a duct: **a** #87101304; **b** #87101202; **c** #87101302 (Sugiyama et al. 1987)

is not necessarily two-dimensional. The boundary layer developed along the square wall and hence the pseudo shock wave looked slightly blurred. The reflected shock wave bifurcated, when the stagnation pressures in main flows are higher than the stagnation pressures in the boundary layer. This condition is fulfilled in in the region where the pseudo shock waves bifurcate (Inoue et al. 1995).

References

Courant, R., & Friedrichs, K. O. (1948). *Supersonic flows and shock waves*. New York, NY: Wiley InterScience.

Gaydon, A. G., & Hurle, I. R. (1963). *The shock tube high-temperature chemical physics*. London: Chapman and Hall Ltd.

Heilig, W. (1969). Diffraction of shock waves by a cylinder. *Physics Fluids*, *12*, 154–157.

Honda, M., Takayama, K., Onodera, O., & Kohama, Y. (1975). Motion of reflected shock wave in shock tube. In G. Kamimoto (Ed.), *Modern Developments in Shock Tube Research, Proceedings 10th International Shock Tube Symposium*, Kyoto (pp. 320–327).

Inoue, O., Imuta, G., Milton, B. E., & Takayama, K. (1995). Computational study of shock wave focusing in a log-spiral duct. *Shock Waves, 5,* 183–188.

Itoh, K. (1986). *Study of transonic flow in a shock tube* (Master thesis). Graduate School of Engineering, Faculty of Engineering Tohoku University.

Izumi, M. (1988). *Study of particle-gas two phase shock tube flows* (Master thesis). Graduate School of Engineering, Faculty of Engineering Tohoku University.

Kikuchi, T., Takayama, K., Igra, D., & Falcovitz, J. (2016). Shock stand-off distance over spheres in unsteady flows. In G. Ben-Dor, O. Sadat, & O. Igra (Eds.), *Proceedings of 30th ISSW*, Tel Aviv (Vol. 1, pp. 275–278).

Mark, H. (1956). *The interaction of a reflected shock wave with the boundary layer in a shock tube*. NACA TM 1418.

Saito, T., Timofeev, E. V., Sun, M., & Takayama, K. (2000). Numerical and experimental study of 2-D nozzle starting processes. In G. J. Ball, R. Hillier, & G. T. Roberts (Eds.), *Proceedings of 2nd ISSW*, London (Vol. 2, pp. 1071–1076).

Schlichting, H. (1960). *Boundary layer theory*. New York, NY: McGraw Hill Book Company Ltd.

Smith, L. G. (1948). *Photographic investigation of the reflection of plane shocks in air* (Office of Scientific Research and Development OSRD Report 6271), Washington DC, USA.

Sugiyama, H., Takeda, H., Zhang, J., & Abe, F. (1987). Multiple shock wave and turbulent boundary layer interaction in a rectangular duct. In G. Groenig (Ed.), *Shock Tube and Waves, Proceedings of 16th International Symposium on Shock Tubes and Waves*, Aachen (pp. 185–191).

Sugiyama, H., Doi, H., Nagumi, H., & Takayama, K. (1988). Experimental study of high-speed gas particle unsteady flow past blunt bodies. *Proceedings of the16th International Symposium on Space Technology and Science*, Sapporo (pp. 781–786).

Sun, M., Saito, T., Takayama, K., & Tanno, H. (2005). Unsteady drag on a sphere by shock wave loading. *Shock Waves, 14,* 3–9.

Sun, M., Yada, K., Ojima, H., Ogawa, H, & Takayama, K. (2001). Study of shock wave interaction with a rotating cylinder. In K. Takayama (Ed.), *Proceedings of SPIE 24th International Congress of High Speed Photography and Photonics*, Sendai (pp. 682–687).

Tanno, H., Komuro, T., Sato, K., Itoh, K., Ueda, S., Takayama, K., & Ojima, H. (2004). Unsteady drag force measurement in shock tube. In Z. L. Jiang (Ed.), *Proceedings of 24th ISSW*, Beijing (Vol. 1, pp. 371–376).

Timofeev, E. V., Takayama, K., Voinovich, P. V., Sislian, J., & Saito, T. (1997). Numerical and experimental study of three-dimensional unsteady shock wave interaction with an oblique cylinder. In A. P. F. Houwing, & A. Paul (Eds.), *Proceedings of 21st ISSW*, The Great Keppel Island (Vol. 2, pp. 1487–1492).

Yada, K. (2001). *Unsteady transition of reflected shock wave over bodies in shock tube flows* (Ph.D. thesis). Graduate School of Engineering, Faculty of Engineering Tohoku University.

Yang, J.-M. (1995). *Experimental and analytical study of behavior of weak shock waves* (Ph.D. thesis). Graduate School of Tohoku University, Faculty of Engineering.